The Astrophysical Journal Letters, 996:L33 (43pp), 2026 January 10 https://doi.org/10.3847/2041-8213/ae2a30
© 2026. The Author(s). Published by the American Astronomical Society.
OPEN ACCESS

Lightcurves, Rotation Periods, and Colors for Vera C. Rubin Observatory's First Asteroid Discoveries

Sarah Greenstreet[1,2], Zhuofu (Chester) Li[2], Dmitrii E. Vavilov[2], Devanshi Singh[2], Mario Jurić[2], Željko Ivezić[2], Siegfried Eggl[3,4], Alec Koumjian[5], Joachim Moeyens[2,5], Valerio Carruba[6,7], Maria Womack[8], Mikael Granvik[9,10], Anastasia Alexov[11], Pierre Antilogus[12], Ƀrian J. Baumanć[13], Eric C. Bellm[2], Alexandre Boucaud[14], Andrew Bradshaw[15,16], Jeffrey L. Carlin[11], Hsin-Fang Chiang[15], Philip N. Daly[17], Felipe Daruich[18], Guillaume Daubard[12], Erik Dennihy[11], Stephanie JH Deppe[1], Holger Drass[18], Emmanuel Gangler[19], Laurent Le Guillou[20], Leanne P. Guy[18], Patrick A. Hascall[15], Patrick Ingraham[21], M. James Jee[22,23], Tim Jenness[11], Steven M. Kahn[24], Arun Kannawadi[25], Lee S. Kelvin[26], Jacob A. Kurlander[2], Didier Laporte[12], Nate B. Lust[26], Mostafa Lutfi[11], Lauren A. MacArthur[26], Gabriele Mainetti[27], Moniez Marc[28], Andrés A. Plazas Malagón[15,16], David Jiménez Mejías[18], Ƒelipe Menanteau[29], David J. Mills[11], William O'Mullane[18], Angelo Fausti Neto[11], Jeremy Neveu[30], Erfan Nourbakhsh[26], HyeYun Park[31], Maria T Patterson[2], John R. Peterson[32], Bruno C. Quint[11], Tiago Ribeiro[11], Stephen T. Ridgway[33], Wouter van Reeven[18], Jacques Sebag[34], Nima Sedaghat[2], Richard A. Shaw[35], Alan L. Strauss[1], Krzysztof Suberlak[2], Ian S. Sullivan[2], John D. Swinbank[26,36], Sandrine Thomas[11], Adam Thornton[34], W. M. Wood-Vasey[37], Christopher W. Walter[25], Charlotte Ward[38], and Beth Willman[39]

[1] NSF-DOE Vera C. Rubin Observatory/NSF NOIRLab, 950 N. Cherry Avenue, Tucson, AZ 85719, USA; sarah.greenstreet@noirlab.edu
[2] DiRAC Institute and the Department of Astronomy, University of Washington, 3910 15th Avenue NE, Seattle, WA 98195, USA
[3] The Grainger College of Engineering, Department of Aerospace Engineering, University of Illinois Urbana-Champaign, Urbana, USA
[4] Department of Astronomy, University of Illinois at Urbana-Champaign, Urbana, IL 61801, USA
[5] B612 Foundation Asteroid Institute, P.O. Box 100, Mill Valley, California, CA 94942, USA
[6] São Paulo State University (UNESP), School of Engineering and Sciences, Guaratinguetá, SP 12516-410, Brazil
[7] Laboratório Interinstitucional de e-Astronomica, RJ 20765-000, Brazil
[8] Department of Physics, University of Central Florida, 4111 Libra Drive, Physical Sciences Building 430, Orlando, FL 32816-2385, USA
[9] Department of Physics, P.O. Box 64, 00014, University of Helsinki, Finland
[10] Asteroid Engineering Laboratory, Luleøa University of Technology, Box 848, SE-981 28 Kiruna, Sweden
[11] Vera C. Rubin Observatory Project Office, 950 N. Cherry Avenue, Tucson, AZ 85719, USA
[12] Sorbonne Université, Université Paris Cité, CNRS/IN2P3, LPNHE, 4 place Jussieu, F-75005 Paris, France
[13] Lawrence Livermore National Laboratory, 7000 East Avenue, Livermore, CA 94550, USA
[14] Université Paris Cité, CNRS, Astroparticule et Cosmologie, F-75013 Paris, France
[15] SLAC National Accelerator Laboratory, 2575 Sand Hill Road, Menlo Park, CA 94025, USA
[16] Kavli Institute for Particle Astrophysics and Cosmology, SLAC National Accelerator Laboratory, 2575 Sand Hill Road, Menlo Park, CA 94025, USA
[17] Steward Observatory, 933 N. Cherry Avenue, Tucson AZ 85719, USA
[18] Vera C. Rubin Observatory, Avenida Juan Cisternas #1500, La Serena, Chile
[19] Université Clermont Auvergne, CNRS/IN2P3, LPCA, 4 Avenue Blaise Pascal, F-63000 Clermont-Ferrand, France
[20] Laboratoire de Physique Nucléaire et des Hautes Energies, Sorbonne Université, CNRS/IN2P3, 4 place Jussieu, 75005 Paris, France
[21] Steward Observatory, The University of Arizona, 933 N. Cherry Avenue, Tucson, AZ 85721, USA
[22] Department of Astronomy, Yonsei University, 50 Yonsei-ro, Seoul 03722, Republic of Korea
[23] Department of Physics and Astronomy, University of California, Davis, One Shields Avenue, Davis, CA 95616, USA
[24] Departments of Physics and Astronomy, University of California, Berkeley, CA 94720, USA
[25] Department of Physics, Duke University, Durham, NC 27708, USA
[26] Department of Astrophysical Sciences, Princeton University, Princeton, NJ 08544, USA
[27] CNRS, CC-IN2P3, 21 avenue Pierre de Coubertin, CS70202, F-69627 Villeurbanne cedex, France
[28] Laboratoire de Physique des deux infinis Irène Joliot-Curie, Université Paris-Saclay, CNRS/IN2P3, IJCLab, 91405 Orsay, France
[29] National Center for Supercomputing Applications, University of Illinois Urbana-Champaign, 1205 W. Clark Street, Urbana, IL 61801, USA
[30] Université Paris-Saclay, CNRS/IN2P3, IJCLab, 15 Rue Georges Clemenceau, F-91405 Orsay, France
[31] Duke University, Science Drive, Durham, NC 27710, USA
[32] Department of Physics and Astronomy, Purdue University, 525 Northwestern Avenue, West Lafayette, IN 47907, USA
[33] NSF NOIRLab, 950 N. Cherry Avenue, Tucson, AZ 85719, USA
[34] Vera C. Rubin Observatory, 950 N. Cherry Avenue, Tucson, AZ 85719, USA
[35] Space Telescope Science Institute, 3700 San Martin Drive, Baltimore, MD 21218, USA
[36] ASTRON, Oude Hoogeveensedijk 4, 7991 PD, Dwingeloo, The Netherlands
[37] Pittsburgh Particle Physics, Astrophysics, and Cosmology Center (PITT PACC). Physics and Astronomy Department, University of Pittsburgh, Pittsburgh, PA 15260, USA
[38] Department of Astronomy & Astrophysics, 525 Davey Lab, 251 Pollock Road, The Pennsylvania State University, University Park, PA 16802, USA
[39] LSST Discovery Alliance, 933 N. Cherry Avenue, Tucson, AZ 85719, USA

Received 2025 July 30; revised 2025 November 19; accepted 2025 December 6; published 2026 January 7

Original content from this work may be used under the terms of the Creative Commons Attribution 4.0 licence. Any further distribution of this work must maintain attribution to the author(s) and the title of the work, journal citation and DOI.

Abstract

We present lightcurves, rotation periods, and colors for the first asteroid discoveries made with the NSF-DOE Vera C. Rubin Observatory. These are the first science results derived from the 2103 asteroid discoveries released as part of the Rubin First Look (RFL) media event on 2025 June 23, in which the first LSST Camera commissioning images were released. The ∼340,000 observations in which the discoveries were made span nine nights between 2025 April 21 and May 5. With a limiting single-epoch 5σ depth of ∼23–25 mag and dense temporal sampling under an irregular, commissioning-driven cadence, the RFL observations provide an ideal test bed for determination of rotation periods, including sensitivity to rapid rotation. We model lightcurves and derive rotation periods and colors for the ∼2000 objects. We find 75 main-belt asteroids (MBAs) and one near-Earth object (NEO) with reliable rotation periods spanning 0.031–21.3 hr and a photometric precision in the range of 0.05–0.15 mag. We find 19 superfast rotators with periods shorter than the 2.2 hr spin barrier. Rubin-discovered MBA 2025 MN_{45} is the fastest-rotating $d > 0.5$ km known asteroid with a rotation period of 1.9 minutes; along with NEO 2025 MJ_{71} (1.9 minutes) and Rubin-discovered MBAs 2025 MK_{41} (3.8 minutes), 2025 MV_{71} (13 minutes), and 2025 MG_{56} (16 minutes), these five super- to ultrafast rotators join a couple of NEOs as the fastest-spinning subkilometer asteroids known. As this study demonstrates, even in early commissioning, Rubin is successfully probing a previously sparsely sampled region of the subkilometer size−spin rate regime for MBAs.

Unified Astronomy Thesaurus concepts: Small Solar System bodies (1469); Main belt asteroids (2036); Asteroid rotation (2211); Light curves (918); Two-color diagrams (1724); Photometry (1234); Optical astronomy (1776)

1. Introduction

Asteroids (minor planets) are small rocky bodies that orbit the Sun. There are currently ∼1.45 million asteroids known, including ≃41,000 near-Earth objects (NEOs) and ≃4600 comets reported by the Minor Planet Center (MPC). These small bodies are fragments of leftover planetesimals from the early formation of the solar system 4.6 billion years ago and preserve important information about the composition of the solar nebula that formed the Sun and planets. Moreover, their organic compounds and water contents can provide hints to the origin of life on Earth (P. Michel et al. 2015). As such, studying asteroid orbits, sizes, shapes, rotation periods, internal structures, bulk compositions, and surface properties is crucial to our understanding of the formation and evolution of the solar system.

In particular, understanding the rotational properties of asteroids is critical for deciphering their physical structure and collisional history. In photometric studies, the brightness of an asteroid arises from the scattering of sunlight off its surface. For asteroids with nonspherical shapes, variation in the object's brightness can be distinguished as the body rotates. This periodic magnitude variation can be used to compute the period at which the asteroid rotates and provide a rough idea of how elongated the asteroid is based on the amplitude of its magnitude variation.

A key feature of asteroid rotation is called the "spin barrier," which is the maximum rotation rate that a cohesionless object can sustain before the centrifugal force overcomes self-gravity, potentially leading to structural fragmentation of the asteroid or binary formation (P. Pravec & A. W. Harris 2007). The spin barrier for main-belt asteroids (MBAs) larger than 0.15 km is ≈2.2 hr (A. Carbognani 2017), while Jupiter Trojans have a spin barrier of ≈4.4 hr (Z. Li et al. 2025); this longer critical spin barrier indicates lower bulk densities for Jupiter Trojans compared to MBAs, likely due to higher fractions of ices and volatile materials (S. Mottola et al. 2024). Knowing where the rotation period of an object falls compared to its spin barrier can provide information about its bulk density and collisional history. Objects that rotate faster than the spin barrier are likely to have higher bulk densities that prevent their fragmentation when spinning at higher speeds, which could indicate that the object experienced a recent collision, has been spun up to a higher rotation period owing to the Yarkovsky–O'Keefe–Radzievskii–Paddack (YORP) effect (S. J. Paddack 1969), or has a surface with nonzero cohesion/strength. Numerous NEOs and MBAs have been found to exhibit rotation periods faster than the 2.2 hr spin barrier (see Section 4.1.1 for discussion), as well as at least one Jupiter Trojan (C. Kiss et al. 2025) and a couple of Hildas (N. Takács et al. 2025) that rotate faster than the 4.4 hr spin barrier. The amplitude of the observed magnitude variation also indicates the rough elongation of the body, with a higher amplitude pointing to a less spherical shape. For asteroid family members, their shapes can potentially provide a rough indication of the age of the family; G. M. Szabó & L. L. Kiss (2008) and G. M. Szabó et al. (2022) show from statistical analyses that asteroid shapes can evolve from elongated fragments in young families to rough spheroidal shapes in older families owing to heavy bombardment.

Asteroid colors provide powerful hints to their surface chemical composition and the effects of space weathering, including the ability to decipher asteroid taxonomic classifications discriminating between S, C, and V types (Ž. Ivezić et al. 2001). For example, the Sloan Digital Sky Survey (SDSS) multiband photometry of over 10,000 asteroids shows a strong bimodal distribution in the $g - r$ and $r - i$ color–color space corresponding to high-albedo S-type asteroids and low-albedo C-type asteroids (Ž. Ivezić et al. 2002a). In addition, as groups of asteroids that are thought to have originated from the breakup of a larger, single asteroid, thus sharing a common origin, asteroids in families also tend to share similar chemical compositions. The identification of distinct color groupings among asteroid families has provided improved family definition for nearby and/or overlapping families (Ž. Ivezić et al. 2002b; A. Parker et al. 2008; V. Carruba et al. 2024).

Previous surveys (e.g., SDSS, D. G. York et al. 2000; Gaia, P. Tanga et al. 2023; the Small Main-belt Asteroid Spectroscopic Survey (SMASS), R. P. Binzel et al. 2004; F. E. DeMeo & R. P. Binzel 2011) have provided photometric and spectroscopic observations for over 1 million asteroids. The Vera C. Rubin Observatory is expected to provide photometry for up to 5 million small bodies across the solar system over the next decade (Ž. Ivezić et al. 2019; J. A. Kurlander et al. 2025),

enabling much larger studies that will transform our understanding of asteroid physical structures and collisional histories and to a greater degree the formation and evolution of the solar system.

1.1. The Vera C. Rubin Observatory Overview and Status

The NSF-DOE Vera C. Rubin Observatory (Ž. Ivezić et al. 2019) is a new sky survey facility funded by the US National Science Foundation and the US Department of Energy's Office of Science and currently being completed in the Southern Hemisphere. Located on Cerro Pachón in Chile, it houses the 8.4 m wide-field Simonyi Survey Telescope (B. Stalder et al. 2024). This telescope is equipped with the 3.2-gigapixel LSST Camera (LSSTCam; A. Roodman et al. 2024; SLAC National Accelerator Laboratory & NSF-DOE Vera C. Rubin Observatory 2025), designed with a wide 9.6 deg^2 field of view with delivered image quality of the order 1″. A single 30 s exposure can reach a depth of $m_r \sim 24$, and with a settle-and-slew time of ≈5 s, the telescope is able to take up to 1000 exposures each night.

Toward the start of 2026, the observatory will begin conducting the Legacy Survey of Space and Time (LSST), a decade-long campaign to repeatedly image the southern sky in multiple bands. The main LSST survey will use six filters spanning near-ultraviolet to near-infrared wavelengths (*ugrizy*), revisiting the same pointing twice each night, returning to take additional pairs every few nights. Details of the survey cadence and optimization are still being finalized, with the current recommendations presented in F. B. Bianco et al. (2022). The cadence is designed to result in a dataset capable of answering numerous and varied science cases, from understanding the nature of dark energy to discovering and characterizing millions of asteroids, comets, interstellar objects (C. O. Chandler et al. 2025), and transneptunian objects (TNOs) in the solar system (J. A. Kurlander et al. 2025).

Delivery of the LSST dataset is supported by advanced, automated data processing pipelines and facilities—the LSST Data Management (DM) System (M. Jurić et al. 2017; W. O'Mullane et al. 2022). The DM system is designed to store raw images and process, generate, and distribute reduced images and catalogs on timescales from 60 s (alerts) to annual (Data Releases). It includes the comprehensive data reduction software package, LSST Science Pipelines (J. Bosch et al. 2018; Rubin Observatory Science Pipelines Developers 2025). The performance of the DM system and science pipelines on the Rubin system has been preliminarily characterized using the LSST Commissioning Camera (LSSTComCam (similar to LSSTCam but smaller in scale); SLAC National Accelerator Laboratory & NSF-DOE Vera C. Rubin Observatory 2024; Vera C. Rubin Observatory 2025). The pipeline suite includes tools for identification and linking of observations of solar system bodies (M. J. Holman et al. 2018; A. Heinze et al. 2023). This toolchain has already been used to analyze the data of the Hyper Suprime-Cam Survey (H. Aihara et al. 2018), as well as to detect asteroids in the Dark Energy Survey, the Catalina Sky Survey, and the Asteroid Terrestrial-impact Last Alert System archival data (including 2022 SF_{289}, a potentially hazardous asteroid; L. Denneau et al. 2023). Vera C. Rubin Observatory (2025) describes the details of the LSST Science Pipelines processing, data validation, and performance assessment from LSSTComCam commissioning, including photometric calibration and difference image purity and detection completeness; we refer the reader to Vera C. Rubin Observatory (2025) for details of the Rubin Observatory photometry, in particular for moving objects. The full range of data products that will be included in the LSST data releases is provided in the LSST Data Products Definition Document (M. Jurić et al. 2023).

Table 1
Overview of the Rubin First Look (RFL) Imaging (M49 Field) and Small-body Data

RFL Parameter	RFL Quantity
Dates of observation (mm/dd, UTC)	4/22, 4/25, 4/28, 4/29, 4/30, 5/2, 5/3, 5/4, 5/5
Bands (visits)	*u* (261), *g* (281), *r* (388), *i* (255); total (1,185)
Exposure times	30 s for *g*, *r*, *i*, 38 s for *u*
Sky coverage	24 deg^2
Field center	(R.A., decl.) ≈(186.4, 6.8) deg, (λ, β) ≈ (183, 8.8) deg
Small bodies detected	2103
Observations per object	16 (min), 132 (median), 509 (max)
Observations per band	*g* (109,304), *r* (162,775), *i* (71,567), *u* (114); total (343,760)
Dynamical classes	Apollo (2), Amor (5), Mars Crosser (19), main belt (2021), Jupiter Trojan (11), other (34), Jupiter coupled (6), TNO (5)

1.2. Rubin First Look Observations

The Rubin Observatory is currently in the commissioning phase. During this time, the Rubin system is being verified, validated, and fine-tuned with a set of tests of increasing complexity. As this is ongoing, both the quality of the data and the rate of acquisition can vary. Additionally, the choice of what and how to observe—the pointings, cadence, depth, etc.—is guided primarily by engineering and testing concerns and does not correspond to the expected final cadence (F. B. Bianco et al. 2022).

An early engineering test led to the taking of 1185 images covering approximately 24 deg^2 in the area near M49 and covering much of the Virgo cluster, over nine nights beginning on 2025 April 21 and ending 2025 May 5 (details provided in Table 1). These images were taken to verify Rubin's coaddition, image differencing, and moving object finding capabilities. The coadded RGB image was released as a part of the Rubin First Look (RFL) media event on 2025 June 23; we reproduce this image in Figure 1. We measure the dimensions of this figure to be $5.^{\circ}44 \times 2.^{\circ}86$, by fitting the WCS to the released RGB TIFF image using astrometry.net (D. Lang et al. 2010). The limiting magnitudes of individual exposures comprising this coadd are around ∼23–25 mag, depending on the band. The coadded depth reaches around 26.5 mag (*r* band).

This field is about 9° north of the ecliptic and therefore expected to be rich in asteroids. Indeed, zooming into a smaller section of Figure 1 reveals numerous line-like features as seen in Figure 2, corresponding to asteroids moving from image to image in the coadded stack. These are not trails resulting from a single long exposure; they are individual point-like detections that coadd to a line. The lines typically appear in three colors, each corresponding to a sequence of densely spaced observations in a single band. The segments are

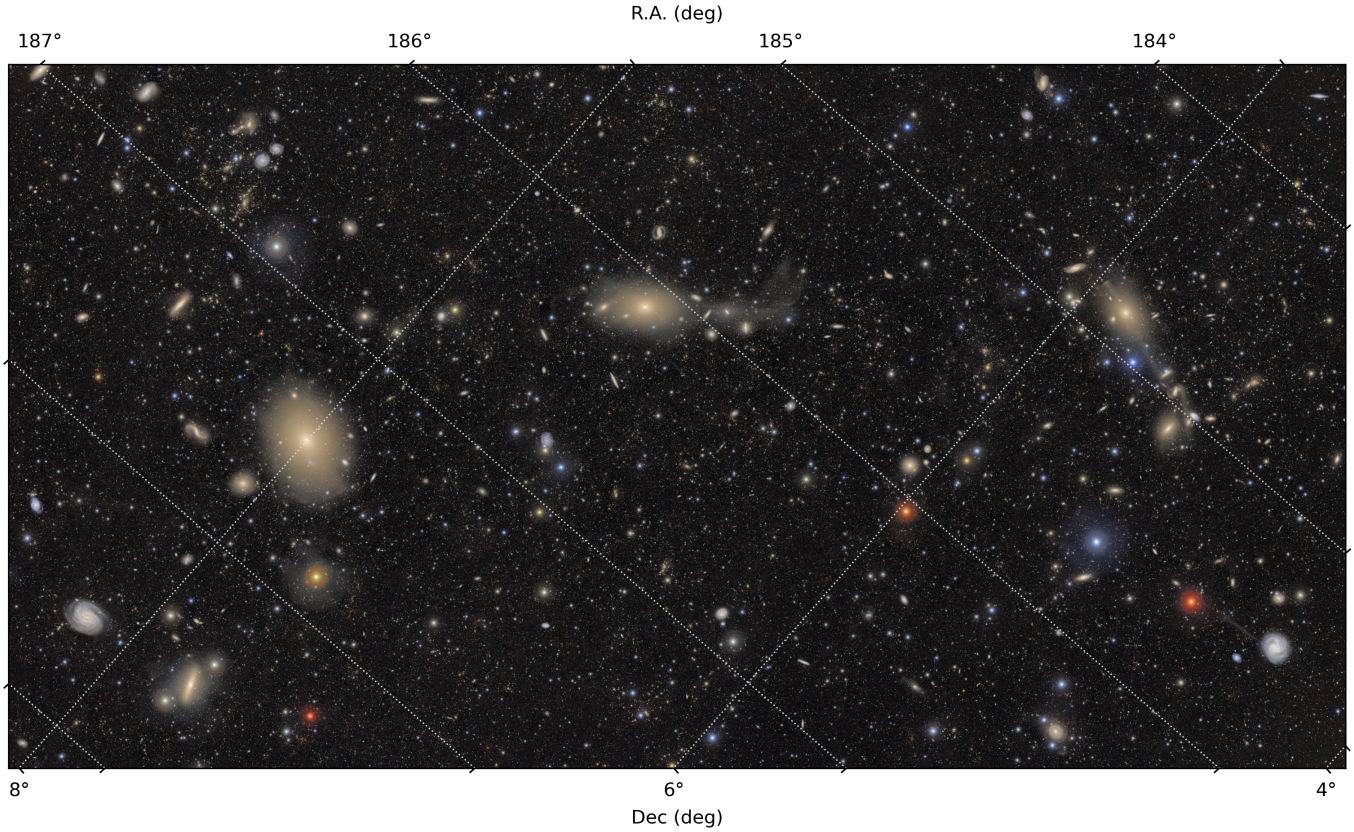

Figure 1. A $5.^{\circ}44 \times 2.^{\circ}86$ RGB coadd (15.6 deg^2) covering the Virgo cluster and published as a part of Rubin Observatory's First Look (RFL) event. The large elliptical galaxy on the left is M49, the prominent galaxy in the center is NGC 4365, and the brightest galaxy on the right is NGC 4261. The image is about 1.6 times the area that NSF-DOE Rubin captures each time it takes an image. This is the region of sky in which the 2103 solar system object discoveries were made that were released as part of the RFL event. Credit: NSF-DOE Vera C. Rubin Observatory.

separated by small gaps resulting from the filter exchange on LSSTCam, which takes about 2 minutes.

Extrapolating to the entire Virgo field, we expect that there should be a few thousand of both known and unknown asteroids. These were searched for by using the coadd from Figure 1, which was cleaned of visible asteroids using aggressive pixel-level outlier rejection in the coaddition phase, as a template against which to difference each individual exposure. Sources were then detected on each difference image using the LSST Science Pipelines.

2. Asteroids in Rubin First Look

The observing cadence in the Rubin M49 RFL field is visualized in Figure 3. Imaging was performed on nine nights, over a 2-week time span, with a substantial number of visits in each night. In particular, each but the final night has over 60 visits taken in the span of a few hours, allowing for construction of densely sampled lightcurves.

In addition, this cadence enables the construction of tracklets and discovery of new asteroids. Rubin discovers asteroids by identifying at least three tracklets over a window of 15 nights, followed by linking them using the `heliolinx` software suite that implements a variant of the Heliolinc algorithm (M. J. Holman et al. 2018; A. Heinze et al. 2023). The former was done by passing the difference image catalogs to the `make_tracklets` routine in the `heliolinx` suite, followed by linking with the `heliolinx` Heliolinc3D implementation. This process resulted in a set of identifications and measurements of known objects, not yet made public, but also the identification of new asteroid candidates. These were released via submission to the Minor Planet Center (MPC) as an ADES file. We obtain the measurements by querying a BigQuery replica[40] hosted by the Asteroid Discovery Analysis and Mapping (ADAM) platform (S. Greenstreet et al. 2021) of the MPC Postgres database[41] (query provided in Appendix A). We note that the objects can also be individually accessed using the MPC Application Programming Interface (API),[42] but bulk download via query is more appropriate for the purpose of this Letter. This query returns 343,760 observations, corresponding to 2103 unique objects. The earliest observation of each object is shown in Figure 4. We also extract the orbits of each of these objects by crossmatching their provisional designations to the MPCORB database. The orbital properties of the 2103 RFL solar system discoveries are illustrated in Figure 5. The discoveries span the range of objects in the solar system, from NEOs to TNOs, with the vast majority being MBAs.

The distribution of the number of observations is shown in Figure 6. The number of observations per object ranges from 16 (minimum) to 509 (maximum), with the median being 132.

[40] http://mpcq.readthedocs.io/en/latest/bigquery_dataset.htm

[41] https://www.minorplanetcenter.net/mpcops/documentation/replicated-tables-info-general/

[42] A tutorial at https://github.com/lsst/tutorial-notebooks/blob/main/MPC/RFL_Solar_System_MPC_Retrieval.ipynb is a good resource to learn more about this type of data access.

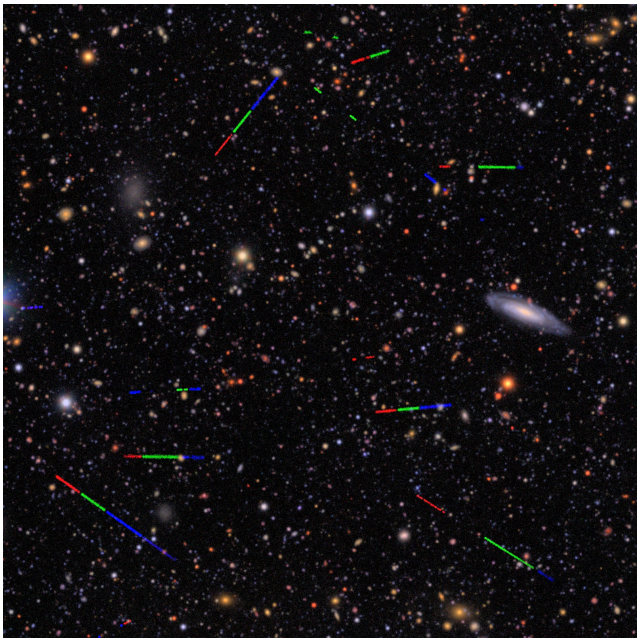

Figure 2. A small (6.5′ × 6.5′) region of Figure 1, located just to the left of M49. The apparent lines are due to bright asteroids that moved between the individual exposures that were used to create the coadd. A closer look reveals that they are composed of a set of closely spaced point sources, one from each input exposure. The color segments correspond to data taken in different bands: red representing the object's flux in the *i* band, green corresponding to the *r* band, and the blue channel capturing a linear combination of *g* and *u* bands. Note that Rubin data reported to the Minor Planet Center (MPC) were measured on individual exposures, not the coadd. Credit: Rubin SkyViewer, https://skyviewer.app.

In particular, there are numerous objects with large numbers (>100) of observations that may be suitable for variability studies.

To assess whether there is any evidence of variability, we look at the rms of the reported magnitudes grouped by band and object. In Figure 7, each point represents the median magnitude versus the rms variability of its magnitude change across the available photometric data, computed for each object. If there were no variability, one would expect these points to roughly follow a line of irreducible error induced by Poisson noise dominated by the sky background. The gray lines show the median errors reported by the LSST pipeline in narrow bins of magnitude, roughly approximating this irreducible floor. The majority of points lie above the gray lines, showing that there is variability that goes beyond noise and justifying a closer look, which we take in the following sections of this Letter. Some objects show very little variability, practically touching the gray limit of irreducible error. While this implies that no period is likely to be measured for these, it also demonstrates that the LSST pipelines' photometry is repeatable to $\lesssim$30 mmag at the bright end.

Finally, at the faint end we see that the computed scatter becomes *smaller* than what the pipeline reports as the expected magnitude error. This is a discovery-selection-induced bias. The small-body sample Rubin reported from RFL contains only new discoveries. These discoveries are made by identifying and linking individual tracklets over at least three nights, requiring a minimum number of detections[43] for the object to be linked and included here. Objects near the flux limit, whose brightness varies appreciably, will be less likely to be detected in images at each opportunity and thus less likely to be discovered overall (and vice versa). We confirm this hypothesis by verifying that this effect diminishes the more observations an object has (not shown). While this does not affect the results of this study, we note that this effect will be very important to include in understanding LSST's selection effects for simulations (e.g., S. R. Merritt et al. 2025) or population studies and may impact the estimates of overall LSST discovery yields (J. A. Kurlander et al. 2025).

We additionally checked a number of the ∼2000 objects for magnitude variability large enough to determine rotation periods by plotting their magnitudes over the observed time frame, starting with those objects with the largest number of observations. An example is shown in Figure 8. As can be seen in the figure, which shows the magnitude over time for RFL solar system object discovery 2025 MM_{81}, from just a single night of observations (bottom panel), the amplitude of the magnitude variation (≃1.2 mag), the object's rotation period (≃0.045 days = ≃1.1 hr), and even its colors (e.g., $g - r \simeq 0.6$) can be determined directly from the raw photometry. Further inspection of the available photometry revealed that this large, dynamically diverse, multiband dataset of solar system object time series is likely to be highly suitable for lightcurve extraction and fitting and rotation period determination.

Building on this robust dataset, we employed the following methods (described in Section 3) to extract and fit lightcurves, rotation periods, and colors for the observed solar system objects. Our results can be found in Section 4, including discussions of fast rotators and estimates of axial elongations in Section 4.1 and asteroid colors in Section 4.2.

3. Lightcurve Modeling and Rotation Period Determination

The visual magnitude of a rotating body can be roughly approximated as

$$V = H + 5\log_{10} r\Delta + \phi(\alpha) + g(t), \quad (1)$$

where H is the absolute magnitude of the body, r and Δ are the heliocentric and topocentric distances (in au), respectively, the phase function $\phi(\alpha)$ describes how the brightness evolves with the phase angle α (Sun−asteroid−observatory), and $g(t)$ is a periodic function related to the shape of the object while in rotation,

$$g(t) = \sum_{j=1}^{k} A_j \cos(2\pi f j t) + B_j \sin(2\pi f j t), \quad (2)$$

where f is the frequency of rotation (cycles per day), t is time (in days), k is the maximal number of Fourier series, and $\{A_j, B_j\}$ is the amplitude coefficients at each frequency. While this rough approximation does not discriminate between the phase angle, pole orientation, and rotational phase dependencies of an asteroid's rotational magnitude variation, as described in Section 1.2 above, the RFL observations were taken over a period of ⩽12 days of a single 24 deg^2 area of the sky and cover a small range of phase angles (≈10°–20°) for the small-body discoveries. As a result, the rotational and phase dependencies can be separated to first order, and the

[43] While the exact linking thresholds have not been published, we note that the smallest total number of detection across all bands is 16.

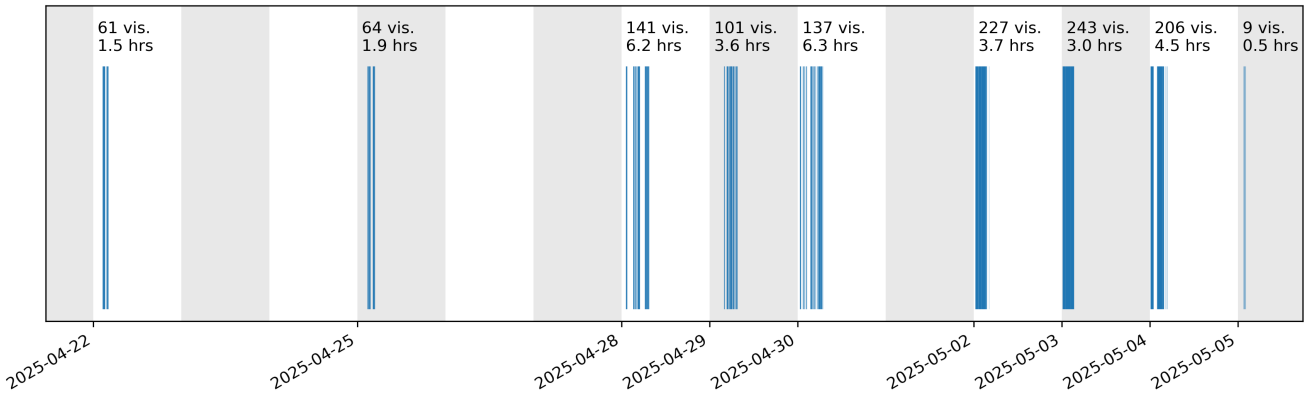

Figure 3. Visualization of the Rubin First Look M49 field cadence, inferred from the data submitted to the MPC on 2025 July 23 by the Rubin Observatory (code X05). The images were taken over nine nights, spanning a total of 14 nights. Meeting the criteria of at least two visits occurring each night, it is possible to construct two-observation tracklets needed for detection and discovery of moving objects. More interestingly, other than the final night, every night has over 60 visits taken in the span of a few hours, allowing for the construction of densely sampled lightcurves.

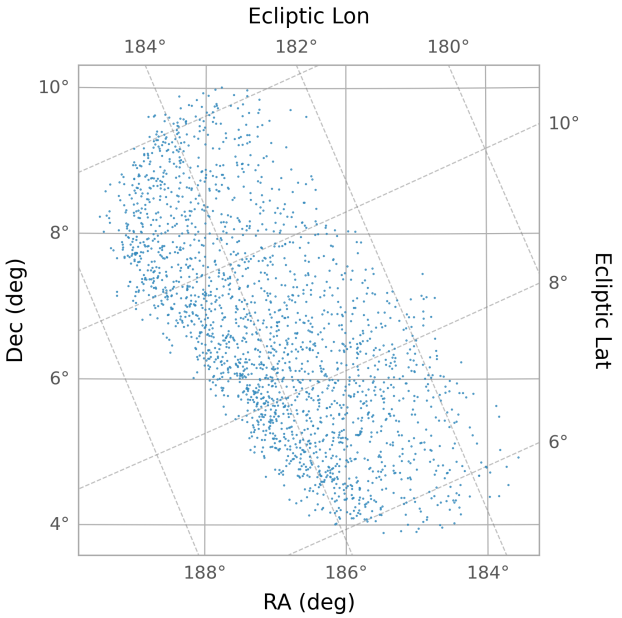

Figure 4. Small bodies in the Rubin First Look M49 field. This figure shows the earliest observation for 2102 of the 2103 small bodies submitted to the MPC by Rubin as a part of the RFL submission. The one remaining object, TNO 2025 MW 47, is located around $(\alpha, \delta) \simeq (212°, -6°)$. It was observed in a different field and unintentionally submitted as part of the RFL release.

amplitude changes in the observed lightcurves should primarily be due to asteroid rotations, making the rough approximation adequate for our purposes, as opposed to using more formal analyses (e.g., M. Kaasalainen & J. Torppa 2001; K. Muinonen et al. 2022).

For objects with nonspherical shapes, variation in the object's brightness can be distinguished as the body rotates. This periodic magnitude variation can be used to compute the period at which the object rotates and provide a rough idea of the extent of the object's elongation based on the amplitude of its magnitude variation.

The vast majority of objects in the RFL data release are discoveries and as such do not have known rotation periods with which we can compare. To assess the robustness of our computed rotation periods, we employed two independent methods for modeling the asteroid lightcurves and determining their rotation periods. We also manually inspected each of the ∼2000 asteroid lightcurves as a final best-fit quality check. We then used the results from both independent rotation period determination methods and the visual inspection to determine the reliability threshold for our computations.

3.1. High-order Fourier Analysis

Our first method to determine the rotation periods of the ∼2000 asteroid lightcurves in the RFL dataset employed a high-order Fourier analysis and followed the approach described in D. E. Vavilov & B. Carry (2025). Here we briefly explain the step-by-step algorithm; for more details, we refer the reader to the original paper. The heliocentric and topocentric distances, r and Δ, respectively, as well as the phase angles, α, were obtained via the NASA Horizons API.[44] First, we subtracted $5\log_{10} r\Delta$ from the observational magnitudes. Then, we corrected the timing of the observations for the speed of light: $t = t' - \frac{c}{\Delta}$, where t' is the observed time, t is the corrected time of observations, and c is the speed of light.

All objects in the RFL data release were observed within a single field over a span of no more than 12 days with phase angles that cover a relatively small range ($\simeq 10°-20°$). This allowed us to model the phase function as a second-order polynomial, $\phi(\alpha) = c_1\alpha + c_2\alpha^2$, as in D. E. Vavilov & B. Carry (2025) for higher efficiency. However, in order to obtain more accurate absolute magnitudes, we also modeled the phase function using HG_{12}^* as described in A. Penttilä et al. (2016) for the asteroids that we consider to have reliable results (i.e., those discussed in Section 4 below). We then used the $g(t)$ function given in Equation (2) above, considering Fourier orders k from 2 to 6 (specifically not considering the model with the first order Fourier series). The absolute magnitude H is a function of the filter, and since the RFL dataset includes observations in different filters, we additionally fit it using the least-squares method, giving us additional parameters for H in each filter. In total we had two parameters from the phase function (c_1, c_2; or one parameter G_{12}^* in the more accurate phase-curve modeling), $2k$ parameters from the

[44] https://ssd.jpl.nasa.gov/horizons

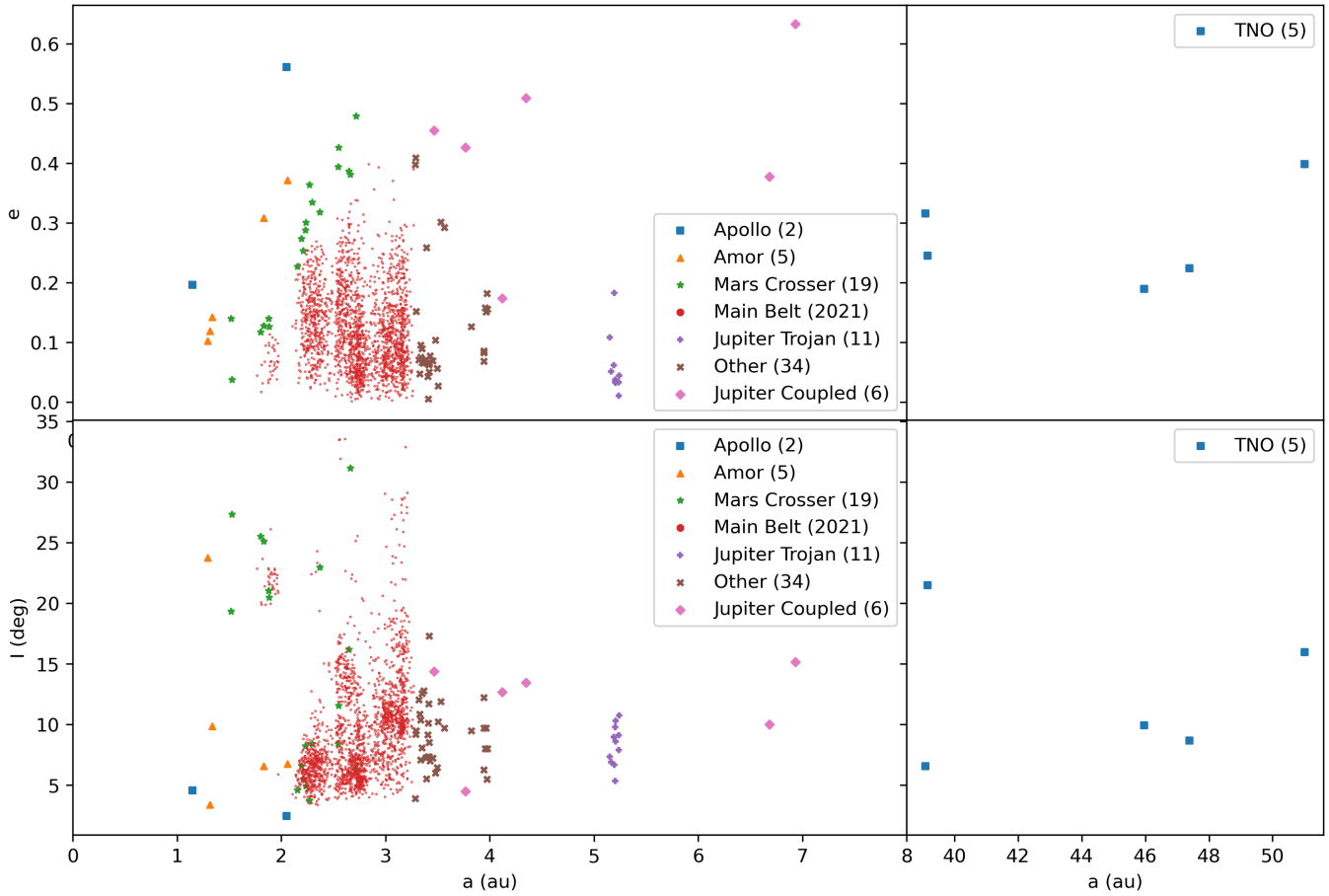

Figure 5. Semimajor axis, eccentricity, and inclination for the 2103 Rubin First Look solar system object discoveries, with colors and symbols indicating orbital class. The left two panels show semimajor axis $a < 8$ au, while the right two panels show semimajor axis $a > 8$ au.

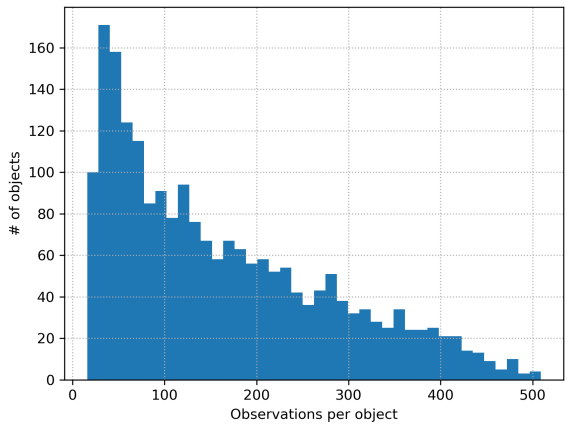

Figure 6. The distribution of observations per object in the Rubin First Look MPC submission. This includes the observations across all bands (*ugri*). The median number of observations is 132.

Fourier series ($\{A_j, B_j\}_{j=1}^{k}$), and up to four H values depending on the number of filters in which the object was observed.

We sampled equidistant frequencies f in the range from the minimal possible frequency that included at least two rotation periods within the observation time span to a maximum that allowed for the detection of ultrafast rotators (rotation periods as small as ∼1 minute). With a maximum of a 12-day span in the observations, the maximum allowed period would be 6 days for two rotations or a minimum frequency of $(6 \times 24)^{-1} = 0.1667$ cycles day^{-1}. For detecting ultrafast rotations, our sampled frequency range went to a maximum of ∼500–1000 cycles day^{-1}, corresponding to a minimum 0.024 hr (≈1.4-minute) rotation period. The number of frequencies sampled was set by $30T(f_{\max} - f_{\min})$, where T is the arc of observations in days.

For each considered frequency f, we fitted the parameters using the weighted least-squares method and computed an unbiased estimate of an observational dispersion:

$$\sigma^2 = \frac{N_{\rm obs}}{\sum_j p_j} \frac{\sum_i p_i (O_i - C_i)^2}{(N_{\rm incl} - n_{\rm par})}, \tag{3}$$

where O_i and C_i are the ith observation and computed magnitude, respectively, p_i is the weight of the ith observation (taken as 1 over the rmsmag^2), $N_{\rm obs}$ is the number of observations, $N_{\rm incl}$ is the number of observations included in the fit, and $n_{\rm par}$ is the number of fitted parameters. During the fit, we also excluded observations according to the 3σ rule (i.e., we exclude the ith observation for each $p_i(O_i - C_i)^2 > 3^2 \sum_j \frac{p_j (O_j - C_j)^2}{(N_{incl} - n_{par})}$). We also estimated the number of local maxima of the fitted solution, and if it equaled 1, we doubled the period.

For each Fourier series k, we found $f_{\min}^k$, which gave the minimal σ value from Equation (3) for the particular k. To choose the final solution among these five values for k (i.e., $k = 2$–6, inclusive), we used the F-test for each pair of models

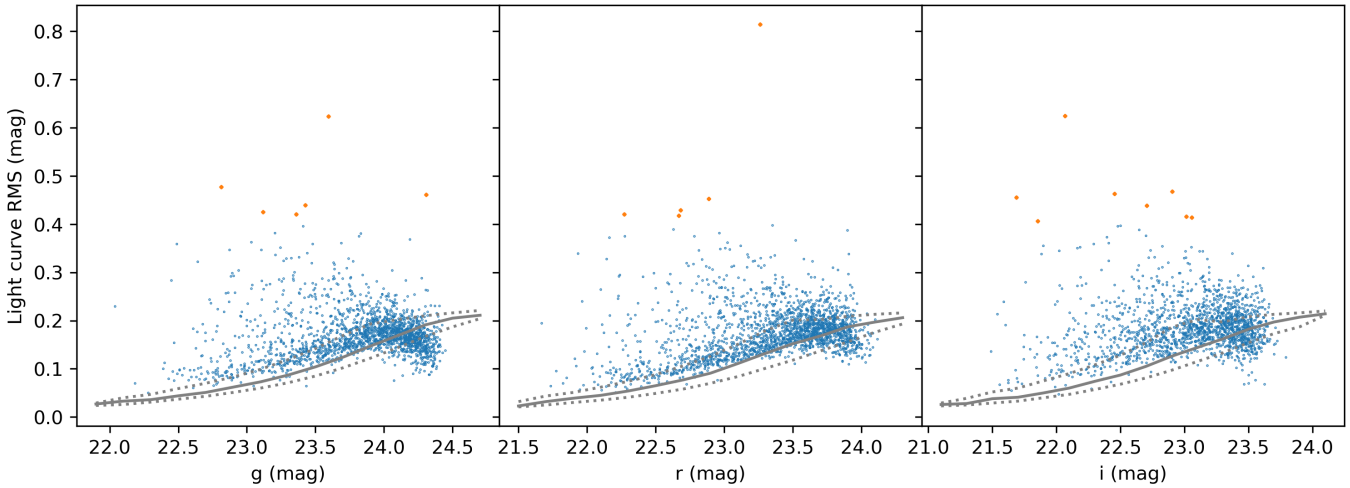

Figure 7. The rms variability as a function of magnitude, for each of the 2103 objects in the Rubin First Look dataset. The three panels correspond to the g, r, and i bands (too few u-band observations were available for analysis). Each point represents an object's rms variability in its magnitude change across the available photometric data vs. median magnitude. Points with rms > 0.4 mag are enlarged and colored red for emphasis. The gray solid line shows the median magnitude error as reported by the pipeline. The majority of points lie above the gray lines, indicating variability beyond what one would expect owing to photometric measurement uncertainty. The downturn at the faint end is an observational bias: objects with less variability are more easily detected near the magnitude limit (details in text).

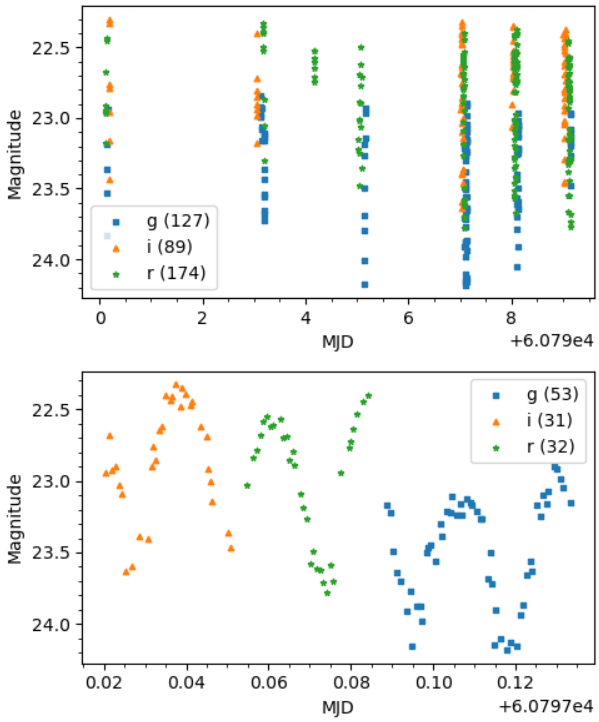

Figure 8. Magnitude over time for Rubin First Look solar system object discovery 2025 MM_{81}, both for the full observation period (top) and zoomed in on a single night (bottom) to see the magnitude variation. Observations were taken in g, r, and i bands; the number of observations in each band is shown in the legend. The amplitude of the magnitude variation ($\simeq$1.2 mag), the object's rotation period ($\simeq$0.045 days $\simeq$ 1.1 hr), and even its colors (e.g., $g - r \simeq 0.6$) can be determined directly from the raw photometry from a single night of observations.

to compute the probability (p-value) that the first model is better than the second one. We chose the model with the minimal number of parameters (minimal k) so that all the other models were not significantly better (has p-values with the chosen one less than 90%).

For the chosen model, we also computed the sigma threshold. Using the F-test, we computed the sigma level at which the chosen model was 95% better (p-value $= 0.95$) than the other models with higher σ value, making this our threshold. All the solutions with the same Fourier order k whose σ values were lower than the computed sigma threshold were considered as possible solutions. From this sigma level, we estimated the uncertainty of the resulting period and noted the possible other solutions that also fell below the sigma threshold. If there were a lot of possible solutions and the uncertainty was large, that meant that the result could not be trusted.

To define a set of reliable results, we selected only those for which the period uncertainty did not exceed either twice the period itself or 7 hr—whichever was larger. Even if other possible period solutions fell below the sigma threshold, as long as all possible solutions fell within a constrained uncertainty range, we consider the fit reliable, choosing the best fit as the determined period. In addition, for those objects with rotation periods determined to be reliable, we found that the parameters derived from the fits across this uncertainty range, such as lightcurve amplitude and absolute magnitude offsets, varied little, furthering the reliability of the determined rotation period.

Once we chose the final model, we numerically computed the maximal and minimal values of the $g(t)$ function given by Equation (2). Using the mean phase angle computed for each observation included in the fit, we calculated the amplitude of the lightcurve as the difference between this maximal and minimal value.

In addition to determining the rotation periods for all $\sim$2000 asteroids in the RFL data release, we derive asteroid colors. For the high-order Fourier analysis, this is straightforward and essentially a by-product of our fitting procedure. The absolute magnitude H values are functions computed for each observational $ugri$ filter for the lightcurve fit. The difference in H values between bands naturally corresponds to the asteroid color indices.

3.2. The Multiband Lomb–Scargle Approach

As mentioned at the start of Section 3, the vast majority of the ∼2000 asteroids released as part of the RFL event are objects newly discovered by the Rubin Observatory. As such, they do not have known rotation periods that can be used for comparison with our results. Thus, in order to assess our determined rotation period robustness, we employed two independent methods and used the results of both methods to determine the reliability threshold of our computed rotation periods.

Our second method of rotation period determination used the Lomb−Scargle Multiband (LSM) periodogram and followed a similar methodology to that described in Z. Li et al. (2025). Here we provide a brief explanation of the algorithm and refer the reader to the original paper for additional details. First, we utilized the MPC (B. D. Warner et al. 2009) to correct the data for the observational effects due to heliocentric and topocentric distance by subtracting the MPC-predicted V-band magnitudes from the observed magnitudes and then normalizing these differences by the median. We also removed the outliers with corrected magnitudes that were more than three standard deviations away from the mean. Since the MPC calculates the predicted V-band magnitude using the H–G magnitude system (E. Bowell et al. 1989), it might not capture the phase behavior of asteroids with unique characteristics or thus correct for phase angle accurately. However, given the 12-day time span of the observations in the dataset, the phase angle α does not change significantly for any of the ∼2000 asteroids in our dataset, as described in Section 3.1.

We then used the LSM periodogram (J. T. VanderPlas & Ž. Ivezić 2015) to search for periodic signals in the lightcurves. The rotational modulation $g(t)$ corresponding to the rotation of the body is represented as a Fourier series of order k equal to 2 as shown in Equation (2). We perform a dense, uniform grid search for the best periodic signal with a range between 0.00065 days (0.936 minutes) and 3 days (72 hr), allowing for the detection of rapid rotation. The number of periods in the grid search is calculated as

$$n_{\text{periods}} = \left[\left(\frac{1}{P_{\text{min}}} - \frac{1}{P_{\text{max}}}\right)(t_{\text{max}} - t_{\text{min}})\right] \times 100, \quad (4)$$

where P_{min} is the lower period bound (0.00065 days), P_{max} is the upper period bound (3 days), and $t_{\text{max}} - t_{\text{min}}$ is the total time span of the observations for the object. We include an oversample factor of 100 in Equation (4) to get a smoothly resolved periodogram.

For each period in the grid, we fit the multiband Fourier model by solving a weighted linear least-squares system and then define the Lomb–Scargle power at that period as the fractional reduction in χ^2 relative to a flat (constant-brightness) model as follows:

$$\text{Power(period)} = \frac{\chi_0^2 - \chi^2(\text{period})}{\chi_0^2}. \quad (5)$$

We refer the reader to J. T. VanderPlas & Ž. Ivezić (2015) for more details about the power spectrum calculation. After computing the Lomb–Scargle power spectrum for all periods on the grid, we identify the periods with local maxima in the power spectrum and only keep the periods that resulted in two local maxima (minima) in a phase curve, since an asteroid (an elongated body) often exhibits two maxima (minima) per cycle. The surviving period with the highest periodogram power is picked as the best rotation period of the asteroid. The amplitude of the lightcurve is calculated based on the difference between the maximum and minimum magnitudes of the fitted lightcurve using the best period.

For the derivation of colors, the LSM method simultaneously fits the same periodic signal across all photometric bands while allowing each band to have an independent magnitude. Once we determined the best periodic signal, the median magnitude of the best-fitted lightcurve for the r band was set as an offset of 0. The additional per-band fitted lightcurves were then normalized to this median r-mag and combined to provide a single fitted lightcurve. The offsets between each band were then used to calculate the $g - r$, $g - i$, and $r - i$ colors for each asteroid.

3.3. Differences between the High-order Fourier and LSM Methods

While the two rotation period determination methods described above are similar in many ways, there are a few key differences that can lead to a slight divergence in the resulting rotation period determinations and lightcurve amplitudes (which are used for color determinations) between the two methods. First is the preprocessing of the data. In the LSM method, we used the MPC's predicted V magnitude to correct for distance and phase-angle variation. In the high-order Fourier method, the observed magnitudes used distances and phase angles from JPL Horizons and manually fit the phase function. Next, both methods utilized a weighted least-squares method to fit the Fourier series to the data. However, in the LSM method, we excluded observations that are 3σ away from the mean magnitude before the fit was made, while for the high-order Fourier analysis, observation exclusions were made during the fit iterations, potentially leading to differences in the observations excluded from the lightcurve fit. The two methods also used different orders in the Fourier series: LSM considered only second-order Fourier series, while the high-order Fourier analysis considered orders $k = 2-6$, choosing the best option out of the possible fits. The powers of the fitted solutions were also calculated differently (LSM: Equation (5)); high-order Fourier: Equation (3). The LSM method additionally excluded solutions with only a single peak, choosing the peak with the highest power and two maxima within one phase. In the high-order Fourier analysis, we did not exclude possible period solutions with a single peak; however, if a single-peaked solution was found to be the best fit, the period corresponding to that single-peaked solution was doubled and chosen as the best-fit solution. These differences in the two methods could potentially lead to different best-fit rotation periods and derived amplitudes and colors resulting from the two algorithms. These potential differences are discussed in greater detail in Section 4.1 below as part of the presentation of our results.

3.4. Additional Validation

To further validate our results from the LSM and high-order Fourier analyses, we manually inspected the photometric data for each of the ∼2000 asteroids (>100 hr of work). For each object we first extracted the calibrated epochs and magnitudes

for each band (in *ugri*) and plotted magnitude versus Modified Julian Date to reveal raw brightness variations (similar to Figure 8). We then ran a simplified implementation of the LSM periodogram that included a determination of the best-fit rotation period without modeling the lightcurve to measure the fit. We examined the power versus frequency periodogram curve to pinpoint the strongest peak and converted the frequency associated with that strongest peak into the rotation period, doubling the result to account for elongated asteroid shapes that typically result in double-peaked lightcurves. Folding the observations on this period, with small vertical offsets being adjusted per band, produced phase-folded lightcurves, which we inspected by eye to confirm a coherent amplitude and shape. Those objects with reliable lightcurve shapes, amplitudes, and computed rotation periods were noted for further comparison with the results from the modeled LSM and high-order Fourier analyses, particularly noting the parameters that likely led to poor rotation period determination.

As a result, this additional step was primarily useful for determining our reliability threshold for the computed rotation periods. We found that $\lesssim$30 observations in two bands is when the computed periods became less believable in most cases. Those objects with very clear sinusoidal patterns in their photometry easily produced consistent rotation periods computed between the two methods described above and the additional manual check (e.g., the object shown in Figure 8). Objects with less clear magnitude variation in their photometry most often led to failure to determine a rotation period manually. This also most often corresponded with periods with low confidence and period differences found between the two methods described above, leading us to exclude those objects from our list of reliable rotation periods. Finally, this additional validation step also allowed us to ensure that we took notice of each of the most interesting objects in the dataset, including objects with very short rotation periods and/or large amplitudes. These objects are described in Sections 4.1.1 and 4.1.2, respectively.

4. Results and Discussion

We computed rotation periods for all 2103 solar system objects in the RFL dataset using both independent methods described above. After manually inspecting the photometric data, phased lightcurve, and fitted periodogram for each object from both our high-order Fourier and LSM analyses in coordination with the additional validation describe above, we report here the rotation periods for those objects found to meet our reliability threshold. We find that reliable rotation periods can be determined when $\geqslant$30 observations in two of the (*gri*) bands are available and modeled lightcurve amplitudes are $\geqslant$0.1 mag. Below this threshold, computed periods became less believable.

In all, we find reliable rotation periods and colors for 76 of the 2103 objects included in the RFL data release (see Table 2). Of these 76 objects, 11 were associated by the MPC with known objects (see the footnotes in Table 2 for the list of designations). The remaining 65 objects are Rubin discoveries. None of the previously known objects in this sample have known rotation periods.

Most of the 76 objects have dense coverage with hundreds of observations, taken in *g*, *r*, and *i* bands (and some sparse *u*-band observations), spanning an arc of 4–12 days. The mean magnitudes are in the range $\simeq$22–24.5 mag in *g* band and $\simeq$21.5–24 mag in both *r* and *i* bands. Figure 9 shows the residuals per band and combined for the modeled lightcurve fits versus mean magnitude from each method computed using Equation (3). The residuals are in the range 0.05–0.15 mag. Their increase with apparent magnitude is consistent with expectations given by Equation (5) in Ž. Ivezić et al. (2019) for the Rubin Observatory and the achieved limiting 5σ depth of the characterized Rubin commissioning data (from about 24.5 mag in the *g* band to about 24.0 mag in the *r* and *i* bands; Vera C. Rubin Observatory 2025). The small residuals demonstrate the photometric precision of Rubin at magnitudes fainter than many surveys are able to reach.

Unsurprisingly, since the vast majority of the solar system objects in the RFL data release are MBAs (see Figure 5), all but three of the 76 objects in this sample are MBAs; two of the remaining objects are classified as "others" by the MPC and sit just beyond the outer edge of the main belt at $a > 3.4$ au, while the final object is an Amor NEO with $a \simeq 2.1$ au. Out of curiosity owing to their sparser numbers in the RFL dataset, we carefully manually examined each of the lightcurves for the 80 non-MBAs in the data release; however, none of them were found to have reliable rotation periods above our threshold requirements. Figure 10 shows the semimajor axes, eccentricities, and inclinations for our 76-object sample. The four objects with 1.8 au $< a <$ 2 au sit near the Mars-crossing population (see Figure 5) and may be members of the Hungaria family, which have mean semimajor axes of 1.9 au, high mean inclinations of about 22°, and mean eccentricities less than 0.18 (C. E. Spratt 1990). The two "other" objects in the sample that sit outside the main belt with $a > 3.4$ au are likely to be Cybeles, which have semimajor axes between the locations of the 2:1 and 5:3 mean-motion resonances with Jupiter (V. Carruba et al. 2015). However, confirming family membership is beyond the scope of this work. As evident, the RFL dataset not only includes faint discoveries across the main belt but also has high enough photometric precision to distinguish magnitude variation, extract lightcurves, and reliably determine rotation periods for objects as faint as $m_r \simeq 23$ mag that sit beyond the far edge of the belt, an area that is sparsely sampled in studies of asteroid rotation periods.

As a note, due to the large number of asteroids in the RFL dataset, it is possible that some of the objects show signs of activity. Unfortunately, we do not have access to the images from this MPC-queried dataset to check for potential signs of activity; analyzing any such activity indicators (such as comae) is also beyond the scope of this work. However, we note that possible activity could potentially affect our ability to reliably determine rotation periods for some of the asteroids in our dataset and may account for some of the objects not included in our 76-object sample.

4.1. Lightcurve Rotation Periods and Amplitudes

Figure 11 shows the lightcurves for an example 24 objects composing 35% of our 76-object sample that exhibit rotation periods and amplitudes across the determined range (0.031–21.3 hr and up to 1 mag or more, respectively). This includes superfast rotators (with rotation periods $\leqslant$2.2 hr, discussed in Section 4.1.1) and those with large amplitudes ($\gtrsim$1 magnitude, discussed in Section 4.1.2). As mentioned in Section 4 above, the mean *r*-band magnitudes to which these lightcurves are normalized range from $\simeq$22 to 24, fainter than

Table 2

Rotation Periods, Lightcurve Amplitudes, and Colors for the 76 Objects among the 2103 Rubin First Look Solar System Object Discoveries for Which We Find Reliable Rotation Periods from Our LSM and High-order Fourier Analyses (See Section 3 for Method Details)

Designation	H Mag	Mean Mag (r Band)	Number of Observations	Arc (days)	Period (LSM/ Fourier)	Amplitude (LSM/ Fourier)	$g-r$ (LSM/ Fourier)	$g-i$ (LSM/ Fourier)	$r-i$ (LSM/ Fourier)	Axial Elongation
2025 MA_{19}	18.1	22.66	447	9	8.9 / 8.9	0.7 / 1.0	0.44 / 0.46	0.49 / 0.55	0.05 / 0.08	2.1
2025 MA_{45}[a,b]	19.5	22.50	140	12	1.6 / 1.6	0.7 / 0.6	0.35 / 0.45	0.65 / 0.60	0.30 / 0.14	1.5
2025 MA_{46}	18.1	23.13	291	12	5.9 / 5.9	0.6 / 0.6	0.53 / 0.53	0.71 / 0.68	0.18 / 0.15	1.6
2025 MC_{34}	18.5	23.02	321	12	8.4 / 8.4	0.8 / 0.9	0.52 / 0.49	0.69 / 0.70	0.16 / 0.21	1.9
2025 MD_{38}[a]	18.0	22.80	458	12	15.8 / 9.5	1.1 / 1.1	0.46 / 0.46	0.54 / 0.59	0.08 / 0.13	2.2
2025 MD_{40}	19.0	23.35	393	12	4.4 / 4.4	0.7 / 0.7	0.45 / 0.44	0.59 / 0.58	0.14 / 0.14	1.7
2025 MD_{67}[a]	18.1	22.36	232	2	7.8 / 3.3	1.2 / 0.5	0.50 / 0.51	0.72 / 0.59	0.21 / 0.07	1.4
2025 MD_{76}[a]	18.3	23.02	404	12	11.0 / 11.0	0.7 / 0.6	0.46 / 0.49	0.65 / 0.65	0.18 / 0.16	1.6
2025 ME_{15}	19.8	22.95	329	12	6.9 / 8.1	0.9 / 0.9	0.61 / 0.63	0.78 / 0.79	0.17 / 0.16	1.9
2025 ME_{24}[a]	18.4	23.32	386	12	2.9 / 4.2	0.3 / 0.4	0.51 / 0.51	0.70 / 0.70	0.19 / 0.19	1.3
2025 ME_{68}[b]	21.2	23.51	192	12	0.9 / 0.9	0.6 / 0.5	0.59 / 0.58	0.75 / 0.76	0.16 / 0.18	1.4
2025 MF_{76}[b]	18.9	21.82	244	6	2.2 / 2.0	0.2 / 0.1	0.56 / 0.58	0.75 / 0.75	0.19 / 0.17	1.1
2025 MG_{17}	17.1	22.76	289	6	4.3 / 4.3	0.4 / 0.4	0.46 / 0.46	0.59 / 0.58	0.13 / 0.13	1.3
2025 MG_{56}[b]	18.9	22.86	213	12	0.3 / 0.3	0.5 / 0.8	0.47 / 0.48	0.59 / 0.59	0.12 / 0.11	1.7
2025 MH_{40}	19.1	22.56	379	9	8.0 / 6.9	1.4 / 0.7	0.47 / 0.43	0.58 / 0.55	0.11 / 0.12	1.7
2025 MH_{69}[a]	19.1	23.12	314	12	6.7 / 7.8	0.7 / 0.7	0.63 / 0.63	0.81 / 0.93	0.18 / 0.30	1.7
2025 MH_{75}	19.0	22.67	399	12	4.2 / 4.2	0.5 / 0.4	0.58 / 0.58	0.82 / 0.83	0.23 / 0.24	1.3
2025 MH_{86}	18.2	23.00	456	12	4.4 / 4.4	0.5 / 0.5	0.44 / 0.44	0.54 / 0.53	0.10 / 0.09	1.5
2025 MJ_{13}	20.9	23.06	116	12	3.4 / 3.1	0.6 / 0.9	0.46 / 0.32	0.48 / 0.82	0.02 / 0.50	1.8
2025 MJ_{21}	18.8	22.22	262	4	3.4 / 3.9	0.3 / 0.3	0.43 / 0.40	0.49 / 0.50	0.06 / 0.10	1.2
2025 MJ_{23}	17.9	22.69	121	2	7.4 / 5.2	0.8 / 0.9	0.64 / 0.56	0.71 / 0.767	0.06 / 0.21	2.0
2025 MJ_{30}	18.0	22.82	291	12	5.6 / 5.6	0.5 / 0.5	0.50 / 0.50	0.67 / 0.68	0.16 / 0.17	1.4
2025 MJ_{71}[a,b]	22.70	23.44	272	6	0.031 / 0.031	0.4 / 0.4	0.58 / 0.58	0.78 / 0.76	0.20 / 0.18	1.3
2025 MJ_{79}[b]	20.0	23.92	70	6	1.0 / 0.4	0.2 / 0.2	0.47 / 0.42	0.65 / 0.71	0.18 / 0.3	1.2
2025 MK_{23}	20.4	22.58	112	12	6.2 / 10.6	0.9 / 1.7	0.65 / 0.56	0.63 / 0.77	-0.02 / 0.2	3.1
2025 MK_{41}[b]	19.3	22.17	426	12	0.063 / 0.063	0.2 / 0.3	0.41 / 0.40	0.55 / 0.56	0.14 / 0.16	1.2
2025 MK_{68}	19.1	22.16	147	2	5.0 / 5.0	0.7 / 0.6	0.50 / 0.63	0.58 / 0.81	0.08 / 0.18	1.5
2025 MK_{83}	20.1	22.77	333	12	6.1 / 6.1	0.5 / 0.5	0.58 / 0.55	0.73 / 0.67	0.14 / 0.12	1.4
2025 MK_{88}[a]	18.4	23.19	234	12	2.7 / 2.5	0.4 / 0.4	0.60 / 0.62	0.80 / 0.84	0.20 / 0.22	1.4
2025 ML_{10}[a]	18.3	23.20	294	6	7.0 / 7.0	1.0 / 1.1	0.50 / 0.54	0.57 / 0.64	0.07 / 0.10	2.2
2025 ML_{17}	18.5	23.28	255	12	6.7 / 6.7	0.6 / 0.6	0.37 / 0.40	0.48 / 0.49	0.10 / 0.10	1.5
2025 ML_{35}	19.4	23.10	411	12	21.3 / 21.3	0.8 / 1.0	0.54 / 0.58	0.78 / 0.82	0.24 / 0.24	2.0
2025 ML_{52}	18.8	22.91	436	12	11.5 / 9.2	0.7 / 0.7	0.54 / 0.55	0.67 / 0.75	0.13 / 0.20	1.7
2025 ML_{53}	18.4	22.83	121	12	5.2 / 7.0	0.7 / 0.8	0.38 / 0.42	0.63 / 0.64	0.25 / 0.21	1.8
2025 MM_{37}[b]	19.6	22.40	305	9	3.7 / 1.9	0.3 / 0.3	0.52 / 0.48	0.58 / 0.59	0.06 / 0.11	1.2
2025 MM_{81}[b]	21.1	22.90	390	9	1.1 / 1.1	1.0 / 1.2	0.55 / 0.53	0.67 / 0.66	0.12 / 0.12	2.1
2025 MM_{82}	19.0	22.96	412	12	5.0 / 5.0	0.8 / 0.9	0.73 / 0.74	0.88 / 0.83	0.15 / 0.09	1.9
2025 MN_{25}[b]	20.5	22.95	318	12	0.4 / 0.4	0.4 / 0.4	0.42 / 0.41	0.51 / 0.54	0.08 / 0.13	1.3
2025 MN_{37}	17.8	22.20	424	9	4.8 / 6.8	0.8 / 0.9	0.56 / 0.54	0.73 / 0.75	0.18 / 0.21	2.0
2025 MN_{45}[b]	18.7	22.24	517	12	0.031 / 0.031	0.4 / 0.4	0.43 / 0.42	0.56 / 0.57	0.13 / 0.14	1.3
2025 MN_{7}	18.1	23.00	347	12	6.8 / 10.6	0.7 / 0.7	0.47 / 0.47	0.62 / 0.59	0.15 / 0.12	1.7
2025 MO_{35}	18.4	22.37	417	12	6.3 / 6.3	0.5 / 0.5	0.57 / 0.56	0.71 / 0.71	0.14 / 0.15	1.4
2025 MO_{39}	19.3	22.84	141	2	4.9 / 6.2	0.9 / 1.0	0.46 / 0.37	0.47 / 0.44	0.01 / 0.07	1.9
2025 MO_{47}	18.5	23.43	279	12	9.1 / 9.1	0.7 / 0.7	0.44 / 0.43	0.72 / 0.74	0.28 / 0.31	1.7
2025 MO_{79}	20.1	23.27	122	9	5.5 / 2.7	0.6 / 0.6	0.57 / 0.62	0.69 / 0.71	0.12 / 0.09	1.6
2025 MP_{21}	17.9	22.67	314	12	6.2 / 5.5	0.6 / 0.5	0.52 / 0.54	0.65 / 0.72	0.13 / 0.17	1.5
2025 MP_{47}[a,b]	18.8	22.73	398	12	4.9 / 2.2	0.4 / 0.3	0.43 / 0.47	0.48 / 0.62	0.04 / 0.15	1.2
2025 MP_{61}	18.4	23.51	268	9	3.0 / 5.6	0.6 / 0.7	0.49 / 0.55	0.70 / 0.70	0.21 / 0.15	1.7
2025 MP_{67}	19.0	22.75	194	4	4.1 / 6.2	0.7 / 0.7	0.63 / 0.62	0.79 / 0.83	0.16 / 0.21	1.6
2025 MP_{71}	18.3	22.23	359	12	9.1 / 9.1	0.4 / 0.4	0.57 / 0.57	0.83 / 0.78	0.25 / 0.20	1.4
2025 MQ_{58}	18.4	23.11	314	12	2.9 / 3.1	0.3 / 0.4	0.60 / 0.65	0.78 / 0.74	0.18 / 0.10	1.3
2025 MR_{33}	18.3	22.40	490	12	3.5 / 3.5	0.3 / 0.2	0.68 / 0.66	0.83 / 0.87	0.15 / 0.21	1.2
2025 MS_{34}	18.3	23.05	292	6	2.3 / 2.3	0.5 / 0.5	0.59 / 0.58	0.74 / 0.75	0.15 / 0.17	1.4
2025 MS_{7}	18.5	23.04	114	2	4.6 / 4.6	0.8 / 0.7	0.49 / 0.47	0.58 / 0.56	0.09 / 0.08	1.7
2025 MT_{24}	17.8	22.15	408	9	8.9 / 8.9	1.0 / 1.1	0.63 / 0.49	0.64 / 0.62	0.01 / 0.13	2.2
2025 MU_{10}	20.6	22.32	450	6	6.5 / 6.5	0.5 / 0.5	0.52 / 0.52	0.67 / 0.66	0.15 / 0.14	1.3
2025 MU_{15}[b]	21.6	23.53	182	12	0.4 / 0.4	0.5 / 0.5	0.50 / 0.48	0.69 / 0.69	0.19 / 0.21	1.4
2025 MU_{24}[b]	18.7	22.79	475	6	2.2 / 2.2	0.3 / 0.2	0.66 / 0.64	0.80 / 0.80	0.13 / 0.16	1.2

Table 2
(Continued)

Designation	H Mag	Mean Mag (r Band)	Number of Observations	Arc (days)	Period (LSM/ Fourier)	Amplitude (LSM/ Fourier)	$g-r$ (LSM/ Fourier)	$g-i$ (LSM/ Fourier)	$r-i$ (LSM/ Fourier)	Axial Elongation
2025 MU_{59}	19.0	22.00	503	12	8.2 / 8.2	0.6 / 0.6	0.54 / 0.58	0.79 / 0.77	0.25 / 0.20	1.5
2025 MU_{8}[b]	19.0	23.22	276	12	0.8 / 0.8	0.6 / 0.6	0.47 / 0.46	0.58 / 0.58	0.12 / 0.12	1.5
2025 MU_{9}	18.4	22.72	324	6	4.9 / 3.5	0.6 / 0.7	0.48 / 0.47	0.61 / 0.57	0.13 / 0.10	1.7
2025 MV_{19}	18.0	22.60	254	6	7.4 / 7.4	0.7 / 0.7	0.46 / 0.46	0.68 / 0.66	0.23 / 0.20	1.7
2025 MV_{31}	18.8	22.98	277	6	5.2 / 5.8	0.7 / 0.6	0.43 / 0.54	0.71 / 0.67	0.27 / 0.13	1.6
2025 MV_{38}	17.9	22.91	241	6	6.0 / 6.0	0.6 / 0.6	0.68 / 0.68	0.86 / 0.91	0.18 / 0.23	1.6
2025 MV_{4}	19.6	23.36	350	12	5.9 / 5.3	0.8 / 0.6	0.47 / 0.48	0.58 / 0.64	0.11 / 0.16	1.5
2025 MV_{46}	17.8	22.47	502	12	3.4 / 3.4	0.2 / 0.1	0.55 / 0.52	0.70 / 0.67	0.15 / 0.15	1.1
2025 MV_{71}[b]	18.2	22.74	334	12	0.2 / 0.2	0.4 / 0.6	0.44 / 0.43	0.57 / 0.57	0.13 / 0.13	1.6
2025 MW_{70}	18.5	22.45	265	12	3.9 / 3.9	0.2 / 0.3	0.63 / 0.62	0.90 / 0.90	0.28 / 0.28	1.2
2025 MX_{34}	19.4	22.37	174	2	5.8 / 4.7	0.7 / 0.8	0.67 / 0.63	0.91 / 0.83	0.23 / 0.20	1.7
2025 MX_{44}[a,b]	17.9	23.21	488	12	1.1 / 1.2	0.2 / 0.3	0.41 / 0.42	0.56 / 0.54	0.16 / 0.12	1.3
2025 MX_{50}[b]	19.8	22.14	432	12	1.9 / 1.9	0.3 / 0.3	0.64 / 0.63	0.81 / 0.83	0.17 / 0.20	1.2
2025 MX_{63}	19.1	23.22	327	9	8.3 / 8.3	0.7 / 0.5	0.60 / 0.59	0.80 / 0.79	0.20 / 0.20	1.4
2025 MX_{69}	19.2	22.51	213	4	9.1 / 7.7	0.7 / 1.3	0.52 / 0.49	0.53 / 0.56	0.01 / 0.06	2.4
2025 MY_{23}	18.9	22.10	199	12	3.1 / 3.1	0.2 / 0.2	0.57 / 0.58	0.72 / 0.72	0.15 / 0.14	1.1
2025 MY_{77}	18.1	22.51	258	6	7.6 / 7.6	1.0 / 1.1	0.60 / 0.61	0.80 / 0.91	0.20 / 0.30	2.2
2025 MZ_{78}[b]	17.8	23.21	167	4	1.2 / 1.2	0.5 / 0.5	0.46 / 0.46	0.58 / 0.60	0.12 / 0.14	1.5

Notes. In addition, we compute an estimate of the axial elongation of each object given its lightcurve amplitude (see Section 4.1.2)
[a] 11 objects were associated by the MPC with known objects (none have known rotation periods): MA_{45}=2015 KR_{298}, MD_{38}=2014 HR_{48}, MD_{67}=2015 FU_{236}, MD_{76}=2021 PA_{196}, ME_{24}=2014 HT_{395}, MH_{69}=2016 PW_{289}, MJ_{71}=2022 CJ_{2}, MK_{88}=2022 SZ_{331}, ML_{10}=2015 KP_{348}, MP_{47}=2015 UC_{70}, and MX_{44}=2016 UO_{174}.
[b] "Rubin superfast rotator" (rotation period $\leqslant$2.2 hr computed from at least one of the LSM/Fourier methods).

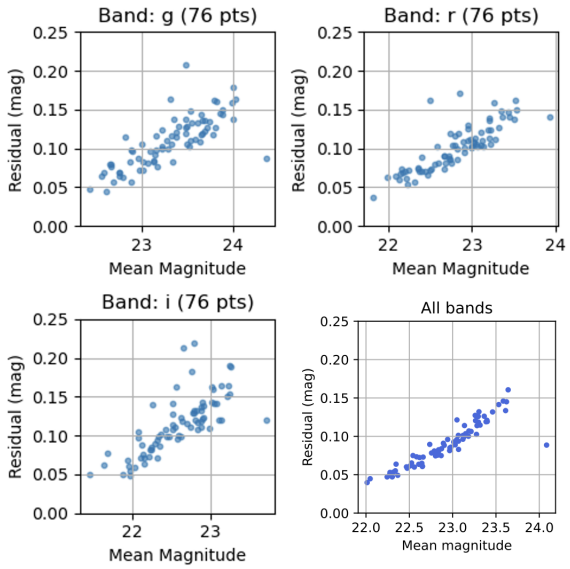

Figure 9. Top and bottom left: magnitude residuals for the lightcurve fit from the LSM approach vs. mean magnitude for the g, r, and i bands individually. Bottom right: magnitude residuals for the lightcurve fit from the high-order Fourier analysis vs. mean magnitude for all bands combined. The residuals for both methods were obtained using Equation (3). The residuals are in the range 0.05–0.15 mag. Their increase with apparent magnitude is consistent with expectations given in Ž. Ivezić et al. (2019; their Equation (5)) and the achieved limiting 5σ depth of the characterized commissioning data (from $\approx$24.5 mag in the g band to 24.0 mag in the r and i bands; Vera C. Rubin Observatory 2025).

is typically provided by other surveys for rotation period determination of MBAs. As evident in the figure, several of the observed lightcurves for the objects in our sample are asymmetrical or have sharp features. A discussion of the implications of these features can be found in Section 4.1.2. The full set of fitted lightcurves and periodograms extracted using the two methods we employ for the 76 objects in our sample can be found in Appendix B.

Figure 12 shows the rotation period as a function of absolute magnitude H and lightcurve amplitude for the 76 objects included in our sample. The blue points were computed using the LSM approach, while the orange points were determined using the high-order Fourier analysis. Our sample covers a range of H magnitudes from $\simeq$17.1 to $\simeq$22.7. The majority of our derived rotation periods are <10 hr, with a few outliers out to periods $\approx$21 hr. We discuss the objects found to be rotating faster than the 2.2 hr spin barrier in Section 4.1.1. We find lightcurve amplitudes for our sample ranging from $\approx$0.15 to 1.7, with the majority falling between 0.2 and 0.8 (see Section 4.1.2 for further discussion). The rotation periods we derive using the two methods described in Section 3 agree for most objects in our sample and thus overlap in the left panel of Figure 12. Our calculated amplitudes differ by a slightly wider margin than the rotation periods owing to the differences in lightcurve fits utilized in the two analyses.

The right panel of Figure 12 shows a comparison of the computed rotation periods determined from the LSM and high-order Fourier analyses. As evident, the majority (67%) of the rotation periods computed with the two methods employed agree to within 10%. The remaining objects agree to within a factor of $\simeq$2; this level of uncertainty is common since it can be difficult at times to distinguish between rotation periods that are low-order integer multiples of each other. The 33% of objects that have rotation period differences $>$10% most often have multiple possible periods returned from both determination methods. In these cases, each method tends to pick out a

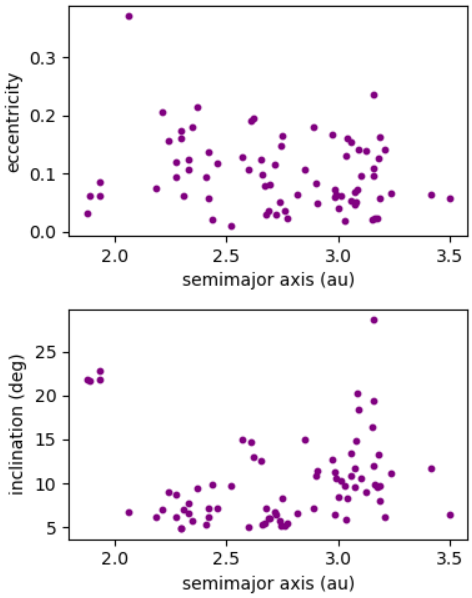

Figure 10. Semimajor axis, eccentricity, and inclination for the 76 objects in the 2103-object RFL dataset for which we determine rotation periods and colors from their lightcurves. All but three of the 76 objects are MBAs; two of the remaining objects are classified as "others" by the MPC and sit just beyond the outer edge of the main belt at $a > 3.4$ au, while the final object is an Amor NEO with $a \simeq 2.1$ au; see Figure 5). The high photometric precision of the dataset allows for distinguishing magnitude variation, extracting lightcurves, and reliably determining rotation periods for low-eccentricity objects as faint as $m_r \simeq 23$ mag that sit beyond the far edge of the main belt where studies of asteroid rotation periods are sparsely sampled.

different, but nearby, best fit for the rotational period out of the possible periods with the highest probabilities. We provide the additional possible rotation periods for each object in our sample in Appendix B.

An example of an object with multiple possible periods for which the two methods pick out different peaks in the periodogram is 2025 MJ_{79}, shown in the left two panels of Figure 13. Despite the multiple possible rotation periods, all acceptable possibilities are very closely clumped together and cover a very short range of frequencies. In addition, all the possible periods are very short, with the LSM method picking out a best-fit period of 0.6 hr and the Fourier analysis selecting a best-fit period of 1.0 hr, agreeing to within a factor of ≈2 and confirming that this object is a superfast rotator. Interestingly, MJ79 has the faintest mean r-magnitude (23.9) in our sample. The ability to distinguish a rotation period for an object of this faint magnitude, particularly a superfast rotation with a relatively small amplitude (0.2 mag), demonstrates the precision of Rubin's photometry and capability to extend rotation period determination to fainter MBAs.

4.1.1. Fast Rotators

Due to the nature of the commissioning observations included in this dataset (as described in Section 1.2 above), Rubin did not follow a fixed cadence (e.g., imaging every n hours), but instead observed with dense temporal sampling under an irregular cadence driven by commissioning. This irregular density leads to a very high effective Nyquist-like frequency (as defined in L. Eyer & P. Bartholdi 1999), allowing the detection of extremely fast rotating asteroids with rotation periods of ∼minutes. Although the exact value of this frequency depends on the specific timing of the given observations, in practice it is often well above 240 cycles day^{-1} (less than a 0.1 hr period), significantly expanding the range of detectable rotational periods within the dataset.

As shown in Table 2, the rotation periods for our 76-object Rubin sample range from 0.031 to 21.3 hr. As evident from Figure 12, 19 of the 76 asteroids have rotation periods ⩽2.2 hr from at least one of our two analyses (see Table 2). This critical spin period corresponds to that at which self-gravity and centrifugal acceleration are balanced and is referred to as the "spin barrier." Hereafter we refer to these 19 objects as the "Rubin superfast rotators."

Of particular interest are 2025 MN_{45}, 2025 MJ_{71}, 2025 MK_{41}, 2025 MV_{71}, and 2025 MG_{56} (rotation periods of ≃1.88, ≃1.92, ≃3.78, ≃13, and ≃16 minutes, respectively). The photometric data, phased lightcurves, and periodograms for MN45, MJ71, and MK41 are shown in Figure 13, and the phased lightcurves for MV71 and MG56 can be found in Figure 11. With rotation periods of <5 minutes, MN45, MJ71, and MK41 belong in a category all their own, which we call "ultrafast rotators."

We estimate the diameters of these five objects assuming a spherical shape from the following equation (E. Bowell et al. 1989):

$$d = \frac{1329}{\sqrt{\alpha}} 10^{-0.2H}, \quad (6)$$

where the geometric albedo α is assumed to be 0.15 and H is the absolute magnitude in the i band. The four MBAs (MN45, MK41, MV71, and MG56) have relatively large (>0.5 km) estimated diameters ($d \simeq 0.71$ km, $d \simeq 0.54$ km, $d \simeq 0.93$ km, and $d \simeq 0.66$ km, respectively), while the Amor NEO MJ71 is smaller ($d \simeq 0.12$ km).

From a search of the NASA Small-Body Database,[45] as of 2025 July 29, there are four $H < 20$ asteroids with reported rotation periods shorter than or near those we computed for MN45, MK41, MV71, and MG56. Those asteroids, their H magnitudes, and their rotation periods, respectively, are as follows: Apollo near-Earth asteroid (NEA) 2019 MA_2 ($H = 18.91$, $P = 0.044$ hr), MBA (305454) 2008 DP_4 ($H = 16.39$, $P = 0.061$ hr), Amor NEO (285625) 2000 RD_{34} ($H = 17.91$, $P = 0.065$ hr), and MBA (27346) 2000 DN_8 ($H = 15.88$, $P = 0.068$ hr). The comments provided with the reported rotation periods for the last three of these four asteroids indicate that the results are "incomplete," "inclusive," and "based on fragmentary lightcurves" and "may be completely wrong." The comment provided with the period for MA2 reports "less than full coverage of the lightcurve and an uncertainty of ∼30% for the period." Regardless of whether the rotation periods for these four objects with known rotation periods are considered to be reliable, the four fastest-rotating Rubin-discovered MBAs, particularly MN45 and MK41 with rotation periods <3 minutes, confirm that $d > 0.5$ km asteroids can have rotation periods of the order of a few minutes. This also makes Rubin-discovered MBA MN45 the fastest-spinning asteroid with $H < 20$, rotating once every ≈1.88 minutes. Given the exceptional nature of their rapid rotation, we performed extensive validation on MN45, MJ71, and MK41, confirming the robustness of their determined periods across multiple nights of observations and photometric bands (see Appendix C for details).

[45] https://ssd.jpl.nasa.gov/tools/sbdb_query.html

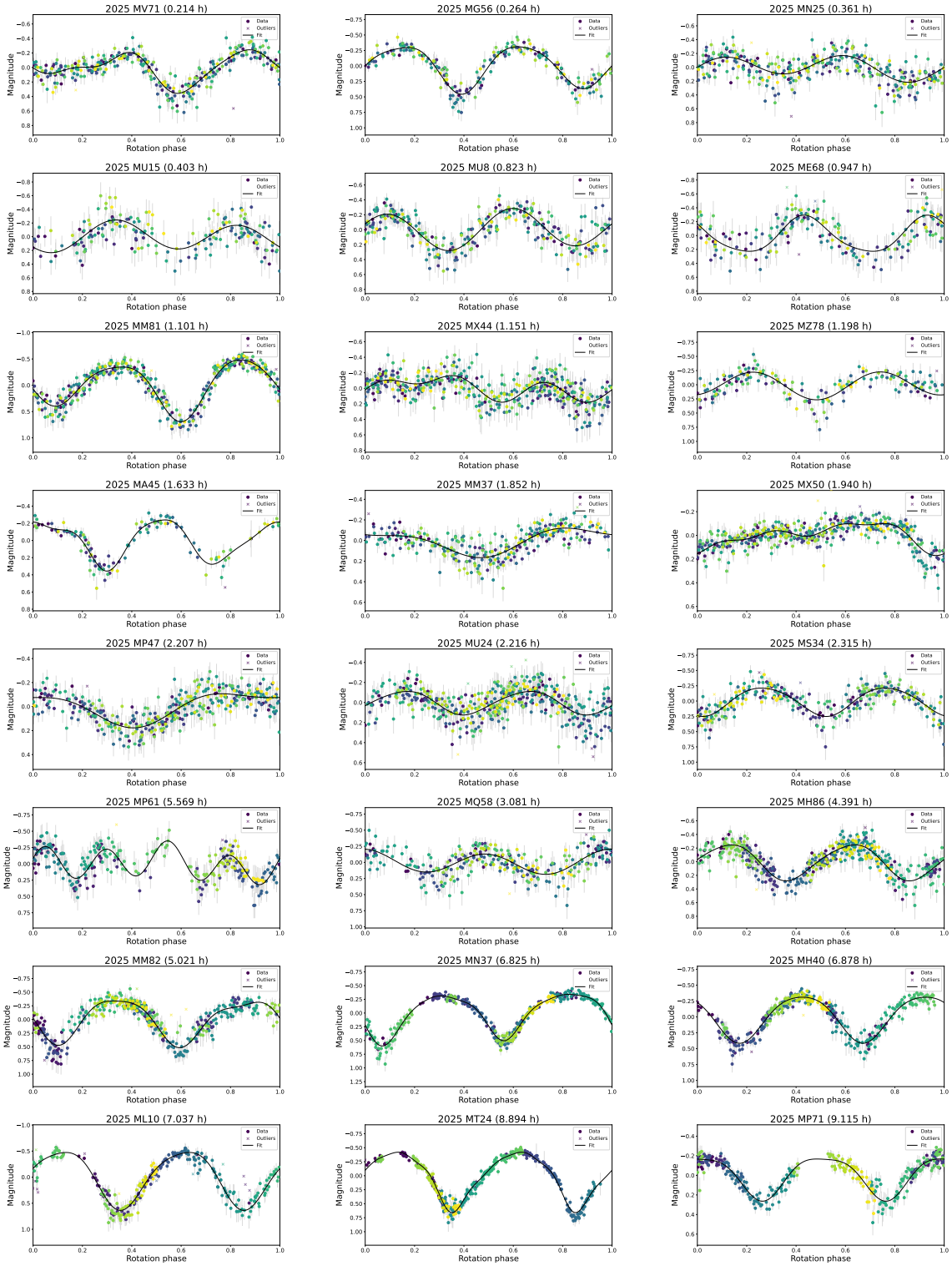

Figure 11. Lightcurves for 24 selected MBAs (shown here modeled using our high-order Fourier analysis), composing 35% of the total Rubin-observed sample for which we produce reliable lightcurves and determine rotation periods (76 objects in total), ordered by rotation period. The colored points show the data as a function of time color-coded by epoch, with purple points corresponding to the first night of observations and light green points corresponding to the last night of observations (see Figure 13 for examples of the observational color-coding by epoch). The examples shown here span nearly the full range of detected periods and amplitudes, including 12 superfast rotators (periods $\leqslant$2.2 hr) and high-amplitude ($\geqslant$1 magnitude) cases; three additional ultrafast rotators are shown in Figure 13. The mean *r*-band magnitudes used for normalization range from $\simeq$22 to 24 mag, fainter than is typically provided by other surveys for rotation period determination of MBAs.

Following P. Sánchez & D. J. Scheeres (2014), we can estimate the cohesive strength necessary to avoid disruption for all 19 of the Rubin superfast rotators. The following inequality for the critical rotation frequency (ω_{crit}) indicates where disruption occurs, that is, when

$$\omega_{\rm crit}^2 \leqslant \omega_\alpha^2 + \frac{2}{\rho\ \alpha^2}\left(\frac{3-\sin\phi}{3+\sin\phi}\right)\sigma_Y. \tag{7}$$

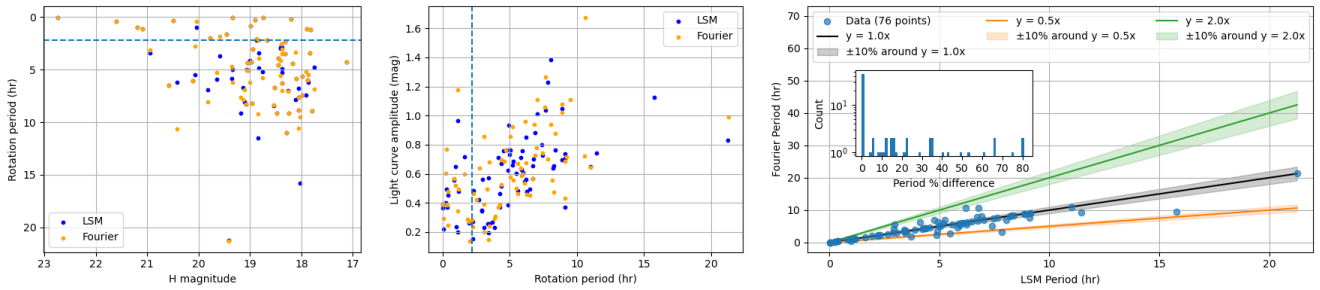

Figure 12. Left: rotation period as a function of absolute magnitude (H magnitude) for the 76 objects included in our sample. The blue points were computed using the LSM approach, while the orange points were determined using the high-order Fourier analysis. The majority of the computed rotation periods agree to within 10% between the two methods employed and thus overlap in the plot (see right panel). The horizontal dashed line at 2.2 hr marks the critical spin period at which self-gravity and centrifugal acceleration are balanced and is referred to as the "spin barrier." Middle: lightcurve amplitude as a function of rotation period for the 76 objects included in our sample. The blue points were computed using the lightcurve fit from the LSM method, while the orange points were determined using the fit from the high-order Fourier analysis (see Section 3.3 for a description of the differences in the amplitude calculations between these two methods). Right: comparison of rotation periods computed for the 76 objects in Table 2 using the two employed methods. The black curve shows agreement between the two computed rotation periods, with the gray region marking agreement within 10%. The green and orange curves denote a factor of two difference between the computed periods, with either the Fourier period being twice that of the LSM period (green) or the LSM period computed as twice that from the Fourier analysis (orange). The inset shows a histogram of the percent difference in the periods between the two methods; note the log scale. A total of 67% of the 76 objects have computed rotation periods that agree to within 10%. The remaining 33% are those for which multiple possible rotation periods were determined (see text and Appendix B), with the best-fit periods determined by both methods agreeing to within roughly a factor of 2.

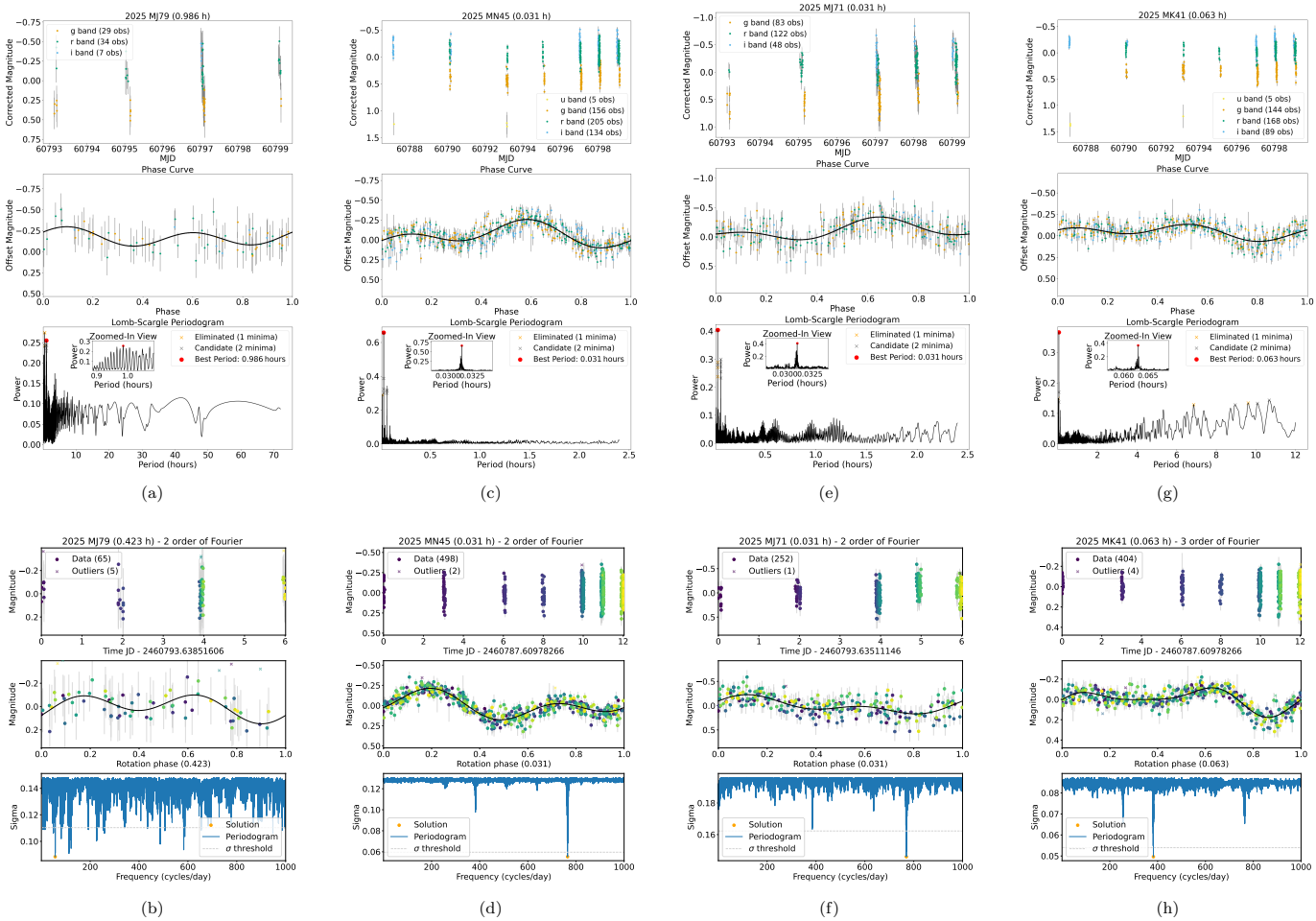

Figure 13. Lightcurves for four selected objects in our Rubin data sample. (a, b) Example of an object (2025 MJ_{79}) with multiple possible, nearby rotation periods for which the LSM (panel (a)) and high-order Fourier (panel (b)) analyses picked out slightly different best-fit rotation periods. Panels (c)–(h) depict the three fastest-rotating asteroids found in the RFL dataset: Rubin discovered MBAs 2025 MN_{45} (1.88-minute rotation period; panels (c) and (d)), 2025 MK_{41} (3.78-minute period; panels (g) and (h)) and Amor NEO 2025 MJ_{71} (1.92-minute rotation period; panels (e) and (f)). Panels (a), (c), (e), and (g) show results from the LSM approach, while panels (b), (d), (f), and (h) show results from the high-order Fourier analysis. The upper subpanel of each panel shows the unfolded photometry (with observations color-coded by band (LSM) and epoch (Fourier)). The middle subpanels show the phased lightcurve folded at the labeled rotation period with the offset magnitude of zero set to the median magnitude of the lightcurve fitted for the r-band observations. The bottom subpanels of panels (a), (c), (e), and (g) show the Lomb–Scargle periodogram, with an inset of the zoomed-in view of the best-fit peak; the bottom subpanels of panels (b), (d), (f), and (h) show the periodogram with the residual of the fit for the high-order Fourier analysis as a function of the rotation frequency, with the horizontal dashed line corresponding to the significance level (sigma threshold).

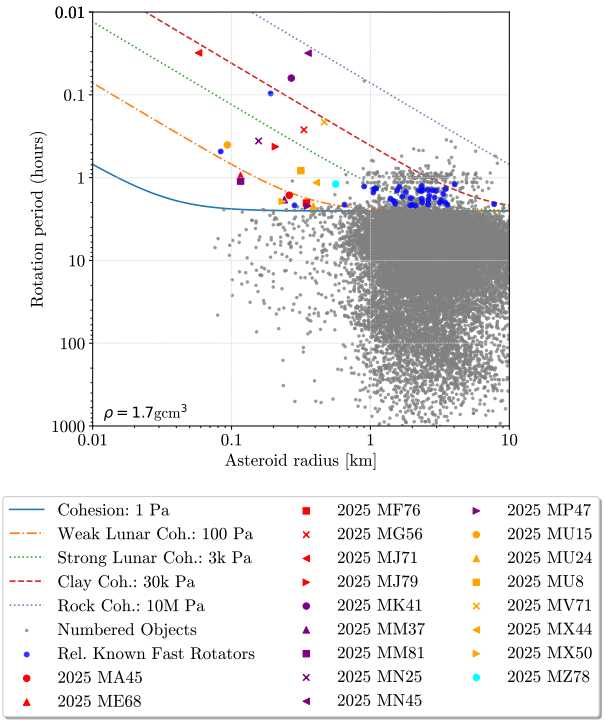

Figure 14. Asteroid size vs. rotation period for numbered asteroids (gray circles) and the 19 Rubin superfast rotators. Blue circles represent known objects with reliable spin periods (uncertainties below 30% based on data from NASA JPL (2025)) that rotate above the so-called "spin barrier" indicated by the level curves for various values of cohesive strengths. Rubin superfast rotator 2025 MG_{56} lies beyond the Strong Lunar Cohesion model, and 2025 MV_{71} along with ultrafast rotators 2025 MJ_{71}, 2025 MK_{41}, and 2025 MN_{45} even farther beyond to required cohesive strengths of clay or rock.

Here ρ is the bulk density of the asteroid, α is the largest semimajor axis of the closest fitting triaxial ellipsoid with $\alpha \geqslant \beta \geqslant \gamma$, ϕ is the internal friction angle of the material, σ_Y is the yield strength of the material, and

$$\omega_\alpha^2 = \frac{3}{2} GM \int_0^\infty \frac{dx}{(\alpha^2 + x)\sqrt{(\alpha^2 + x)(\beta^2 + x)(\gamma^2 + x)}}, \tag{8}$$

which represents the gravitational contribution from the ellipsoidal mass distribution; GM represents the mass parameter of the asteroid. A conservative limit for Equation (7) can be derived by assuming a spherical body, i.e., $\alpha = \beta = \gamma$, and realizing that the term proportional to the yield strength will be greatest for $\phi = \pi/2$, but only by a factor of 2 over $\phi = 0$. In this case, the integral in Equation (8) reduces to

$$\omega_\alpha^2 \approx \frac{4}{3}\pi G\rho, \tag{9}$$

and Equation (7) simplifies to

$$\omega_{\mathrm{crit}}^2 \leqslant \frac{4}{3}\pi G\rho + \frac{\sigma_Y}{\rho\alpha^2}. \tag{10}$$

The first term on the right-hand side in Equation (10) only depends on the bulk density ρ and leads to the asymptotic behavior for large asteroids and low cohesive strength, as shown in Figure 14. Here spin-based disruption limits are shown as level curves for various cohesive strengths σ_Y. A bulk density of $\rho = 1700$ kg m^{-3} was assumed in plotting these curves, typical of the most common type of rocky asteroids. The so-called "spin barrier" manifests itself as a plateau where the disruption curves assuming low cohesive strength flatten out for larger asteroid sizes. The known population of fast rotators is shown in blue, while all other asteroids with known rotation periods are shown as gray circles. Rubin superfast rotators are depicted individually.

Most of the fast rotators fall below the Strong Lunar Cohesion limit (3 kPa). Five of the Rubin superfast rotators are exceptions, requiring higher cohesions to survive under current model assumptions. MG56 would require a cohesive strength of $\simeq$12 kPa, MV71 and ultrafast rotator MJ71 would require higher strengths of just under $\simeq$30 kPa, and ultrafast rotators MK41 and MN45 would require even higher strengths of roughly 0.9 and 9 MPa, respectively, to avoid disruption. While these cohesive strengths are larger than would be needed for many asteroids with known rotation periods, as shown in Figure 14, these values are not outside the realm expected for objects with high strength and are consistent with those expected for clay or rock. As the cohesive strength curves in the figure indicate, there are no physical restrictions for sub-kilometer-sized objects to rotate with periods $<$1 hr or faster; these objects are simply most likely to be rare (B. D. Warner & R. D. Stephens 2020), suggesting unusual compositions, internal structures, or formation histories. For comparison, in a search of the DECam Ecliptic Exploration Project (DEEP) dataset for superfast rotators among the DEEP-discovered MBAs, R. Strauss et al. (2024) found three such objects, two (2022 KB_9 and internal designation Iogm1Zl) with rotation periods very similar to MG56 at $\approx$0.21 hr ($\approx$13 minutes). With derived H magnitudes of 19.0 and 20.3, respectively, these subkilometer MBA superfast rotators from the DEEP survey fall within the size–spin rate regime of our Rubin superfast rotator sample, also above the Strong Lunar Cohesion limit. Even with the differences between the expected cadence of Rubin Observatory's decade-long LSST currently scheduled to begin in early 2026 and the irregular, commissioning-driven cadence of the RFL dataset, Rubin is likely to further probe this subkilometer regime of superfast rotators, helping us to better understand just how rare these very rapid rotators are among the asteroid population.

Plotting the orbital elements of the Rubin superfast rotators in the context of known fast rotators (Figure 15) reveals that most of the former appear to integrate well with known patterns of potential families that likely share a common high angular momentum collision event in the past. Notable exceptions are 2025 MU_{15} and 2025 MM_{81}, which cluster closely in orbital element space near the Hungarias (see discussion in Section 4). Those two objects also share similar absolute magnitudes and colors, which may also indicate a common origin. To confirm potential family membership, however, proper element analysis is required (Z. Knežević & A. Milani 2003; D. Nesvorný et al. 2024), which is beyond the scope of this work. It is also interesting to note that $>$50% of the objects with $a < 2$ au (three out of five) and with $a > 3.4$ au (one out of two) for which we determine reliable rotation periods are found to be superfast rotators.

Of additional note is the fact that all but one object in our reported sample of 76 asteroids with reliable rotation periods ranging from 0.031 to 21.3 hr and H magnitudes from $\simeq$17.1 to $\simeq$22.7 are MBAs or "other" asteroids that sit just outside the

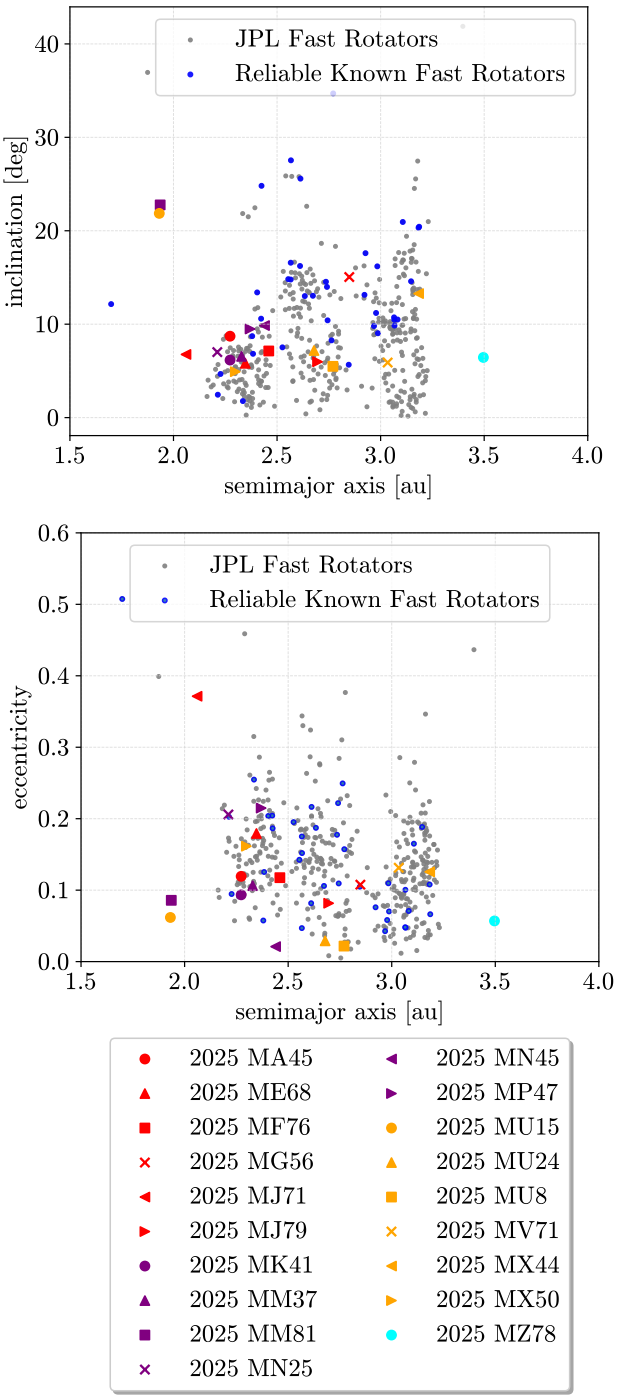

Figure 15. Semimajor axis, eccentricity, and inclination for the Rubin superfast rotators and known fast rotators (gray circles), where the "reliable known fast rotators" (blue circles) are defined as asteroids with a spin period uncertainty below 30% based on data from NASA JPL (2025). 2025 MU_{15} and 2025 MM_{81} cluster around $a \approx 1.9$ au, $e < 0.1$, and $i \approx 22°$. "Other"-classified asteroid 2025 MZ_{78} sits at $a > 3.4$ au. Amor NEO MJ71 has a higher eccentricity of $e \approx 0.37$.

outer edge of the traditionally defined main belt. Of the five $H < 20$ asteroids listed above with rotation periods <0.3 hr, the two objects with similar H magnitudes to MN45, MK41, MV71, and MG56 ($H \approx 17.5$–19.5) are NEOs, while the two MBAs are much larger (with $H \approx 15.5$–16.5). Amor NEO MJ71 joins this group of super- to ultrafast rotators at a smaller size ($H \approx 22.7$). As a result, this Amor and these four Rubin-discovered MBAs join these two NEAs as the fastest-spinning subkilometer asteroids known. In addition, as evident from Figure 14, Rubin is successfully probing the currently widely undersampled region of the size–spin rate regime for MBAs. Typically, only subkilometer NEOs have been reported with rotation periods less than the 2.2 hr spin barrier (P. Sánchez & D. J. Scheeres 2014; F. Monteiro et al. 2020; S. Hu et al. 2021), particularly for diameters down to a few hundred meters and periods <1 hr or even a few minutes. In this 76-object Rubin sample alone, we have 37 MBAs smaller than the smallest MBA visible in Figure 1 of S. Hu et al. (2021) and 8 MBAs with both smaller sizes and shorter rotation periods than those reported in their figure. With millions of MBA discoveries, each with hundreds of observations, expected from Rubin over the next decade (J. A. Kurlander et al. 2025), our understanding of asteroid physical structures and collisional histories is poised to be transformed.

4.1.2. Large Lightcurve Amplitudes and Elongated Shapes

As described in Section 3, the amplitude of a lightcurve can be used to estimate the rough shape of an asteroid, particularly for the axial ratio or elongation of the object. More elongated objects typically have larger changes in brightness as they rotate and thus tend to have larger-amplitude lightcurves, while more spherical objects have flatter lightcurves with less variation in their magnitudes over time. The shape and amplitude of a lightcurve also depend on the angle between the spin vector and the line of sight, as well as the phase angle, α (i.e., the Sun–object–observer angle). Generally the amplitude increases owing to scattering and self-shadowing effects for a given axis ratio, as the phase angle increases (V. Zappala et al. 1990; X.-P. Lu & D. Jewitt 2019).

To estimate the minimum axial elongation of the 76 objects in our sample in order to identify highly elongated objects, we follow the approach of V. Zappala et al. (1990), using the lightcurve amplitudes computed from our high-order Fourier analysis and accounting for the observed phase angles of each object;[46] all 76 objects in our sample were observed within a single Rubin field over a span of no more than 12 days, with phase angles that cover a relatively small range (≃10°–20°).[47]

First, we estimated the amplitude each asteroid should have at zero phase angle:

$$A(0) = A(\alpha)/(1 + m\alpha), \tag{11}$$

where α is the phase angle at which the asteroid is observed (here we take the average phase angle from the observations), $A(0)$ and $A(\alpha)$ are amplitudes for phase angles 0 and α, respectively, and m is a coefficient that depends on the spectral class of the asteroid. Here we considered an average value $m = 0.02$. The axial elongation was then calculated as $10^{0.4 \cdot A(0)}$.

Table 2 provides the lightcurve amplitudes and axial elongation estimates for each object in our Rubin sample. We find five objects for which both lightcurve modeling

[46] Additional methods are available, such as the analytical solution for a triaxial ellipsoid accounting for light scattering effects found in K. Muinonen & K. Lumme (2015); however, the geometrical approach of V. Zappala et al. (1990) suits the purposes of our estimations provided here.

[47] We note that this approach to determine minimum axial elongations provides rough estimates adequate to identify highly elongated objects. The limited phase-angle coverage restricts the shape and spin axis constraints possible with this dataset, and more measurements along the objects' orbits would be required to obtain precise shape models (A. Cellino et al. 2024; N. Takács et al. 2025).

methods calculate amplitudes >1 mag and seven objects for which at least one of the methods found an amplitude >1 mag. For the objects with discrepancies in the measured amplitudes, either they have quite sharp features in their lightcurves that are less well modeled in the extent of their magnitude variation by the fitting algorithms, or the period determination produced different results between the two methods, naturally leading to different amplitudes, as the data are phased differently.

Objects with amplitudes >1 mag have estimated minimum axial elongations $\geqslant$2 (i.e., axial ratios $\geqslant$2:1), with the largest estimated value at 3.1 for MK23. Of particular interest is MM81 ($H = 21.1$; shown in Figure 11), which is both a fast rotator and moderatly elongated object with a period of 1.1 hr (computed from both our LSM and high-order Fourier analyses) and an estimated minimum axial elongation of 2.1. The two large, superfast rotators discussed in Section 4.1.1, MV71 and MG56, have estimated minimum axial elongations of 1.6 and 1.7, respectively, based on their moderate lightcurve amplitudes. Our axial ratio estimates are consistent with the computed relationships between lightcurve amplitude and axis ratio with respect to phase angle for C- and S-type asteroids found in X.-P. Lu & D. Jewitt (2019).

In addition, we can approximate the major- and minor-axis lengths assuming an ellipsoidal shape. For a geometric albedo $p_V = 0.15$, we estimated each object's diameter, d, from its absolute magnitude in the i band according to Equation (6). Then, we computed the axes (a and b) of an ellipsoid with a given a/b ratio. The brightest viewing orientation of the object corresponds to the projected area of its broadside, πab, and the faintest orientation is when viewed edge-on with an area = πb^2. Thus, the average between the two viewing orientations should coincide with the area of a circle with diameter d: $\pi(ab + b^2)/2 = \pi d^2$. From this, we computed the a, b axis lengths for each object. For the ultrafast rotators, we estimate $a = 0.87$ km and $b = 0.66$ km for MN45 ($H = 18.42$), $a = 0.138$ km and $b = 0.109$ km for MJ71 ($H = 22.36$), and $a = 0.62$ km and $b = 0.51$ km for MK41 ($H = 19.02$). Likewise, for the two fastest superfast rotators, $a = 1.28$ km and $b = 0.82$ km for MV71 ($H = 17.83$), and $a = 0.99$ km and $b = 0.57$ km for MG56 ($H = 18.57$).

As evident in Figure 11, several of the observed lightcurves for the objects in our sample are asymmetrical or have sharp features. The asymmetrical lightcurves typically indicate an asymmetrical object shape and can sometimes require a higher-order fit ($k > 2$) in our Fourier analysis. For example, 2025 MX_{44} required $k = 3$ to obtain a reliable Fourier fit. As seen in the lightcurve, three maxima/minima were extracted in the lightcurve fit, which could indicate that the object has an asymmetrical triaxial shape.

Sharp features in the lightcurves, in particular, can be an indication for binarity, as can the existence of additional, typically longer rotation periods. Given that $\approx$15% of all asteroids are binaries (J. L. Margot et al. 2002; P. Pravec et al. 2016), it is almost certain that some of the 76 asteroids in our Rubin sample for which we determine reliable rotation periods are binaries. In particular, some of the examples shown in the bottom two rows of Figure 11 are good candidates for binarity; however, determining the binarity of these objects is beyond the scope of this work. Lightcurves and periodograms for all 76 objects in our Rubin sample are provided in Appendix B, and any additional possible periods found from our high-order Fourier analysis are provided in Table 3 in Appendix B.

4.2. Rubin Asteroid Colors

Asteroid colors at optical and near-IR wavelengths reflect their surface chemical composition and have many uses, such as improved definition of asteroid families (Ž. Ivezić et al. 2002b; A. Parker et al. 2008; V. Carruba et al. 2024). In addition, the asteroid colors in SDSS and Rubin systems are strongly correlated with their optical (geometric) albedo and enable asteroid size estimate accuracy in the range 21%–25%, only about a factor of 1.3–1.4 worse than IR-based estimates (V. Ivezić & Ž. Ivezić 2021). The asteroid a color (defined as $a = 0.89*(g - r) + 0.45*(r - i) - 0.57$), constructed as a principal color in the SDSS $r - i$ vs. $g - r$ color–color diagram; Ž. Ivezić et al. 2001) is particularly powerful for discriminating the S and C types of asteroid taxonomy. Similarly, M. Colazo et al. (2022) show that the a and $g - i$ colors are 94% correlated, making $g - i$ also effective for distinguishing between C and S types. The $i - z$ color adds the ability to recognize V-type objects; regretfully, the Rubin dataset analyzed here does not include any z-band measurements.

The two panels in Figure 16 show representative color–color diagrams constructed with the $g - r$, $r - i$, and $g - i$ colors (without accounting for presumably minor differences in photometric zero-points between the SDSS and Rubin photometric systems) computed from both methods described above. Small differences in the color derivations between the two lightcurve modeling and rotation period determination methods are visible (see Section 3.4). As evident in the figure and as expected given their higher prevalence, the sample studied here includes more C-type than S-type asteroids (for a comparison see, e.g., Figure 10 in V. Carruba et al. 2024).

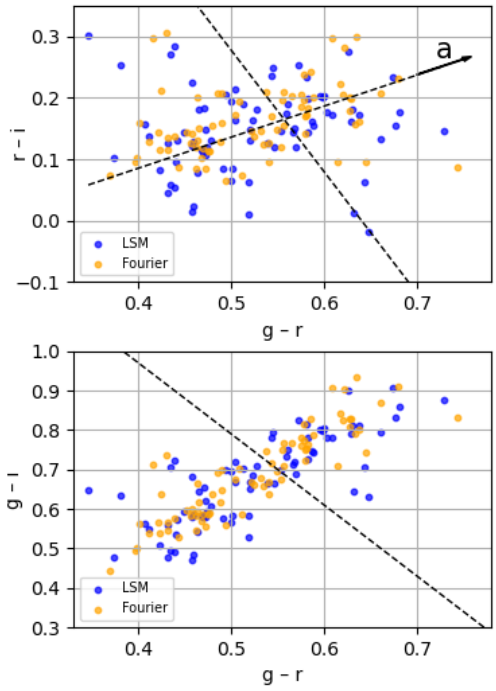

Figure 16. Color–color diagrams for these 76 objects. The blue points were computed using the LSM approach, while the orange points were determined using the high-order Fourier analysis (see Section 3 for details). The roughly vertical lines moving from the upper left to lower right of each plot provide a reference for the typical delineation between C- and S-type asteroids, with C-type asteroids generally falling to the left of the line and S-type asteroids falling on the right side. The a color is defined as $a = 0.89*(g - r) + 0.45*(r - i) - 0.57$ (Ž. Ivezić et al. 2001).

Tending to share similar chemical compositions, colors can be used to help identify asteroid family members and distinguish between overlapping families (Ž. Ivezić et al. 2002b; A. Parker et al. 2008; V. Carruba et al. 2024). While we determine colors, rotation periods, and fitted lightcurve amplitudes, which all have the potential to provide indications of an object's collisional history, age, and possible family membership, family member identification is beyond the scope of this work. In addition, our 76-object sample spread throughout the main belt is likely too small to confidently find members belonging to the same family. However, once Rubin commissioning is complete and the LSST begins producing vast numbers of discoveries with multiband photometry, such studies will likely lead to the identification of many new families across the asteroid belt.

5. Conclusions

We present lightcurves, rotation periods, and colors for the first asteroid discoveries made with the NSF-DOE Vera C. Rubin Observatory, finding 76 objects (75 MBAs and 1 NEO) with reliable rotation periods ranging from >21 hr to <2 minutes. The 19 superfast (<2.2 hr period) rotating asteroids identified are a demonstration of Rubin's ability to probe the region of subkilometer-sized rapid rotators in the main belt that is currently not well sampled. In addition, we surprisingly identified three ultrafast rotators with periods of <5 minutes composing ≃4% of our 76-object sample from the ∼2000-object RFL dataset. The unexpected prevalence of asteroids the size of several football field lengths ($d > 0.5$ km) that complete a full rotation in the extremely short period of <2 minutes requires us to refine our understanding of the formation and evolution of asteroid rotations. Determining the collisional history of these ultrafast rotators is beyond the scope of this work, but as more of these objects are discovered, they will likely transform, in part, our knowledge of asteroid collisions and the spin periods they can induce. Collisions may not be the only cause for these ultrafast rotation periods, and new methods of creating these rotations may additionally be required. As we get more data from Rubin's decade-long LSST currently scheduled to begin in early 2026, the sample size will increase tremendously, aiding efforts to explain the cause of these ultrafast rotations.

The RFL dataset in which these rotation periods were detected did not follow the expected cadence of Rubin's LSST but rather followed an irregular cadence driven by the requirements of commissioning. The dense temporal, multiband sampling of this RFL dataset made it ideal for determination of rotation periods, including detecting rapid rotation. Despite the differences from the commissioning cadence, Rubin's LSST will repeatedly image the entire southern sky every 3 days for a period of 10 yr, over time building up sufficient photometry of an expected 5 million small bodies across the solar system (the vast majority of which will be in the main asteroid belt) over the next decade (Ž. Ivezić et al. 2019; J. A. Kurlander et al. 2025) to enable much larger studies of asteroid rotation periods.

The RFL dataset samples the population of fast rotators across the main asteroid belt, with the largest semimajor axis in our 76-object reliable rotation period sample at $a \simeq 3.5$ au (Rubin-discovery 2025 MZ_{78} with mean r-band magnitude of 23.21). This sample provides a clear example of Rubin's ability, similarly expected with LSST, to provide rotation period determinations at fainter magnitudes, faster periods, and farther distances than are typically obtained by other surveys for MBAs. As the small-body population most studied regarding asteroid collisional histories, largely among the many asteroid families present, the main-belt population provides the best hunting ground for more of these ultrafast rotators and larger samples for rotation period studies overall. LSST is poised to provide us this dataset, expected to increase the number of known MBAs fourfold. With potentially unusual compositions, internal structures, and/or formation histories, a much larger sample of these extremely fast rotating asteroids is very likely to transform our understanding of asteroid physical structures and collisional histories and to a greater extent our understanding of the formation and evolution of the solar system.

Acknowledgments

We thank the referees for their thoughtful reviews of the Letter. We also thank the LSST Solar System Science Collaboration for manuscript feedback, especially Milagros Colazo, Andy Rivkin, and David Trilling for insightful comments that helped to improve the Letter. D.E.V. expresses his gratitude to his wife, Elizaveta Vavilova, whose suggestion to look for asteroids with minute-scale rotation periods made the discovery of ultrafast rotators possible.

This material is based on work supported in part by the National Science Foundation through Cooperative Agreements AST-1258333 and AST-2241526 and Cooperative Support Agreements AST-1202910 and AST-2211468 managed by the Association of Universities for Research in Astronomy (AURA) and the Department of Energy under contract No. DE-AC02-76SF00515 with the SLAC National Accelerator Laboratory managed by Stanford University. Additional Rubin Observatory funding comes from private donations, grants to universities, and in-kind support from LSST-DA Institutional Members.

We acknowledge the use of an LSST tutorial notebook developed by the Rubin Observatory Community Science Team for retrieving the Rubin observations from the Minor Planet Center that were used as the dataset for this study.

The work of S.G. is supported by NOIRLab, which is managed by the Association of Universities for Research in Astronomy (AURA) under a cooperative agreement with the US National Science Foundation.

This research is supported by the National Science Foundation under grant Nos. 2307569 and 2307570 and is partially funded by a generous gift of Charles Simonyi to the NSF Division of Astronomical Sciences. The award is made in recognition of significant contributions to Rubin Observatory's Legacy Survey of Space and Time. Any opinions, findings, and conclusions or recommendations expressed in this material are those of the author(s) and do not necessarily reflect the views of the National Science Foundation.

This work is supported by NASA Solar System Workings grant 80NSSC22K0978.

We acknowledge support from the DiRAC Institute in the Department of Astronomy at the University of Washington. The DiRAC Institute is supported through generous gifts from the Charles and Lisa Simonyi Fund for Arts and Sciences, Janet and Lloyd Frink, and the Washington Research Foundation.

The work of A.K. and J.M. is supported by the Asteroid Institute, a program of the B612 Foundation, through leadership

gifts from the W. K. Bowes Jr. Foundation, the McGregor Girand Charitable Endowment, the P. Rawls Family Fund, Tito's CHEERS, Alison and Steve Krausz, the Lyda Hill Foundation, Maryann and John Montrym, Google Cloud, and three anonymous donors.

V.C. is grateful to the Brazilian National Research Council (CNPq, grant 304168/2021-1) and the São Paulo Research Foundation (FAPESP, grant 2025/01469-0) for their financial support.

Facilities: Rubin:Simonyi.

Software: Rubin Observatory Tutorial Notebooks https://github.com/lsst/tutorial-notebooks, Minor Planet Center BigQuery replica https://mpcq.readthedocs.io/en/latest/bigquery_dataset.html, Minor Planet Center Postgres database https://www.minorplanetcenter.net/mpcops/documentation/replicated-tables-info-general/.

Author Contribution

S.G. came up with the initial research concept and use of the methodology and provided formal analysis, validation and visualization of the results, writing and editing of the manuscript, and supervision and project administration. Z.L., D.E.V., and S.E. provided formal analysis and validation, as well as visualization of the results, and contributed to writing and editing the manuscript. D.S. provided validation, as well as visualization of the results, and contributed to writing and editing the manuscript. M.J. came up with the initial research concept and use of the methodology, contributed the presented characterization of the Rubin First Look dataset, and contributed to writing and editing of the manuscript. Z.I. contributed knowledge of the methodology, provided formal analysis and validation of the results, and contributed to writing and editing of the manuscript. A.K. and J.M. provided the extraction of the Rubin First Look dataset from the MPC and contributed to writing and editing the manuscript. V.C., M. W., and M.G. provided comments that contributed to the writing and editing of the manuscript. All other authors are members of the Rubin Project and have contributed in numerous ways to the development of the Rubin Observatory and the observations that enabled this work.

Appendix A
Retrieval of the Rubin First Look Data Release from the Minor Planet Center

The identifications of new asteroid candidates in the RFL data were released via submission to the MPC as an ADES file. We obtain the measurements by querying a BigQuery replica[48] hosted by the Asteroid Discovery Analysis and Mapping (ADAM) platform (S. Greenstreet et al. 2021) of the MPC Postgres database[49] using the following:

```
SELECT
public_obs_sbn.id,
public_obs_sbn.trksub,
public_obs_sbn.trkid,
public_obs_sbn.obsid,
public_obs_sbn.submission_id,
public_obs_sbn.submission_block_id,
public_obs_sbn.obs80,
public_obs_sbn.status,
public_obs_sbn.ref,
public_obs_sbn.healpix,
public_obs_sbn.permid,
public_obs_sbn.provid,
public_obs_sbn.artsat,
public_obs_sbn.mode,
public_obs_sbn.stn,
public_obs_sbn.trx,
public_obs_sbn.rcv,
public_obs_sbn.sys,
public_obs_sbn.ctr,
public_obs_sbn.pos1,
public_obs_sbn.pos2,
public_obs_sbn.pos3,
public_obs_sbn.poscov11,
public_obs_sbn.poscov12,
public_obs_sbn.poscov13,
public_obs_sbn.poscov22,
public_obs_sbn.poscov23,
public_obs_sbn.poscov33,
public_obs_sbn.prog,
public_obs_sbn.obstime,
public_obs_sbn.ra,
public_obs_sbn.dec,
public_obs_sbn.rastar,
public_obs_sbn.decstar,
public_obs_sbn.obscenter,
public_obs_sbn.deltara,
public_obs_sbn.deltadec,
public_obs_sbn.dist,
public_obs_sbn.pa,
public_obs_sbn.rmsra,
public_obs_sbn.rmsdec,
public_obs_sbn.rmsdist,
public_obs_sbn.rmspa,
public_obs_sbn.rmscorr,
public_obs_sbn.delay,
public_obs_sbn.rmsdelay,
public_obs_sbn.Doppler,
public_obs_sbn.rmsdoppler,
public_obs_sbn.astcat,
public_obs_sbn.mag,
public_obs_sbn.rmsmag,
public_obs_sbn.band,
public_obs_sbn.photcat,
public_obs_sbn.photap,
public_obs_sbn.nucmag,
public_obs_sbn.logsnr,
public_obs_sbn.seeing,
public_obs_sbn.exp,
public_obs_sbn.rmsfit,
public_obs_sbn.com,
public_obs_sbn.frq,
public_obs_sbn.disc,
public_obs_sbn.subfrm,
public_obs_sbn.subfmt,
public_obs_sbn.prectime,
public_obs_sbn.precra,
public_obs_sbn.precdec,
public_obs_sbn.unctime,
public_obs_sbn.notes,
public_obs_sbn.remarks,
public_obs_sbn.deprecated,
public_obs_sbn.localuse,
public_obs_sbn.nstars,
```

[48] https://mpcq.readthedocs.io/en/latest/bigquery_dataset.html

[49] https://www.minorplanetcenter.net/mpcops/documentation/replicated-tables-info-general/

(Continued)

```
public_obs_sbn.prev_desig,
public_obs_sbn.prev_ref,
public_obs_sbn.rmstime,
public_obs_sbn.created_at,
public_obs_sbn.updated_at,
public_obs_sbn.trkmpc,
public_obs_sbn.orbit_id,
public_obs_sbn.designation_asterisk,
public_obs_sbn.all_pub_ref,
public_obs_sbn.shapeocc,
public_obs_sbn.obssubid,
public_obs_sbn.replacesobsid,
public_obs_sbn.group_id,
public_obs_sbn.vel1,
public_obs_sbn.fltr,
public_obs_sbn.vel3,
public_obs_sbn.vel2,
public_obs_sbn.obstime_text
FROM
‘moeyens-thor-dev‘.‘mpc_sbn_aurora‘.‘public_obs_sbn‘ AS public_obs_sbn
WHERE
public_obs_sbn.stn = ’X05’;
```

Appendix B
Full Set of Asteroid Lightcurves and Additional Possible Rotation Periods

Here we provide the fitted lightcurves and periodograms from our high-order Fourier and LSM analyses for all 76 objects in our sample in Figures 17–32. In addition, we publish additional possible rotational periods of asteroids computed from our high-order Fourier analysis (Table 3). These are the rotation periods that also present an acceptable fit to the data (p-value with the chosen solution $<95\%$ from the F-test). We also include here the asteroids for which the uncertainties in their rotation periods are not negligible and exceed 30%. In many cases, the additional spin periods correspond to aliases of the chosen (best-fit) solution. While these asteroids have multiple possible rotation periods, the uncertainty for each is low enough and the fit sufficient for us to consider it reliable, with additional possible solutions that we provide here. In addition, we find our computed absolute magnitude offsets used to derive colors and the lightcurve amplitudes used to estimate the minimum axial elongations to be stable among the possible rotation period solutions from the lightcurve modeling, and thus we include them in our sample.

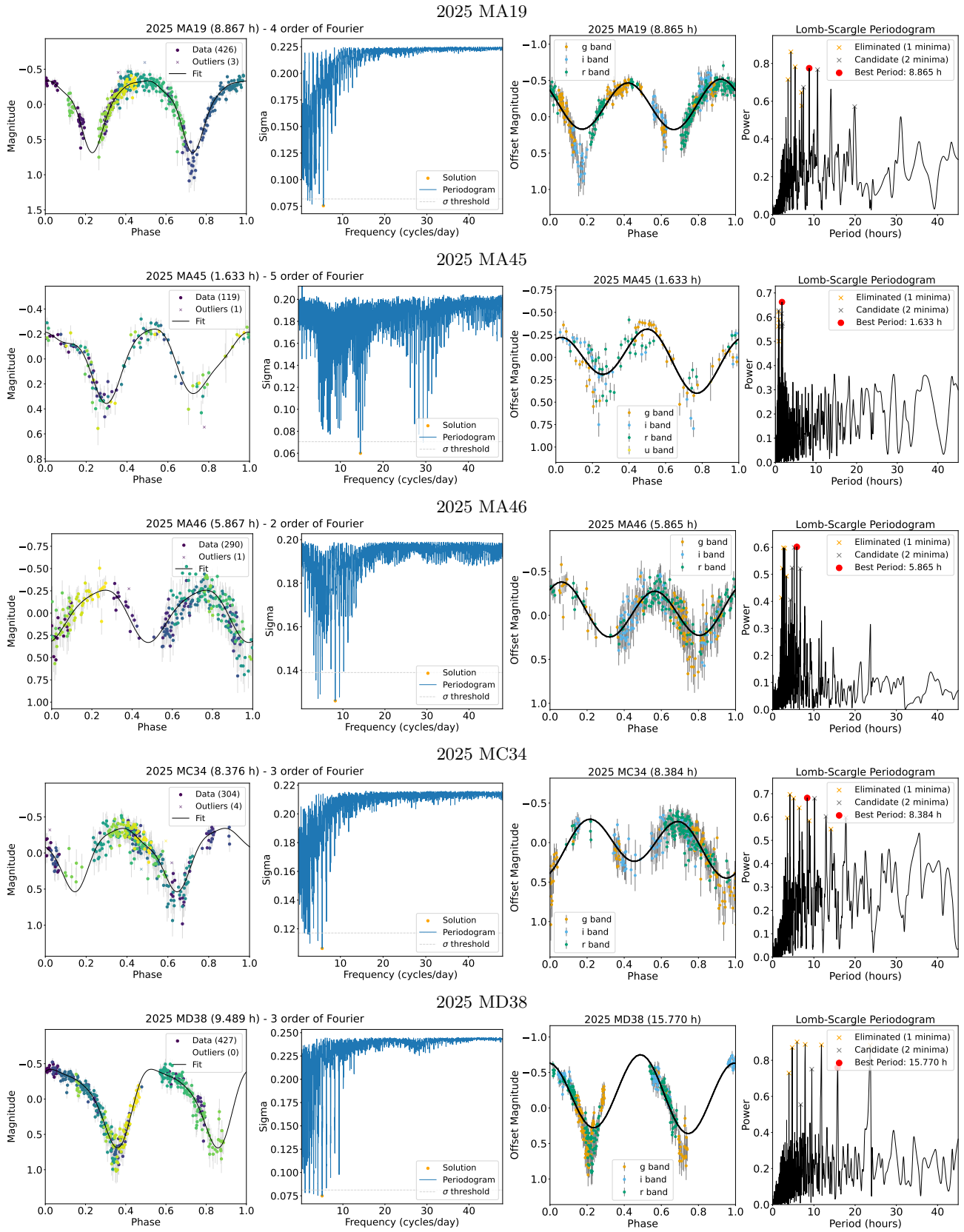

Figure 17. Fitted lightcurves and periodograms from the high-order Fourier (left) and LSM (right) methods for five selected objects in our 76-object sample.

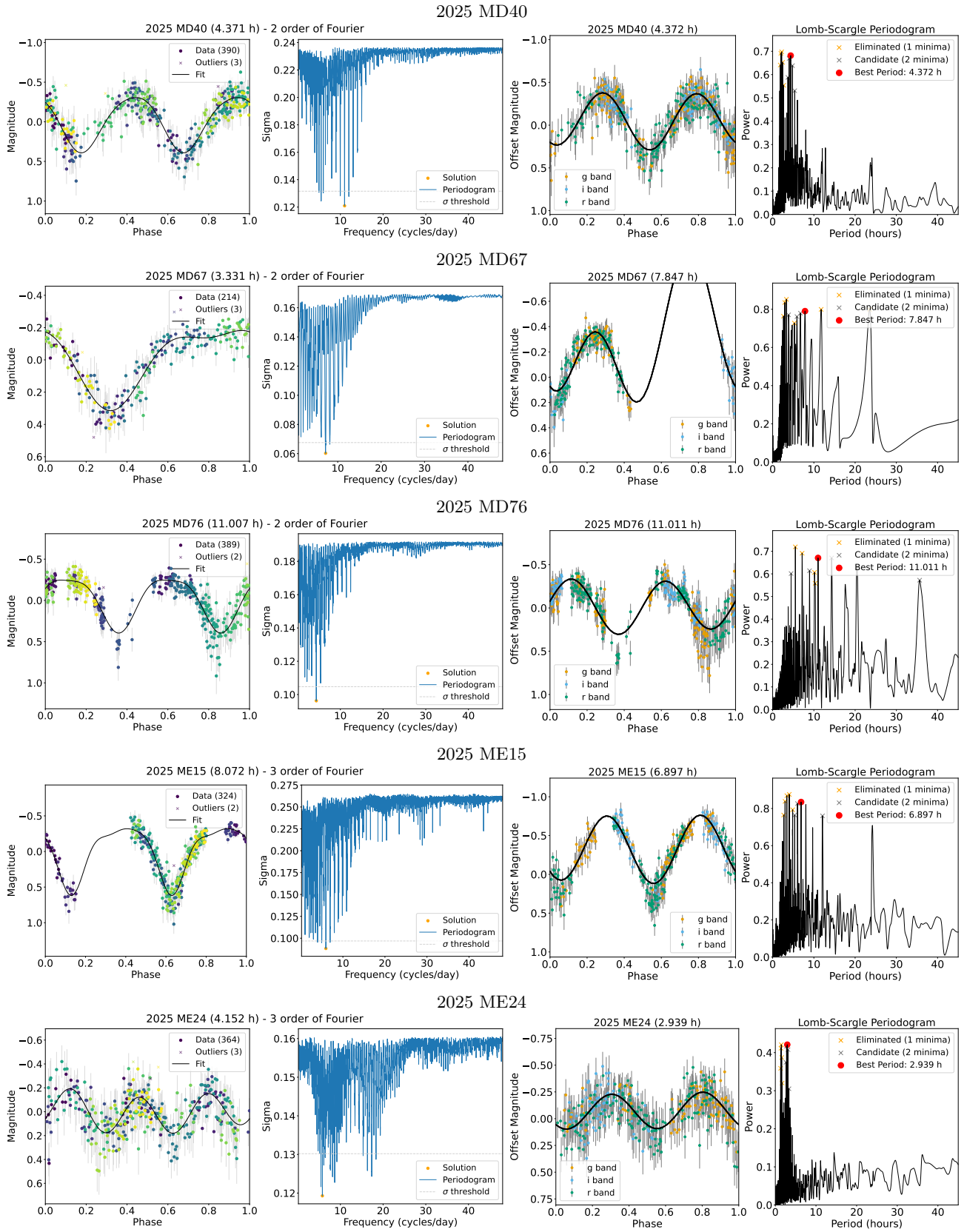

Figure 18. Fitted lightcurves and periodograms from the high-order Fourier (left) and LSM (right) methods for five selected objects in our 76-object sample.

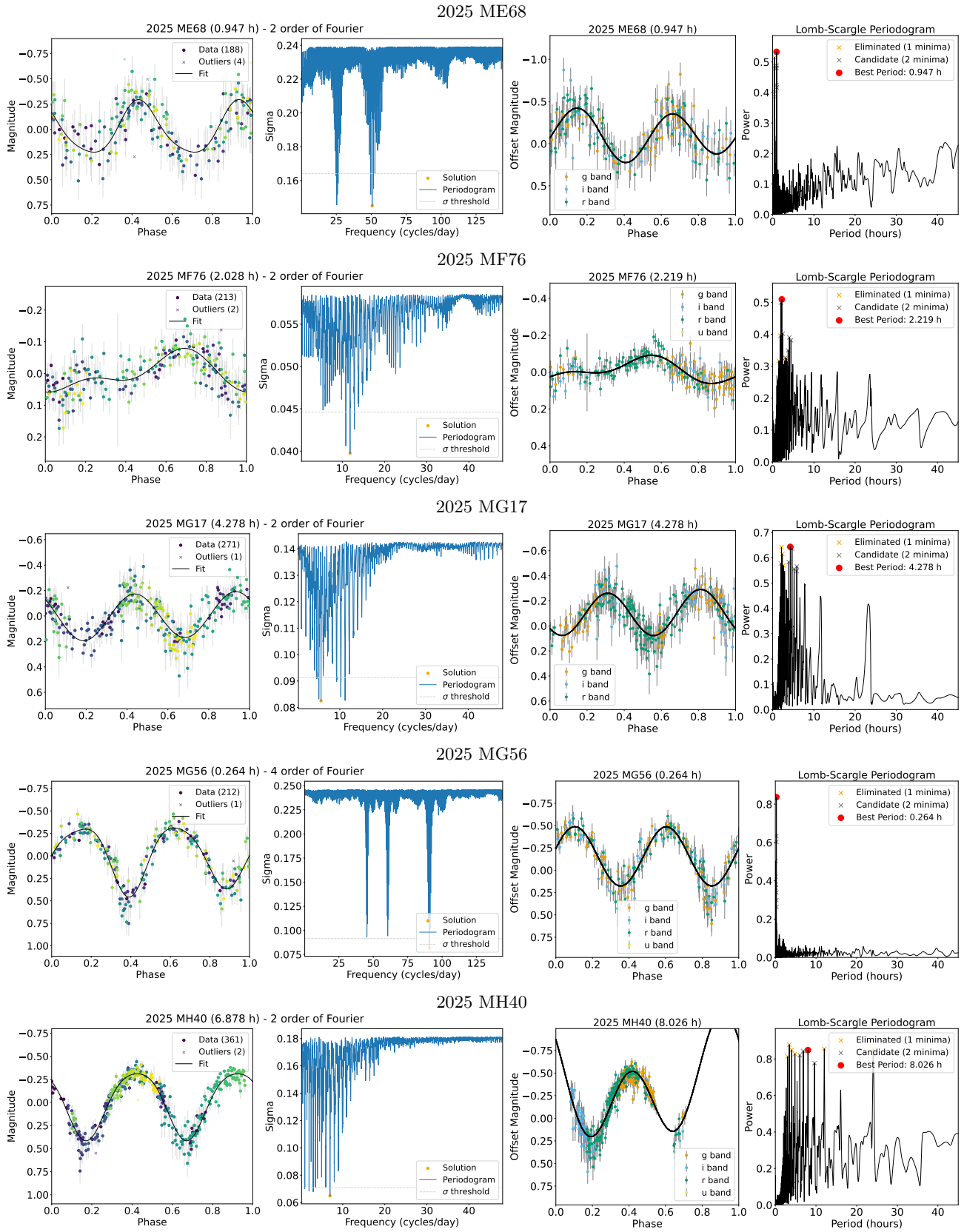

Figure 19. Fitted lightcurves and periodograms from the high-order Fourier (left) and LSM (right) methods for five selected objects in our 76-object sample.

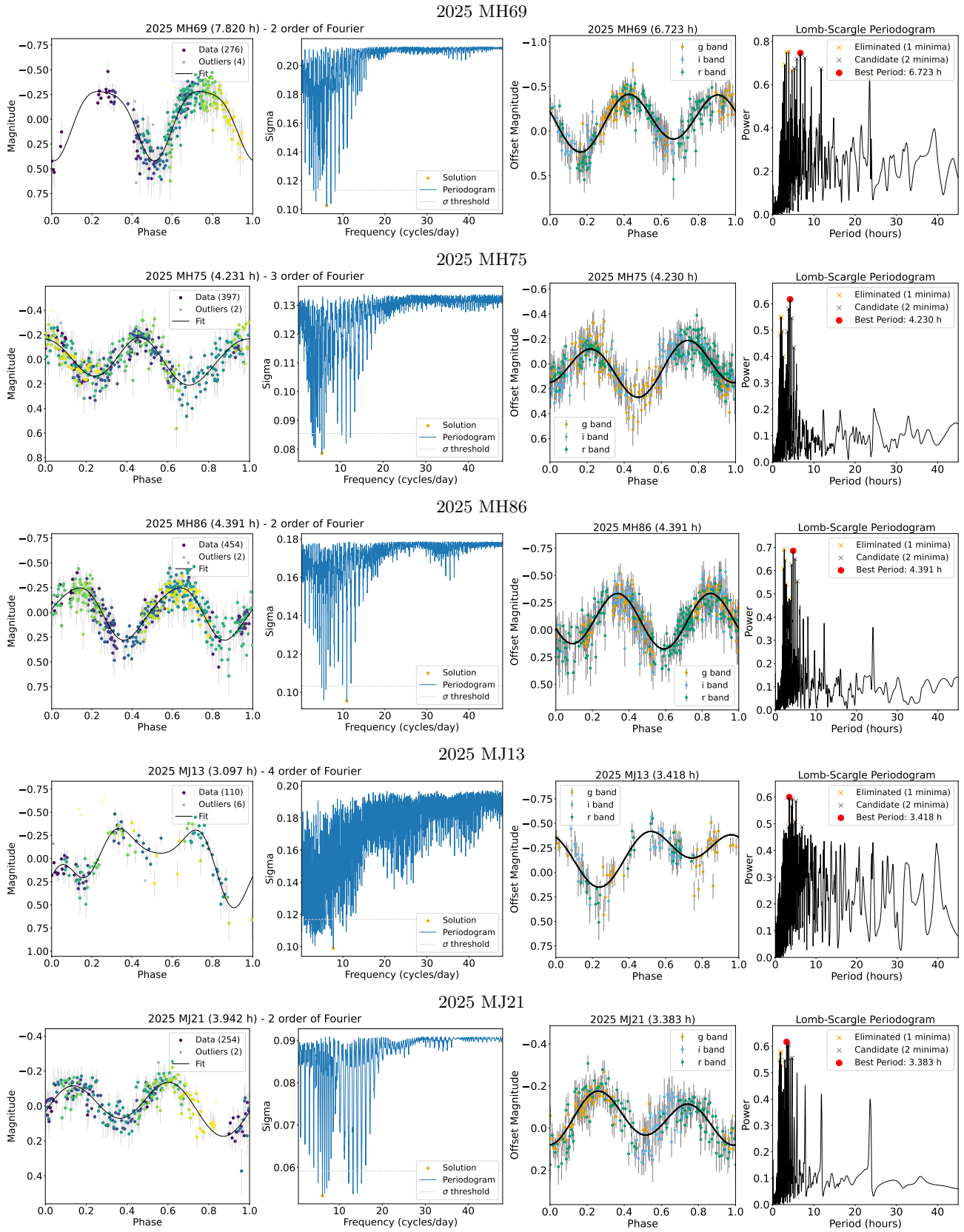

Figure 20. Fitted lightcurves and periodograms from the high-order Fourier (left) and LSM (right) methods for five selected objects in our 76-object sample.

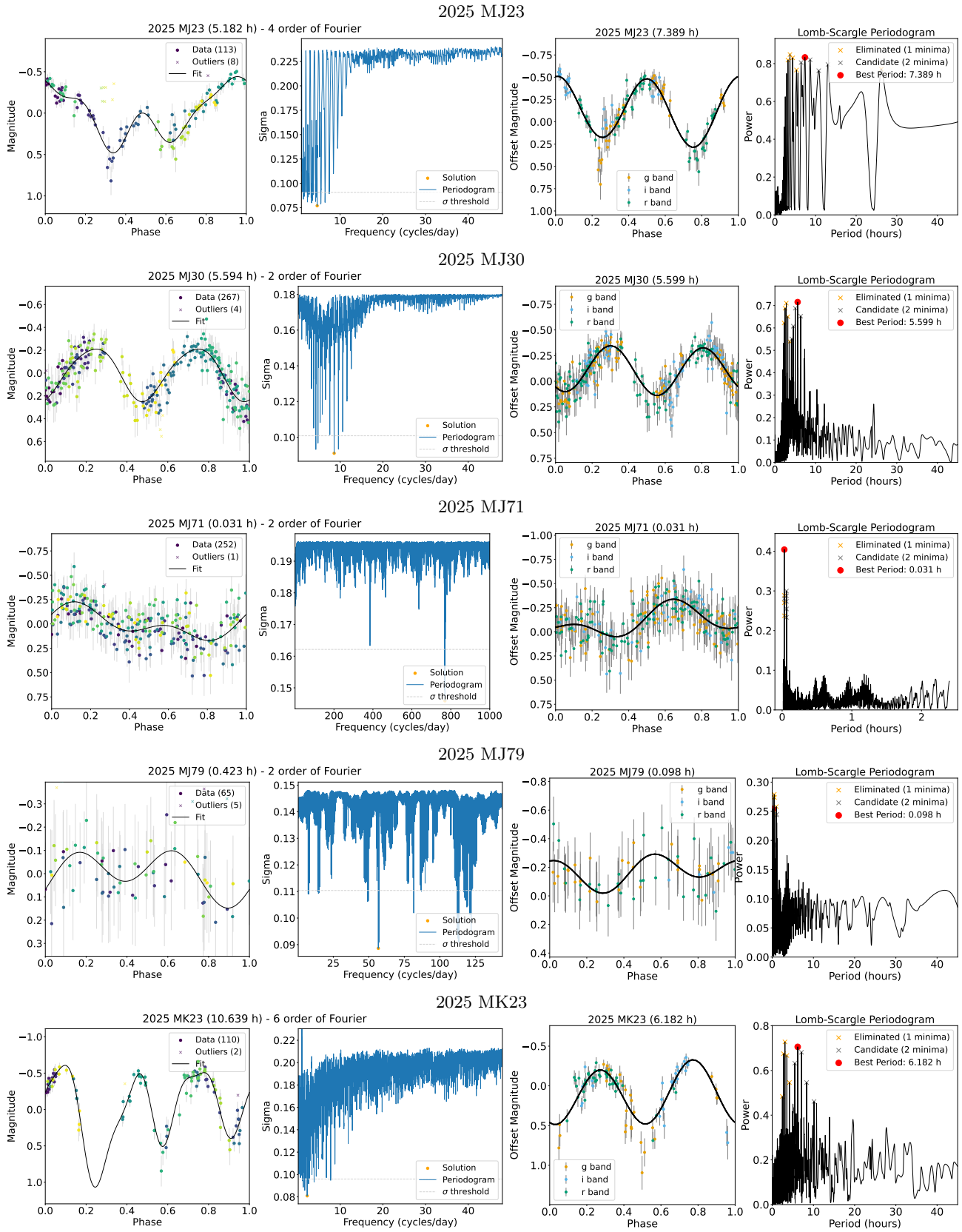

Figure 21. Fitted lightcurves and periodograms from the high-order Fourier (left) and LSM (right) methods for five selected objects in our 76-object sample.

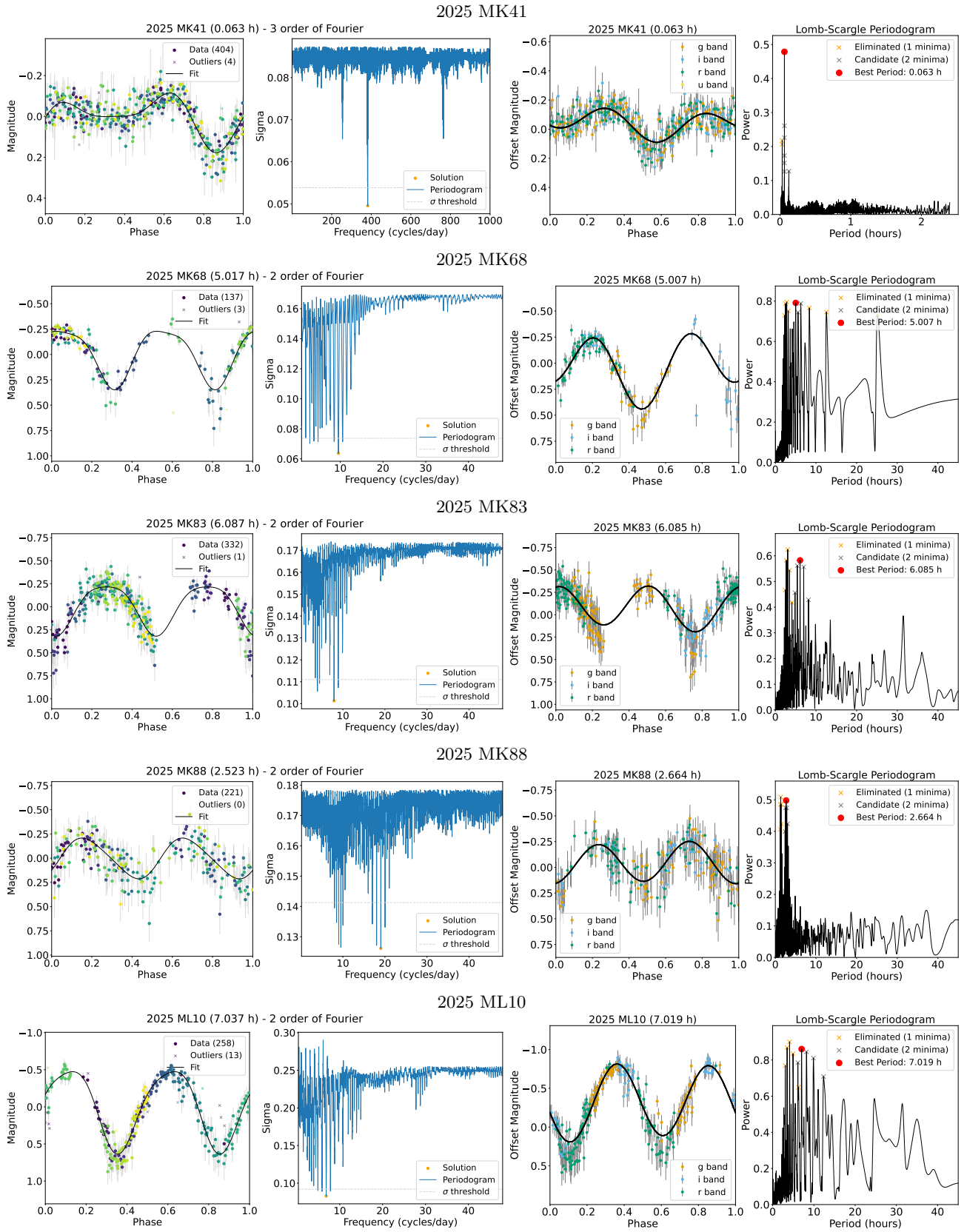

Figure 22. Fitted lightcurves and periodograms from the high-order Fourier (left) and LSM (right) methods for five selected objects in our 76-object sample.

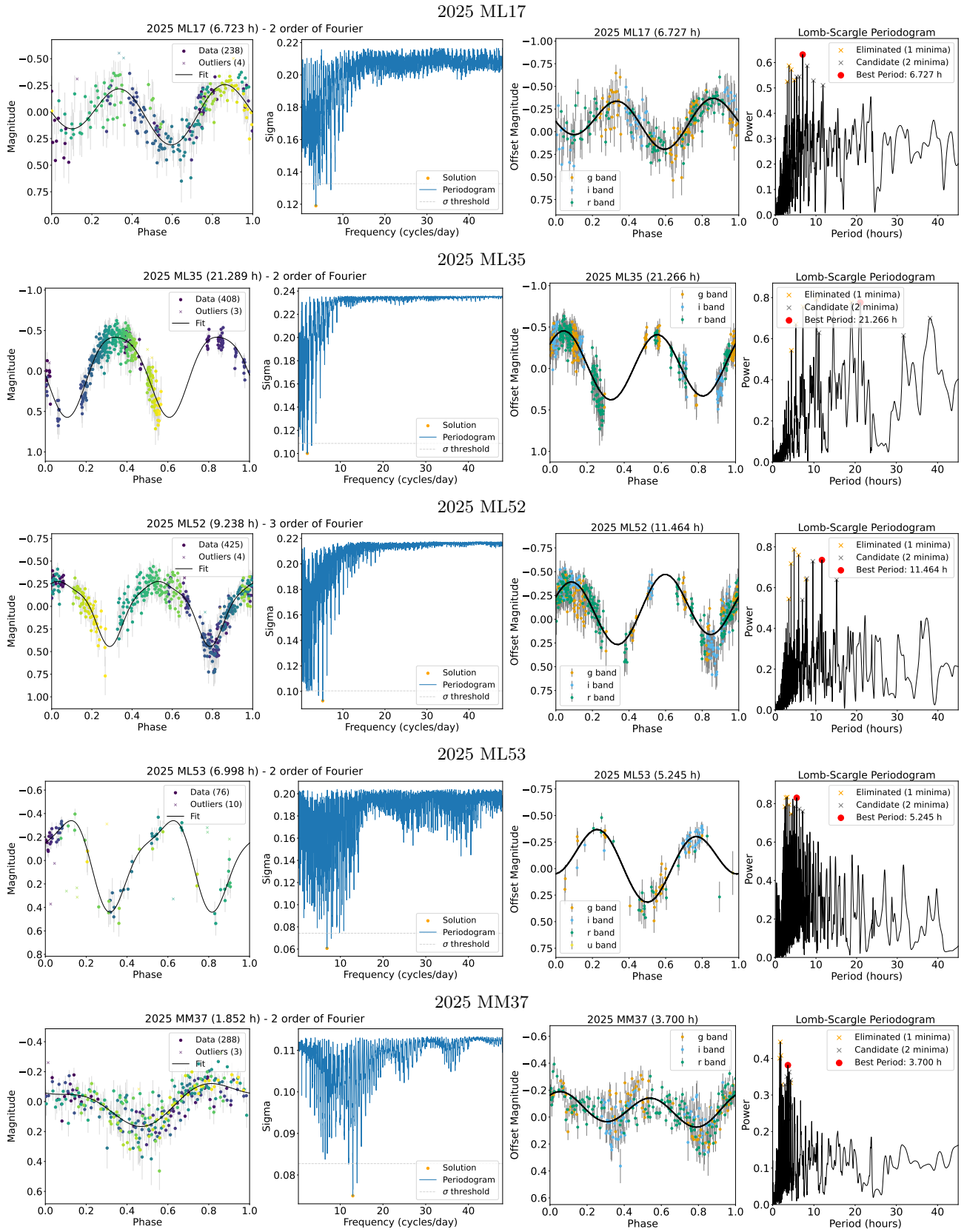

Figure 23. Fitted lightcurves and periodograms from the high-order Fourier (left) and LSM (right) methods for five selected objects in our 76-object sample.

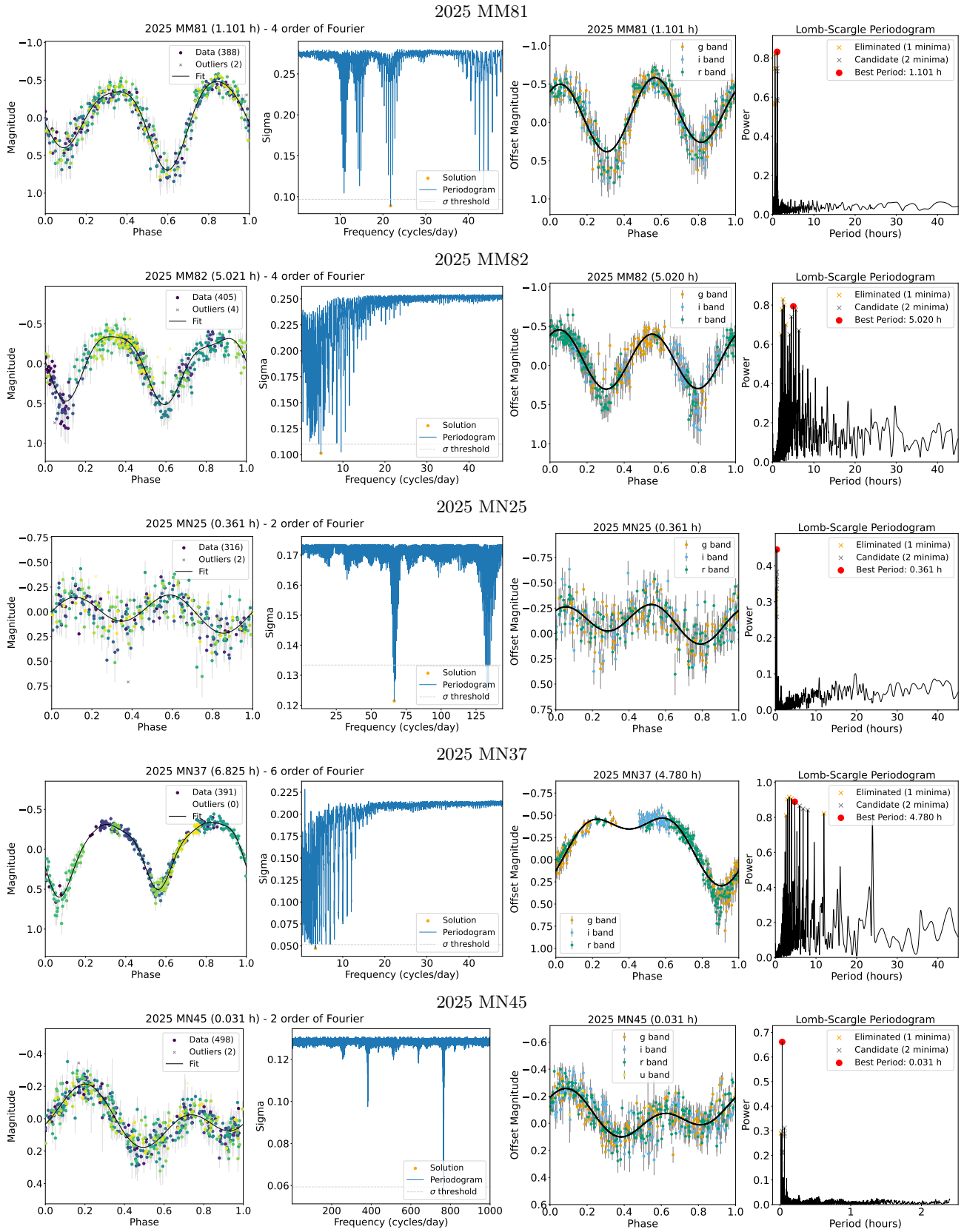

Figure 24. Fitted lightcurves and periodograms from the high-order Fourier (left) and LSM (right) methods for five selected objects in our 76-object sample.

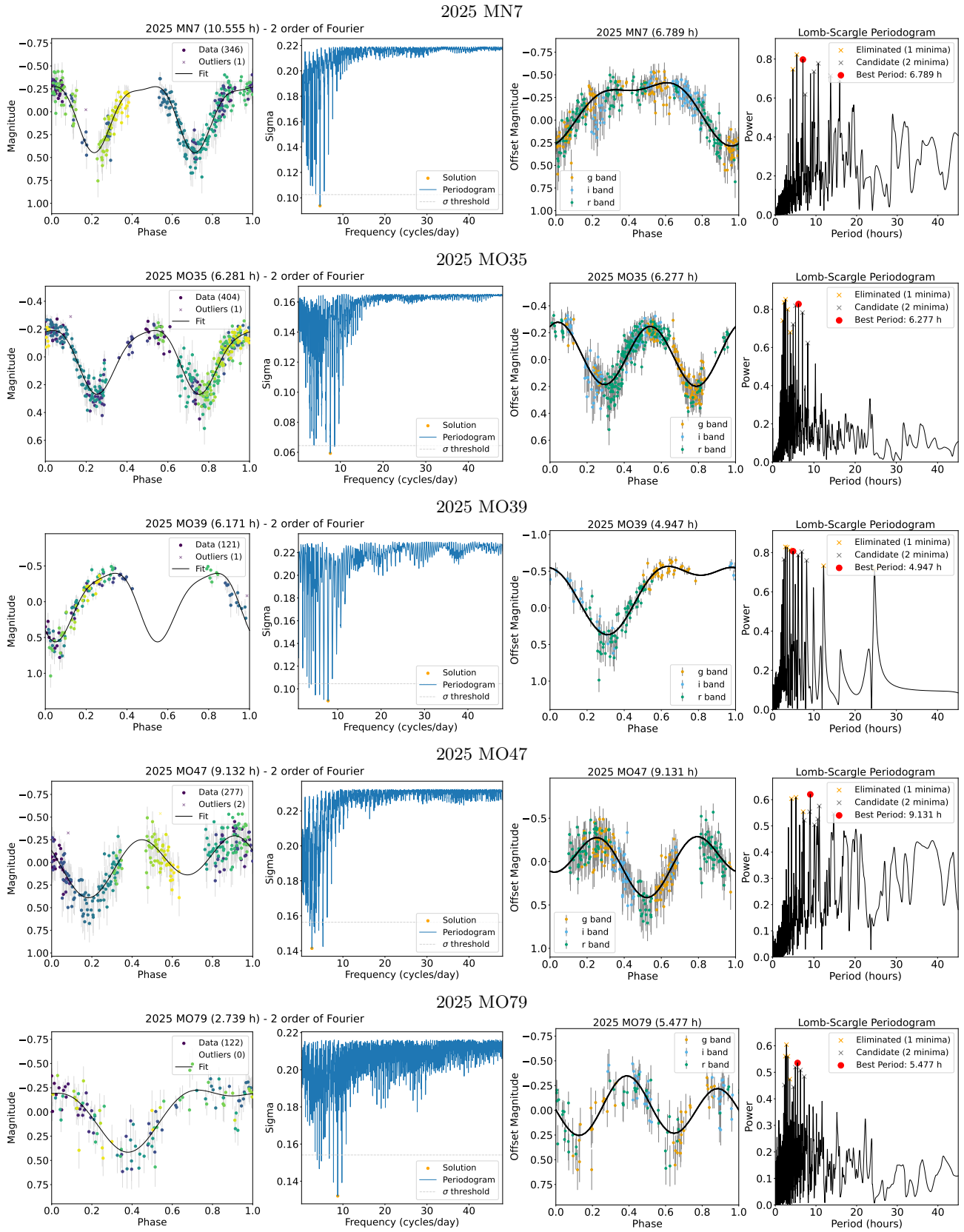

Figure 25. Fitted lightcurves and periodograms from the high-order Fourier (left) and LSM (right) methods for five selected objects in our 76-object sample.

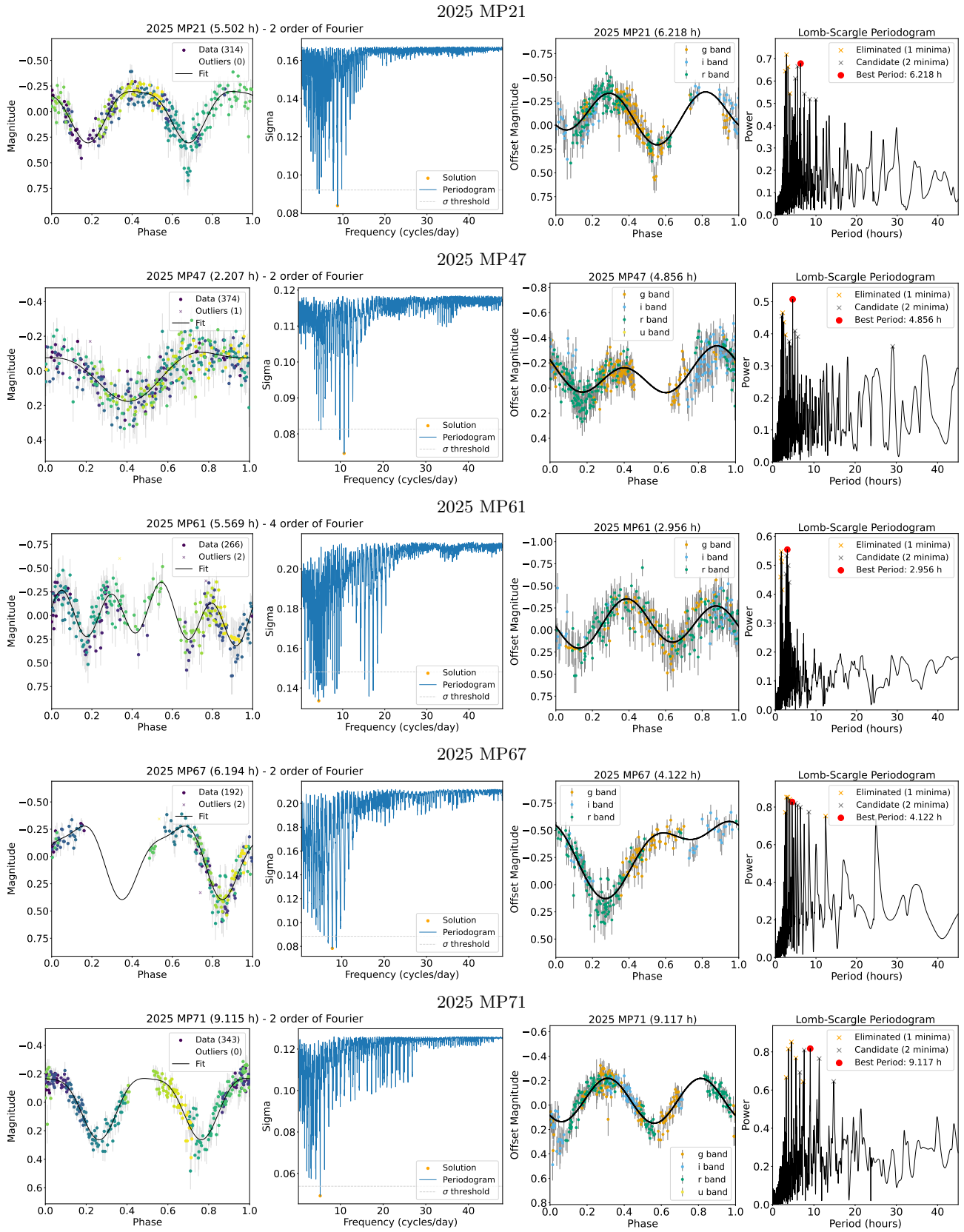

Figure 26. Fitted lightcurves and periodograms from the high-order Fourier (left) and LSM (right) methods for five selected objects in our 76-object sample.

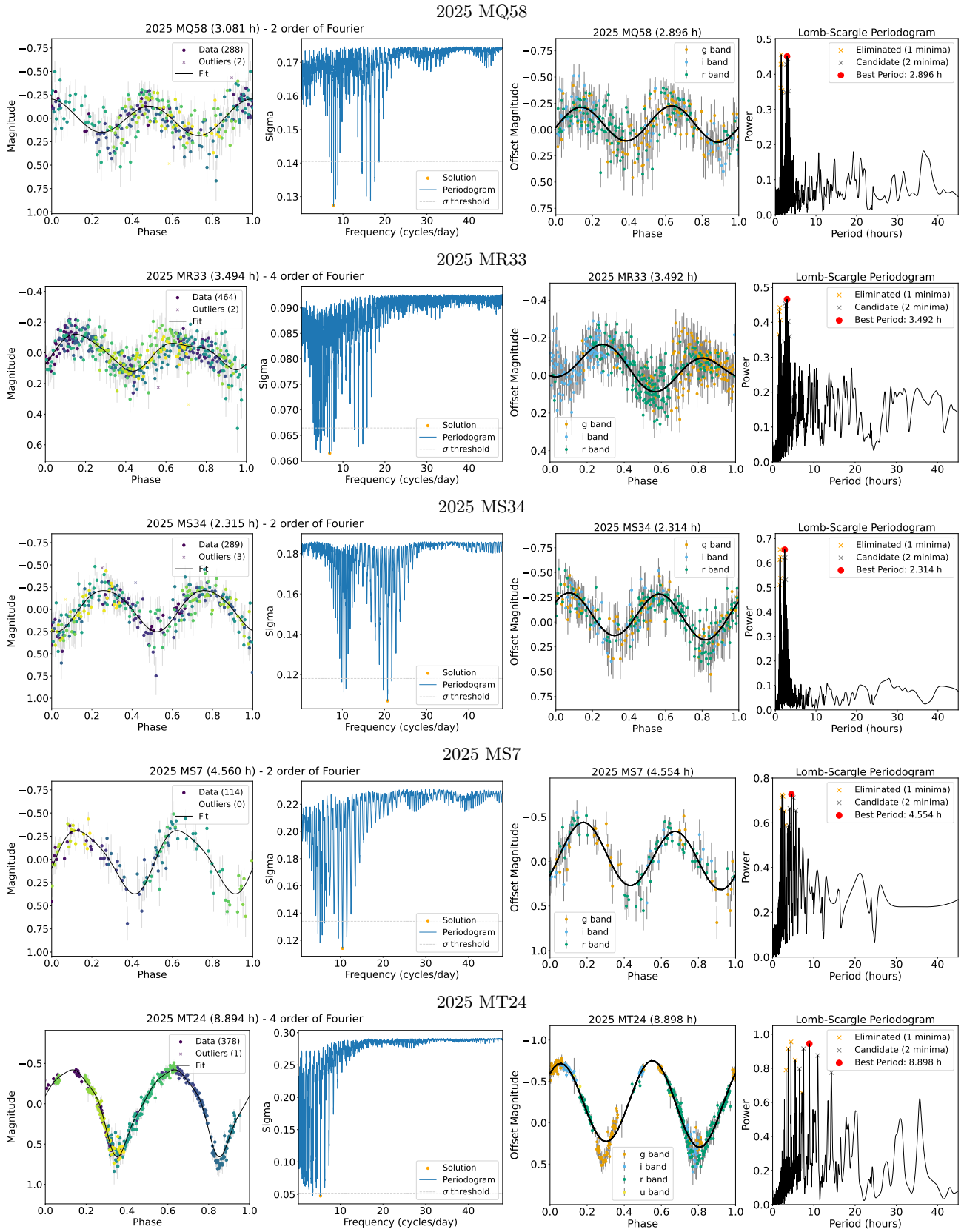

Figure 27. Fitted lightcurves and periodograms from the high-order Fourier (left) and LSM (right) methods for five selected objects in our 76-object sample.

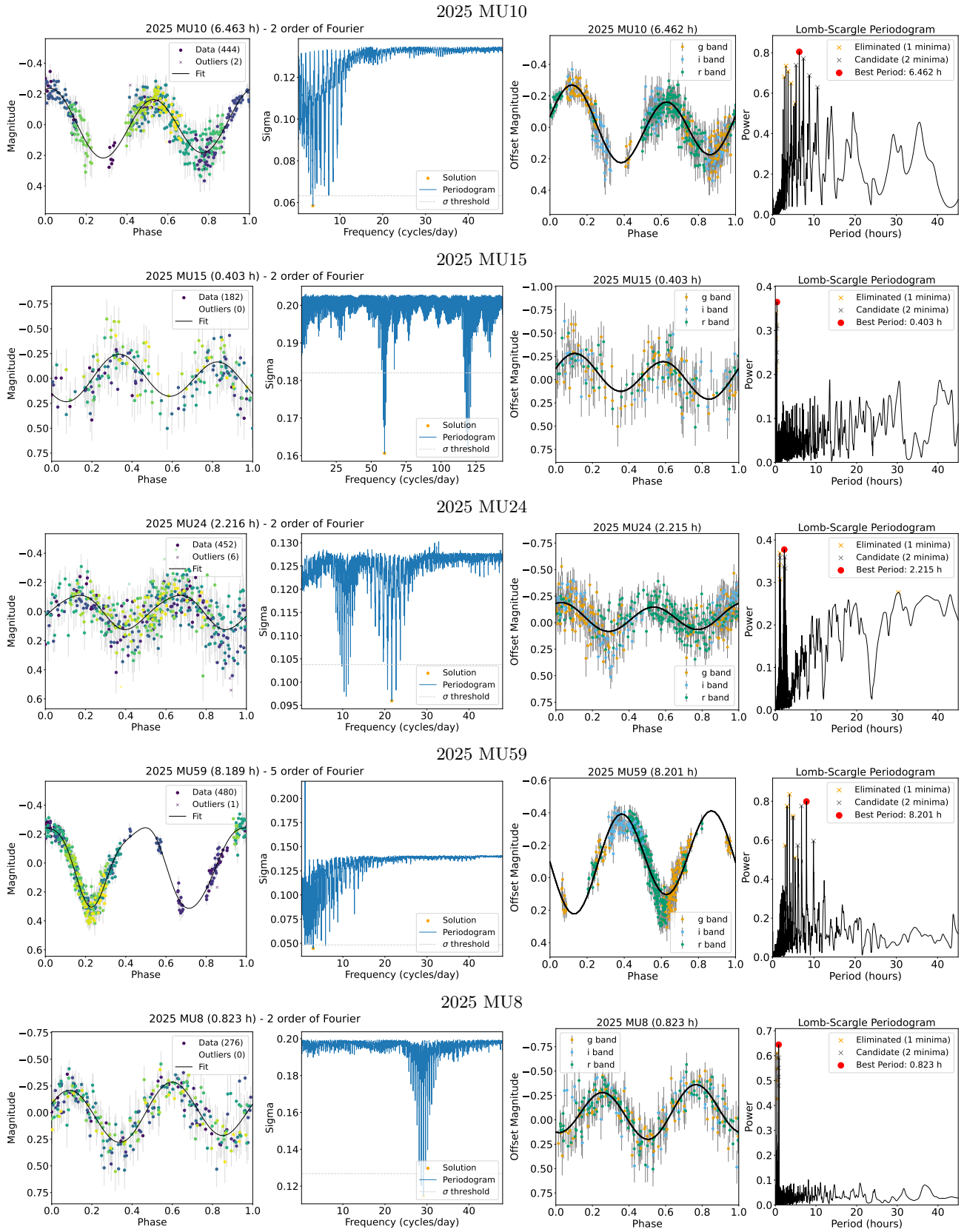

Figure 28. Fitted lightcurves and periodograms from the high-order Fourier (left) and LSM (right) methods for five selected objects in our 76-object sample.

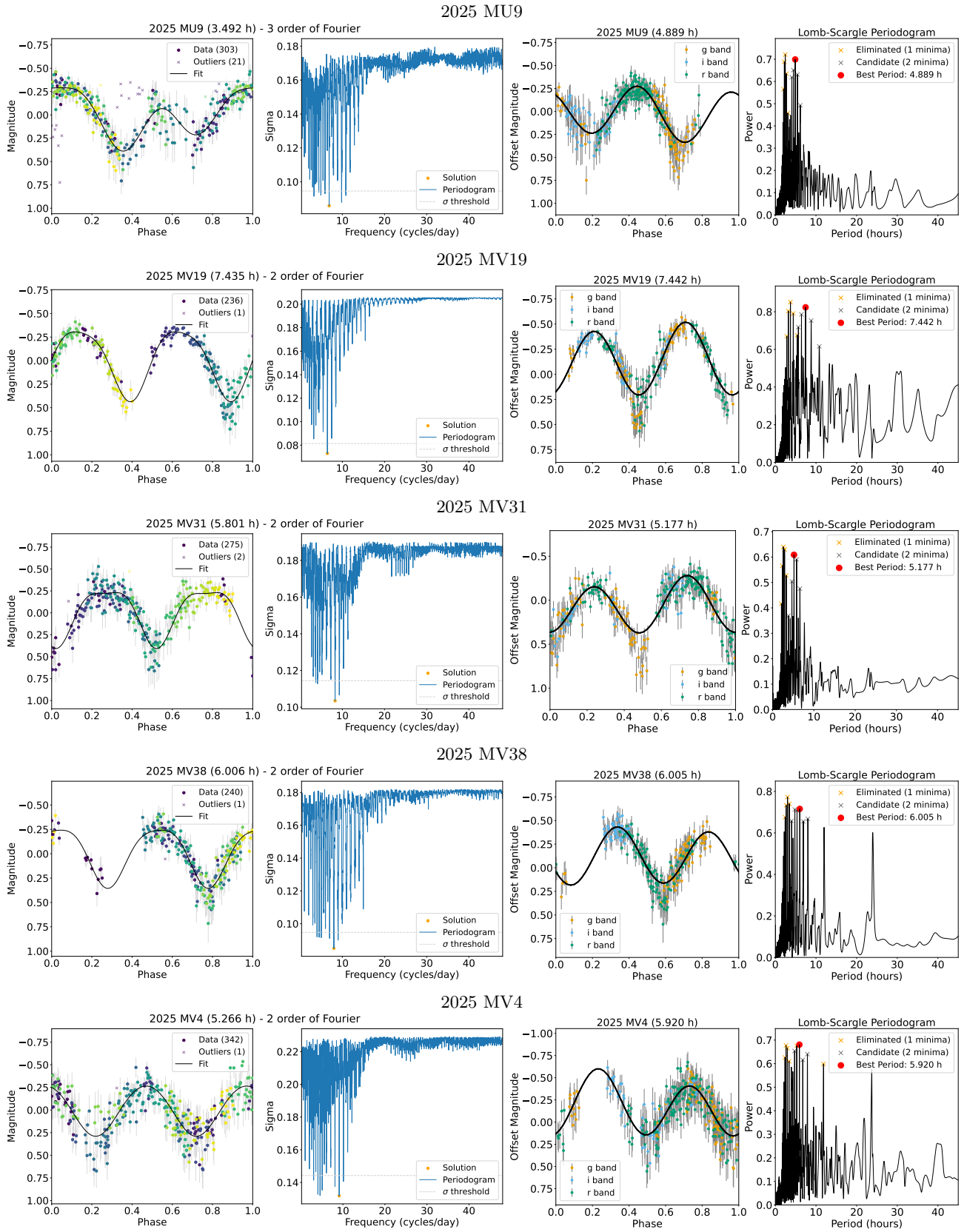

Figure 29. Fitted lightcurves and periodograms from the high-order Fourier (left) and LSM (right) methods for five selected objects in our 76-object sample.

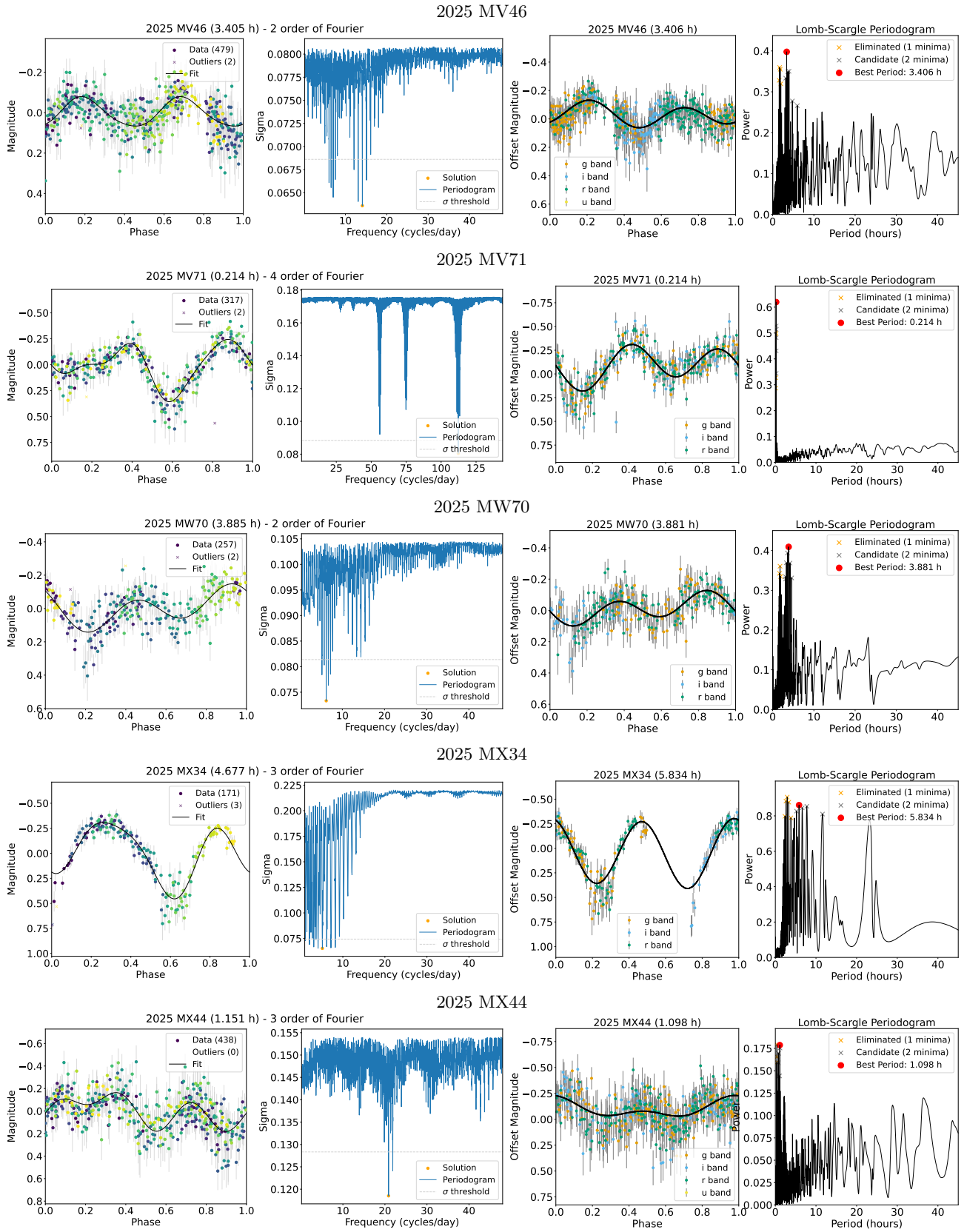

Figure 30. Fitted lightcurves and periodograms from the high-order Fourier (left) and LSM (right) methods for five selected objects in our 76-object sample.

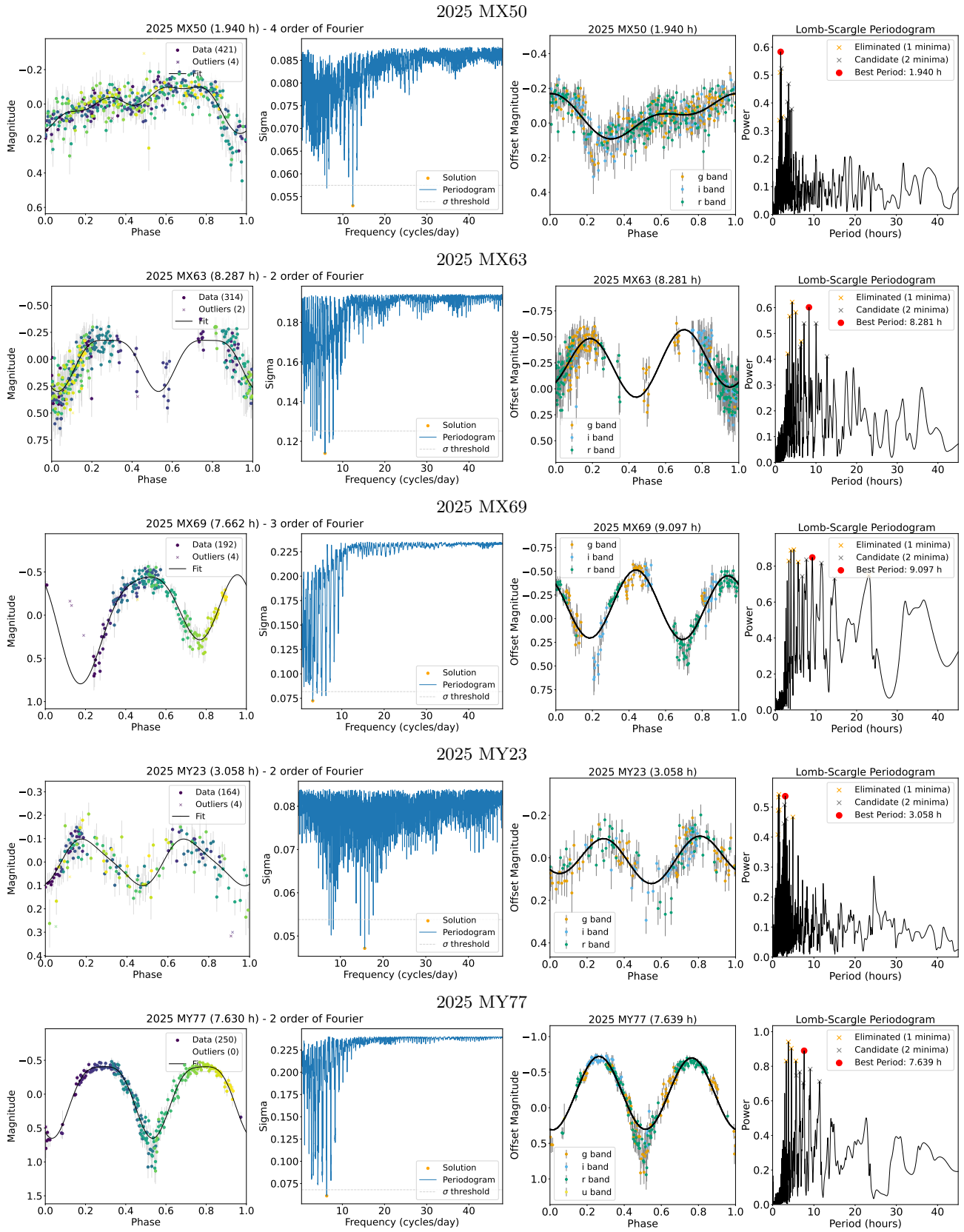

Figure 31. Fitted lightcurves and periodograms from the high-order Fourier (left) and LSM (right) methods for five selected objects in our 76-object sample.

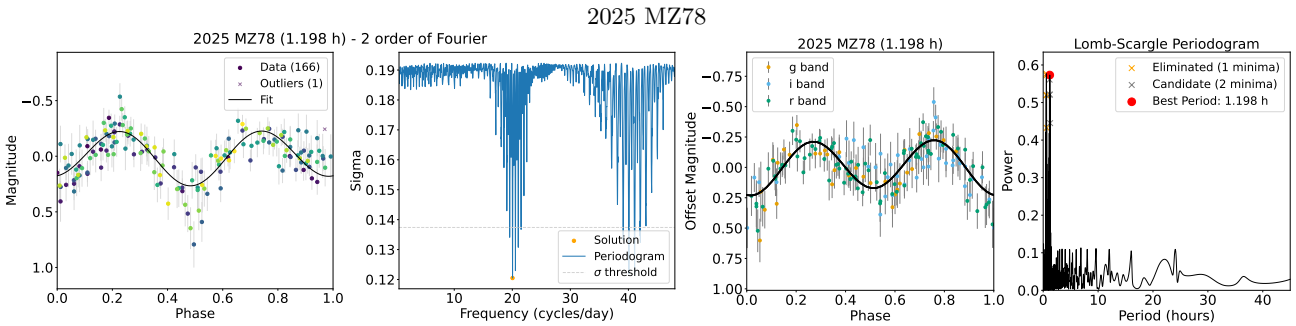

Figure 32. Fitted lightcurves and periodograms from the high-order Fourier (left) and LSM (right) methods for one selected object in our 76-object sample.

Table 3
Best-fit and Additional Rotation Periods for Asteroids in our Rubin Sample Computed from Our High-Order Fourier Analysis; Included are Asteroids for which the Uncertanties in Their Periods Exceeds 30%

Designation	Period	Additional Periods
2025 MA_{19}	$8.867^{+0.006}_{-0.012}$	10.913, 14.201
2025 MA_{45}	$1.633^{+0.000}_{-0.001}$	0.817
2025 MA_{46}	$5.867^{+0.008}_{-0.014}$	5.225, 6.685
2025 MC_{34}	$8.376^{+0.008}_{-0.012}$	5.075, 9.188, 10.144, 15.216
2025 MD_{38}	$9.489^{+0.010}_{-0.010}$	7.906, 11.856, 23.696, 47.392
2025 MD_{40}	$4.371^{+0.007}_{-0.003}$	4.006, 4.811
2025 MD_{67}	$3.331^{+0.027}_{-0.007}$	3.311, 5.879
2025 ME_{15}	$8.072^{+0.008}_{-0.015}$	4.849, 6.041, 6.902
2025 ME_{24}	$4.152^{+0.256}_{-1.537}$	
2025 MF_{76}	$2.028^{+0.005}_{-0.005}$	1.865, 1.869, 2.217
2025 MG_{17}	$4.278^{+0.907}_{-0.002}$	
2025 MH_{40}	$6.878^{+0.011}_{-0.007}$	8.023, 12.028, 48.200
2025 MH_{69}	$7.820^{+0.011}_{-1.919}$	
2025 MH_{75}	$4.231^{+2.740}_{-0.349}$	
2025 MH_{86}	$4.391^{+0.007}_{-0.004}$	4.019, 4.835
2025 MJ_{13}	$3.097^{+89.393}_{-1.118}$	
2025 MJ_{21}	$3.942^{+0.795}_{-0.784}$	
2025 MJ_{23}	$5.182^{+12.158}_{-1.966}$	
2025 MJ_{30}	$5.594^{+0.013}_{-0.005}$	5.009
2025 MJ_{79}	$0.423^{+2.986}_{-0.227}$	
2025 MK_{23}	$10.639^{+0.013}_{-0.013}$	3.090, 6.180, 9.273, 14.191, 17.732, 20.793
2025 MK_{68}	$5.017^{+0.023}_{-0.030}$	4.548, 5.576, 5.604, 6.266, 8.357
2025 MK_{83}	$6.087^{+0.009}_{-0.013}$	5.391, 5.398
2025 MK_{88}	$2.523^{+0.474}_{-0.126}$	
2025 ML_{10}	$7.037^{+0.000}_{-0.017}$	4.918, 6.151, 8.196
2025 ML_{17}	$6.723^{+0.016}_{-0.010}$	5.253, 5.896, 7.827, 7.841
2025 ML_{35}	$21.289^{+0.079}_{-0.156}$	14.711, 21.662, 38.255, 38.424
2025 ML_{52}	$9.238^{+0.010}_{-0.025}$	11.439, 13.842, 17.159
2025 ML_{53}	$6.998^{+0.003}_{-0.011}$	6.104
2025 MM_{37}	$1.852^{+0.002}_{-0.005}$	1.720, 1.724, 2.006
2025 MM_{82}	$5.021^{+0.003}_{-0.003}$	5.609
2025 MN_{37}	$6.825^{+0.007}_{-0.007}$	9.034
2025 MO_{35}	$6.281^{+0.011}_{-0.011}$	5.551
2025 MO_{39}	$6.171^{+0.023}_{-0.023}$	4.952, 7.056, 7.067, 8.229
2025 MO_{47}	$9.132^{+2.211}_{-1.970}$	
2025 MO_{79}	$2.739^{+0.004}_{-0.006}$	3.094, 3.555, 4.912, 4.915, 5.481, 6.184
2025 MP_{21}	$5.502^{+0.009}_{-0.007}$	6.220
2025 MP_{47}	$2.207^{+0.003}_{-0.005}$	4.036, 4.409, 4.858, 4.861, 4.868
2025 MP_{61}	$5.569^{+41.736}_{-4.177}$	
2025 MP_{67}	$6.194^{+0.019}_{-0.026}$	3.540, 5.499, 5.520
2025 MQ_{58}	$3.081^{+0.215}_{-0.499}$	
2025 MR_{33}	$3.494^{+4.050}_{-1.747}$	
2025 MS_{34}	$2.315^{+0.004}_{-0.004}$	2.209, 2.432

Table 3
(Continued)

Designation	Period	Additional Periods
2025 MS_{7}	$4.560^{+0.025}_{-0.025}$	3.832, 4.165, 5.042
2025 MT_{24}	$8.894^{+0.006}_{-0.006}$	6.673
2025 MU_{24}	$2.216^{+0.227}_{-0.100}$	
2025 MU_{59}	$8.189^{+0.008}_{-0.008}$	4.093
2025 MU_{8}	$0.823^{+0.000}_{-0.000}$	0.838
2025 MU_{9}	$3.492^{+3.834}_{-0.000}$	
2025 MV_{31}	$5.801^{+0.016}_{-0.019}$	5.168, 5.177, 5.190, 5.832, 6.497
2025 MV_{38}	$6.006^{+0.021}_{-0.017}$	4.797, 5.332, 6.858, 6.879
2025 MV_{4}	$5.266^{+0.010}_{-0.011}$	4.742, 5.917, 5.925, 7.900
2025 MV_{46}	$3.405^{+0.568}_{-0.231}$	
2025 MW_{70}	$3.885^{+0.010}_{-0.024}$	3.336, 3.591, 4.205, 4.633, 4.643
2025 MX_{34}	$4.677^{+18.676}_{-1.327}$	
2025 MX_{44}	$1.151^{+0.001}_{-0.001}$	1.098
2025 MX_{50}	$1.940^{+0.003}_{-0.003}$	3.882
2025 MX_{63}	$8.287^{+1.752}_{-3.275}$	
2025 MX_{69}	$7.662^{+0.040}_{-0.000}$	5.769, 7.603, 9.109
2025 MY_{23}	$3.058^{+0.209}_{-0.184}$	

Appendix C
Discussion of Rubin's Three Ultrafast Rotators

The determination of ultrafast rotation periods for three of the objects in the RFL dataset warranted further validation to establish confidence in our results. We ran a number of tests to look at the data for these three objects in multiple ways to see whether the very short rotation periods persisted.

First, the reduced $\chi^2 = \sum p_i (O_i - C_i)^2 / N_{\rm obs}$ is expected to be close to 1 for a good model fit and correctly estimated observational uncertainty. A significant shift of χ^2 from 1 indicates either that the fit is bad or that the observational uncertainties are over- or underestimated. The χ^2 values for the full dataset for MK41, MN45, and MJ71 from our high-order Fourier analysis are 1.088, 1.179, and 1.025, respectively (with σ values of 0.049, 0.055, and 0.146 computed from Equation (3)). This is another strong indication for us that the computed periods are correct. The uncertainty ranges of our determined periods are estimated to be 1.1×10^{-4} minutes, 2.7×10^{-5} minutes, and 4.9×10^{-3} minutes, respectively, for MK41, MN45, and MJ71. The Fourier analysis also shows that for MK41 third-order Fourier series are preferred to second-order ones (p-value = 98.2% by F-test), indicating good data quality. And the first-order Fourier series fit gives an erroneous period of 6.516 minutes with a σ value of 0.079.

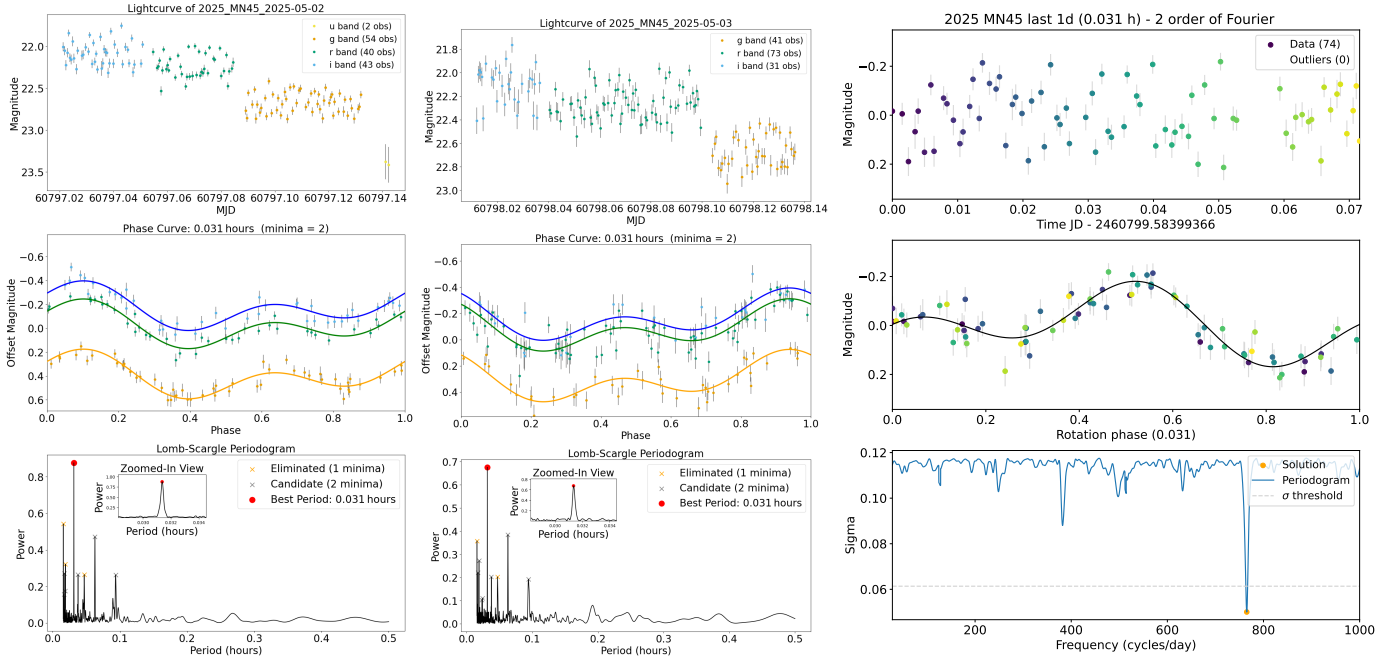

(a) (b) (c)

Figure 33. Lightcurve modeling for 2025 MN_{45} for the nights of (a) May 2, (b) May 3, and (c) May 4 (last 1 day) for each band individually from our LSM (panels (a) and (b)) and high-order Fourier (panel (c)) analyses. The three top, middle, and bottom subpanels in each panel are the same as those described in Figure 13. The rotation periods determined with the data from each individual night agree with those found using the full dataset for each object.

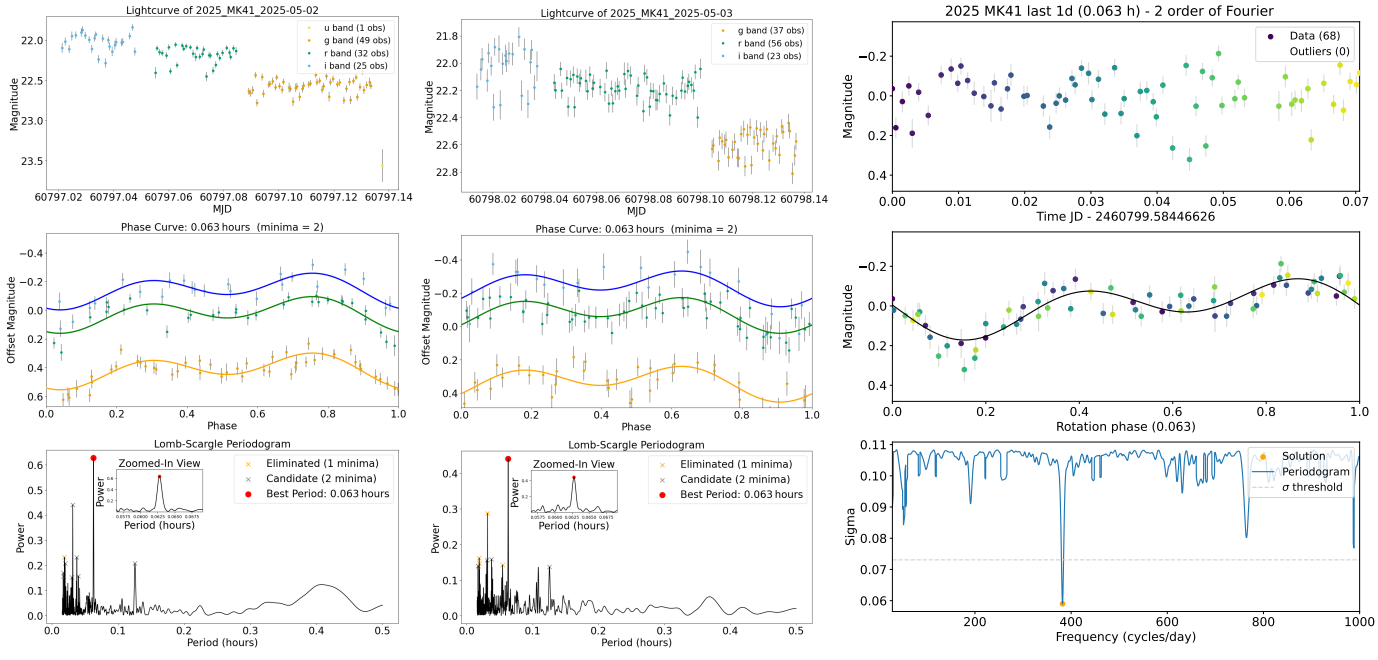

(a) (b) (c)

Figure 34. Similar to Figure 33, but for 2025 MK_{41}.

Second, we split out the observations for the two objects for the nights of 2025 May 2, 3, and 4, when each object has over 70 observations per night. We then ran our lightcurve modeling and rotation period determination using both modeling methods on the three separate nights for each object to see whether we reproduced the same periods on each night as for the full dataset. As evident in Figures 33 and 34, we find a period of 0.031 hr for 2025 MN_{45} and a period of 0.063 hr for 2025 MK_{41}, respectively, on all three individual nights for each object, agreeing with the determined rotation periods using the full observational datasets for both objects. MN45 and MK41 each have >100 observations on each night analyzed and 400–500 observations in total over their 12-day arcs. In contrast, 2025 MJ_{71} has roughly half as many total observations (272) over half the arc lengths (6 days) of MN45 and MK41, with a little more than half as many observations on the individual nights covered in this confidence test. Figure 35 shows that we detect the period of 0.031 hr for May

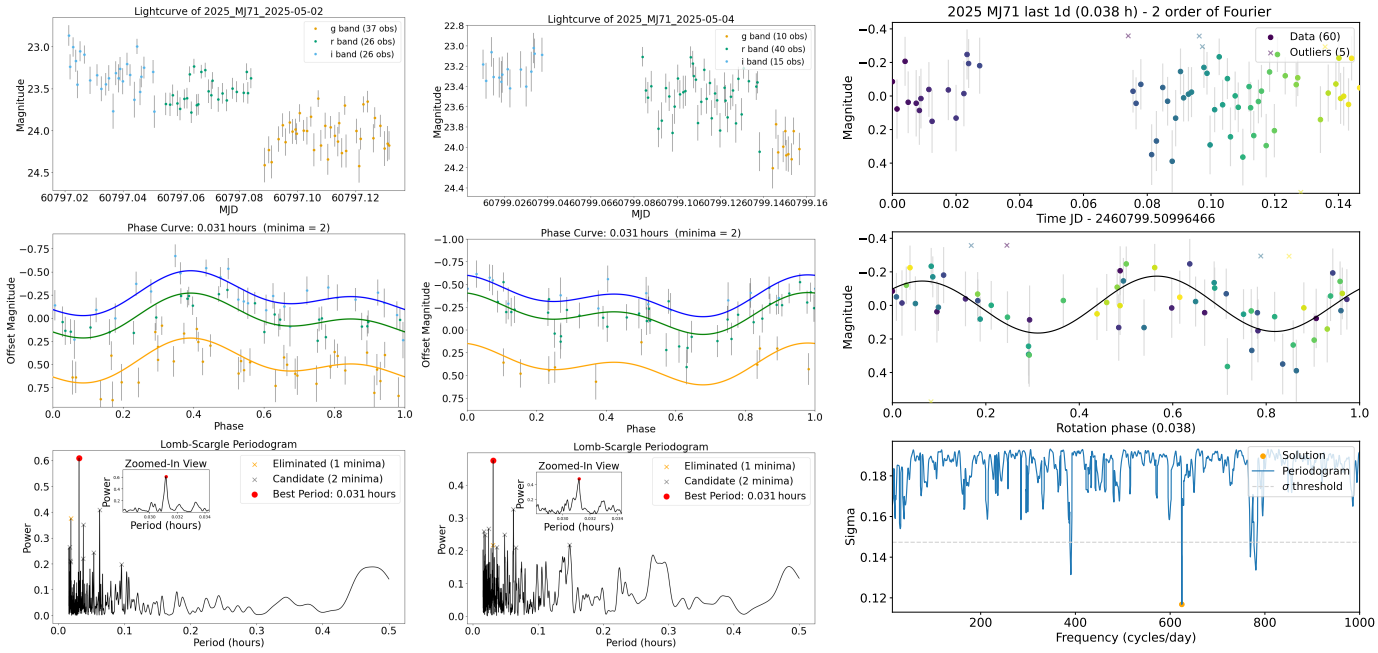

Figure 35. Similar to Figure 33, but for 2025 MJ_{71}. The two methods find slightly different rotation periods for the May 4 data (shown in panels (b) and (c)); this is likely due to the smaller number of observations obtained for MJ71 compared to MN45 (shown in Figure 33) and MK41 (shown in Figure 34). When the full set of observations is used in the fit, the best-fit rotation period for MJ71 is 0.031 hr.

2 and 4 with the LSM method for MJ71. However, the high-order Fourier analysis suggests two possible periods for MJ71 between these two individual nights of data (0.0384 and 0.0312 hr), with 0.0384 hr shown as the best fit for the May 4 data alone. When the full dataset is used in the fit, the best fit is the 0.0312 hr rotational period.

As expected, the uncertainty ranges of the determined periods on each individual night are higher than those using the full observational dataset. The χ^2 values for these smaller data samples are 0.993 and 0.932 for MN45 and MK41, respectively. For MJ71 the χ^2 dropped from 1.025 for the full dataset to 0.553 for the reduced dataset, which is an indicator that the found period for the night of May 4 alone could be spurious. In addition, the values of rms of the observations (computed using Equation (3)) are also slightly different for the individual night observations than for the entire observation set (0.053 for MK41, 0.050 for MN45, and 0.117 for MJ71).

Overall, this test illustrates the difficulty that can arise in reliably fitting lightcurves and rotation periods for objects with $\sim$100 or fewer observations per night; for comparison, we set $>$30 observations in at least two *gri* bands as one of the criteria in our reliability threshold. MN45 and MK41 have dense enough coverage that their rotation periods are consistent between the assessment of each individual night and the full datasets, instilling confidence in the reliability of their determined rotation periods. MJ71 also meets our criteria for reliability but requires the full set of observations to determine a reliable rotation period.

As a third test, we plotted the actual magnitudes (corrected to the median *r*-band magnitude offset) over time and overplotted the best-fit lightcurve model from our LSM method in each band separately for both 2025 May 2 and 3. If the determined rotation period is reliable, the best-fit period in each band on each night should be consistent with small residuals for each band's fit and have a strong peak in the periodogram. We show the results of this test for MN45, MJ71, and MK41 in Figures 36, 37, and 38, respectively. As can be seen in the figures, the rotation periods determined on individual nights across each *gri* band are reproduced for each object in this test.

As a final test of whether these ultrafast rotation periods are an instrumental artifact, we plotted the phased lightcurves for each band separately and added the best-fit model determined for the May 2 data alone. We then used that best-fit period and phase to predict the lightcurve for the May 3 data as a second phased lightcurve following the first night's data. The results of this test are shown in Figure 39. The May 2 data sufficiently predict the lightcurve for the May 3 data for MN45 and MK41. The May 3 data are less well predicted by the May 2 data rotation period and lightcurve for MJ71, likely due to the smaller number of data points; as discussed above, MJ71 requires the full set of observations to determine a reliable rotation period with one of our two methods, which would lead us to expect that this type of prediction may be more difficult than for the other two objects. Nevertheless, the results of this test for the three objects combined are sufficiently convincing that the determined ultrafast rotation periods are thus not likely to be due to an instrumental artifact.

In addition, we wanted to ensure that these very fast rotation periods are not a result of an alias caused by an undersampling of the data. From our Fourier analysis we estimate the maximal frequency of rotation that can be obtained from the available data (D. E. Vavilov & B. Carry 2025). L. Eyer & P. Bartholdi (1999) identified the Nyquist-like frequency limit from finding the largest p-value such that each observation time t_i can be written as $t_i = t_0 + n_i p$, where n_i are integers. The Nyquist frequency then is $f_{\rm Ny} = 1/(2p)$. In our study we are more conservative, we are searching for the maximal p so that $(t_j - t_i)/p$ is an integer with 1% accuracy for 98% of $n(n-1)/$

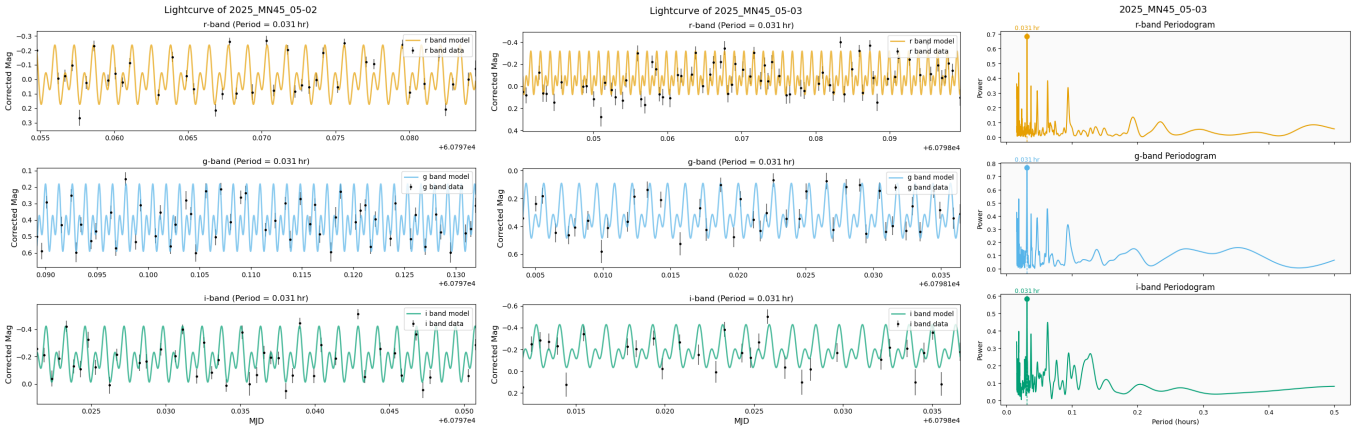

Figure 36. Magnitudes corrected to the median r-band magnitude offset vs. time for 2025 MN_{45} and overplotted with the best-fit lightcurve model in each band separately for both 2025 May 2 (left) and 2025 May 3 (middle). The best-fit period in each band on each night is consistent with small residuals and strong peaks in the periodograms (right) across bands and nights, indicating that the determined rotation period is reliable.

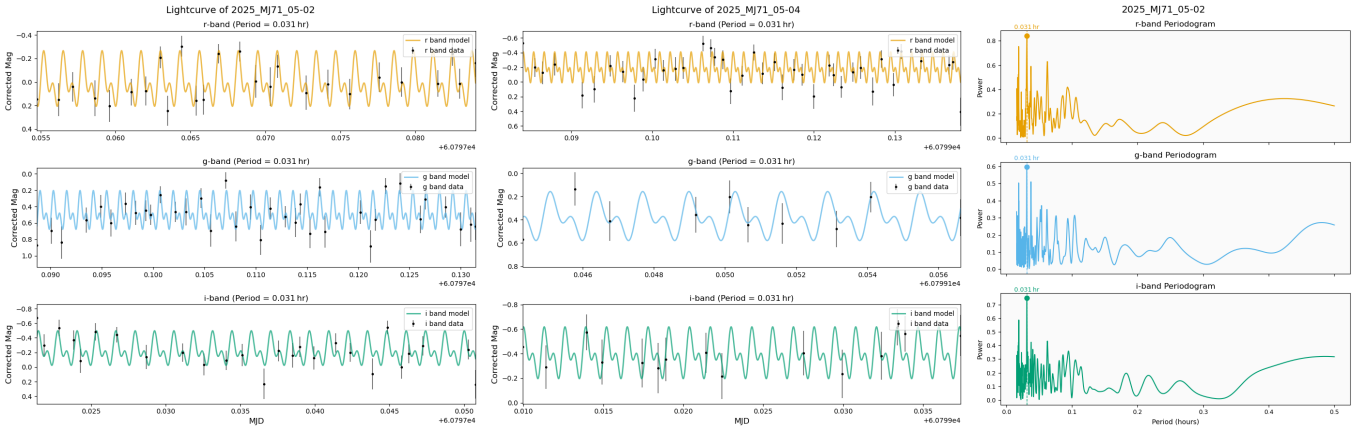

Figure 37. Similar to Figure 36, but for 2025 MJ_{71}.

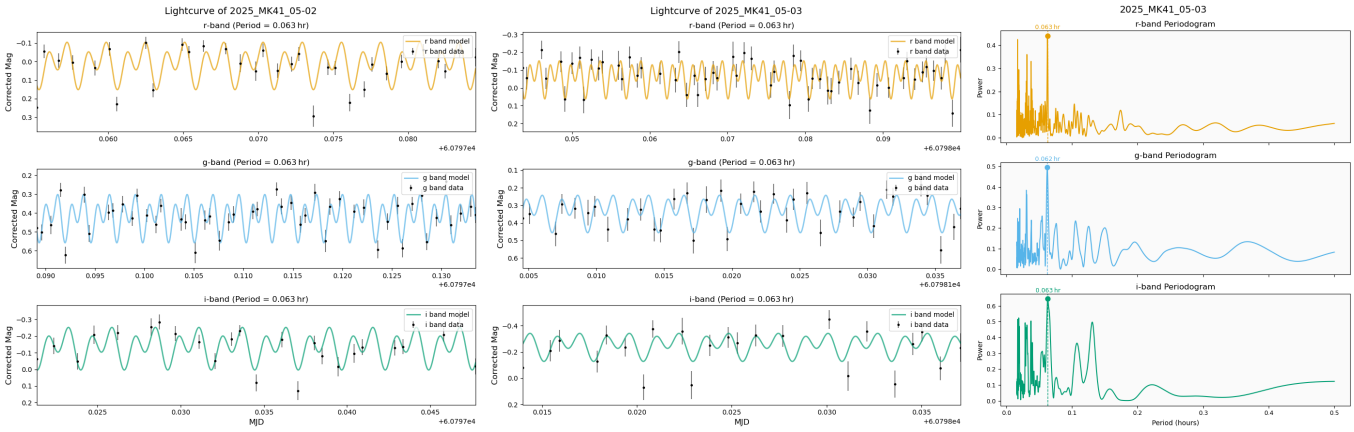

Figure 38. Similar to Figure 36, but for 2025 MK_{41}.

2 pairwise differences. This rule is more strict but gives us more confidence in the results.

It should also be noted that since we require two local maxima in the resulting lightcurve from our analysis, the maximal frequency limit is twice smaller than $f_{\rm Ny}$. For MK41, MN45, and MJ71, the estimated Nyquist frequency limits, $f_{\rm Ny}$, are 2029.63, 2030.42, and 2038.4, respectively. Dividing this by 2 yields a maximal frequency of $>$1000 cycles day^{-1}, which corresponds to 1.44 minutes, smaller than our determined periods (3.78 minutes for MK41, 1.88 minutes for MN45, and 1.92 minutes for MJ71).

To recap, this additional analysis to scrutinize the ultrafast rotation periods determined for MN45, MK41, and MJ71 produces results that agree across different nights and different bands without the need to phase-shift the best-fit models, making the case for this ultrarapid rotation convincing. In

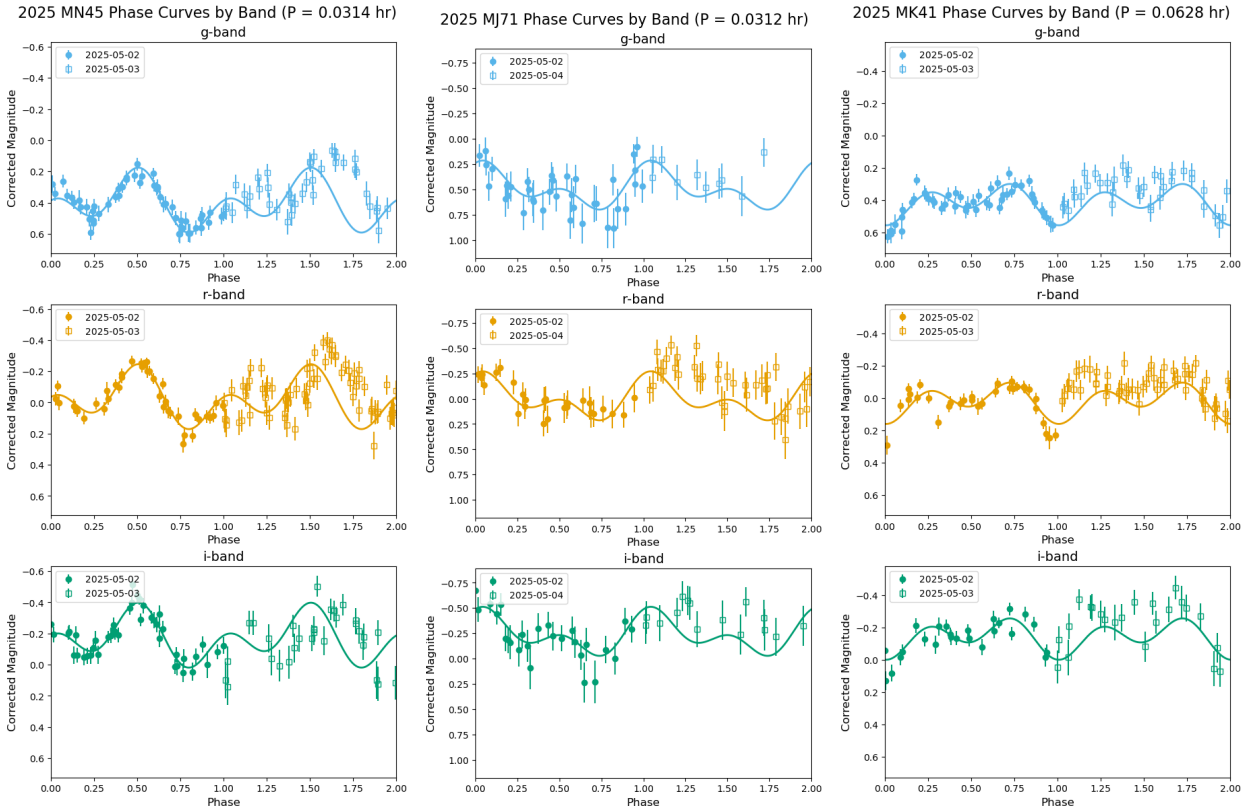

Figure 39. Phase-folded lightcurves for 2025 MN_{45} (left), 2025 MJ_{71} (middle), and 2025 MK_{41} (right) in *g*, *r*, and *i* bands individually. The filled circles show the 2025 May 2 data, and the open squares show the 2025 May 3/4 data. The best-fit rotation period and phase in all panels are computed from the 2025 May 2 data alone and are used to predict the phased lightcurve for the May 3 data as a second phased lightcurve following the first night's data. As is evident, the lightcurves predicted from the May 2 data for the May 3 data and thus the determined rotation periods for all three ultrafast rotators are sufficiently convincing to not likely be due to an instrumental artifact.

addition, we find this rapid rotation for more than one of the objects in the full dataset. The observations span a period of 12 days for MK41 and MN45 and 6 days for MJ71, over which each object changed its on-sky position, resulting in different stars getting used to compute their apparent magnitudes across those nights. Each object also results in a different best-fit rotation period with different features and shapes to their lightcurves. If the ultrarapid magnitude variation was due to an aliasing in the data or an instrumental artifact, we would expect to see the same pattern for all three objects and likely many others. However, out of the full ∼2000-object RFL data release, we only find this rapid rotation for three objects.

As discussed in Section 4.1.1, these are not the only $d > 0.4$ km asteroids to have been found to spin at such rapid rates. Two NEAs and two MBAs, Apollo NEA 2019 MA_2 ($H = 18.91$, $P = 0.044$ hr), MBA (305454) 2008 DP_4 ($H = 16.39$, $P = 0.061$ hr), Amor NEO (285625) 2000 RD_{34} ($H = 17.91$, $P = 0.065$ hr), and MBA (27346) 2000 DN_8 ($H = 15.88$, $P = 0.068$ hr), have also been found to have rotation periods on the order of a few minutes; each of these rotation periods was also determined by independent groups. MN45 is the fastest rotating of these eight objects, all with a relatively small range of periods (0.031–0.068 hr). Together, these objects provide a sufficiently convincing case that objects of this size are capable of spinning at these very high speeds.

Concerning the physical possibility for $d > 0.5$ km asteroids to spin at such rapid rates, as discussed in Section 4.1.1 and shown in Figure 14, MK41, MN45, and MJ71 would require cohesive strengths within the range expected for clay or rocks, but not outside of the realm expected for objects with high strength. As the cohesive strength curves indicate, there are no physical restrictions for subkilometer-sized objects to rotate with periods of <1 hr or faster; it is simply most likely that these objects are rare (B. D. Warner & R. D. Stephens 2020). It is expected that the Rubin Observatory will further probe this subkilometer regime of super- to ultrafast rotators and help us to better understand their numbers among the asteroid population.

ORCID iDs

Sarah Greenstreet https://orcid.org/0000-0002-4439-1539
Zhuofu (Chester) Li https://orcid.org/0000-0003-4285-4453
Dmitrii E. Vavilov https://orcid.org/0009-0007-1972-5975
Devanshi Singh https://orcid.org/0009-0004-0059-3229
Mario Jurić https://orcid.org/0000-0003-1996-9252
Željko Ivezić https://orcid.org/0000-0001-5250-2633
Siegfried Eggl https://orcid.org/0000-0002-1398-6302
Alec Koumjian https://orcid.org/0009-0002-2670-2388
Joachim Moeyens https://orcid.org/0000-0001-5820-3925
Valerio Carruba https://orcid.org/0000-0003-2786-0740
Maria Womack https://orcid.org/0000-0003-4659-8653
Mikael Granvik https://orcid.org/0000-0002-5624-1888
Anastasia Alexov https://orcid.org/0009-0000-7835-3963
Pierre Antilogus https://orcid.org/0000-0002-0389-5706
Brian J. Baumanć https://orcid.org/0000-0001-9438-4516
Eric C. Bellm https://orcid.org/0000-0001-8018-5348

Alexandre Boucaud https://orcid.org/0000-0001-7387-2633
Andrew Bradshaw https://orcid.org/0000-0002-8998-6739
Jeffrey L. Carlin https://orcid.org/0000-0002-3936-9628
Hsin-Fang Chiang https://orcid.org/0000-0002-1181-1621
Felipe Daruich https://orcid.org/0009-0008-2165-0017
Guillaume Daubard https://orcid.org/0009-0004-4351-5968
Erik Dennihy https://orcid.org/0000-0003-2852-268X
Stephanie JH Deppe https://orcid.org/0000-0002-6126-8487
Holger Drass https://orcid.org/0000-0002-7790-9971
Emmanuel Gangler https://orcid.org/0000-0001-6728-1423
Laurent Le Guillou https://orcid.org/0000-0001-7178-8868
Leanne P. Guy https://orcid.org/0000-0003-0800-8755
Patrick Ingraham https://orcid.org/0000-0003-3715-8138
M. James Jee https://orcid.org/0000-0002-5751-3697
Tim Jenness https://orcid.org/0000-0001-5982-167X
Steven M. Kahn https://orcid.org/0000-0003-4833-9137
Arun Kannawadi https://orcid.org/0000-0001-8783-6529
Lee S. Kelvin https://orcid.org/0000-0001-9395-4759
Jacob A. Kurlander https://orcid.org/0009-0005-5452-0671
Nate B. Lust https://orcid.org/0000-0002-4122-9384
Mostafa Lutfi https://orcid.org/0000-0003-2866-3802
Lauren A. MacArthur https://orcid.org/0009-0003-5548-6773
Gabriele Mainetti https://orcid.org/0000-0003-2384-2377
Moniez Marc https://orcid.org/0000-0001-8716-6561
Andrés A. Plazas Malagón https://orcid.org/0000-0002-2598-0514
David Jiménez Mejías https://orcid.org/0000-0002-5859-1136
Řelipe Menanteau https://orcid.org/0000-0002-1372-2534
David J. Mills https://orcid.org/0009-0007-2829-5938
William O'Mullane https://orcid.org/0000-0003-4141-6195
Angelo Fausti Neto https://orcid.org/0000-0002-8095-305X
Jeremy Neveu https://orcid.org/0000-0002-6966-5946
Erfan Nourbakhsh https://orcid.org/0000-0003-3827-4691
HyeYun Park https://orcid.org/0000-0002-7295-2743
Maria T Patterson https://orcid.org/0000-0002-4753-3387
John R. Peterson https://orcid.org/0000-0001-5471-9609
Bruno C. Quint https://orcid.org/0000-0002-1557-3560
Tiago Ribeiro https://orcid.org/0000-0002-0138-1365
Stephen T. Ridgway https://orcid.org/0000-0003-2557-7132
Wouter van Reeven https://orcid.org/0000-0002-1431-9245
Jacques Sebag https://orcid.org/0000-0001-9348-0290
Nima Sedaghat https://orcid.org/0000-0003-4734-2019
Richard A. Shaw https://orcid.org/0000-0003-4058-5202
Alan L. Strauss https://orcid.org/0000-0002-4221-0925
Krzysztof Suberlak https://orcid.org/0000-0002-9589-1306
Ian S. Sullivan https://orcid.org/0000-0001-8708-251X
John D. Swinbank https://orcid.org/0000-0001-9445-1846
Sandrine Thomas https://orcid.org/0000-0002-9121-3436
Adam Thornton https://orcid.org/0000-0001-9342-6032
W. M. Wood-Vasey https://orcid.org/0000-0001-7113-1233
Christopher W. Walter https://orcid.org/0000-0003-2035-2380
Charlotte Ward https://orcid.org/0000-0002-4557-6682
Beth Willman https://orcid.org/0000-0003-2892-9906

References

Aihara, H., Armstrong, R., Bickerton, S., et al. 2018, PASJ, 70, S8
Bianco, F. B., Jones, L., Ivezić, V., Ritz, S. & Rubin Project Science Team 2022, Updated estimates of the Rubin system throughput and expected LSST image depth, Rubin Observatory Project Document PSTN-054, https://pstn-054.lsst.io
Binzel, R. P., Rivkin, A. S., Stuart, J. S., et al. 2004, Icar, 170, 259
Bosch, J., Armstrong, R., Bickerton, S., et al. 2018, PASJ, 70, S5
Bowell, E., Hapke, B., Domingue, D., et al. 1989, in Asteroids II, ed. R. P. Binzel, T. Gehrels, & M. S. Matthews, 524
Carbognani, A. 2017, P&SS, 147, 1
Carruba, V., Camargo, J. I. B., Aljbaae, S., et al. 2024, MNRAS, 527, 6495
Carruba, V., Nesvorný, D., Aljbaae, S., & Huaman, M. E. 2015, MNRAS, 451, 244
Cellino, A., Tanga, P., Muinonen, K., & Mignard, F. 2024, A&A, 687, 277
Chandler, C. O., Bernardinelli, P. H., Jurić, M., et al. 2025, arXiv:2507.13409
Colazo, M., Alvarez-Candal, A., & Duffard, R. 2022, A&A, 666, 77
DeMeo, F. E., & Binzel, R. P. 2011, SMASS-Next: A Next Generation Asteroid Spectroscopic Survey,
Denneau, L., Tonry, J., Heinze, A., et al. 2023, MPEC, 2023-O26, 2023
Eyer, L., & Bartholdi, P. 1999, A&AS, 135, 1
Greenstreet, S., Lu, E., Juric, M., & Moeyens, J. 2021, Bulletin of the AAS, 53, 306.23
Heinze, A., Eggl, S., & Juric, M. 2023, AAS/DPS Meeting, 55, 405.03
Holman, M. J., Payne, M. J., Blankley, P., Janssen, R., & Kuindersma, S. 2018, AJ, 156, 135
Hu, S., Richardson, D. C., Zhang, Y., & Ji, J. 2021, MNRAS, 502, 5277
Ivezić, V., & Ivezić, Ž. 2021, Icar, 357, 114262
Ivezić, Ž., Jurić, M., Lupton, R. H., Tabachnik, S., & Quinn, T. 2002a, SPIE, 4836, 98
Ivezić, Ž., Kahn, S. M., Tyson, J. A., et al. 2019, ApJ, 873, 111
Ivezić, Ž., Lupton, R. H., Jurić, M., et al. 2002b, AJ, 124, 2943
Ivezić, Ž., Tabachnik, S., Rafikov, R., et al. 2001, AJ, 122, 2749
Jurić, M., Axelrod, T., Becker, A. C., et al. 2023, Data Products Definition Document (LSE-163),, LSST Project Document LSE-163, v3.9https://ls.st/LSE-163
Jurić, M., Kantor, J., Lim, K. T., et al. 2017, ASPC, 512, 279
Kaasalainen, M., & Torppa, J. 2001, Icar, 153, 24
Kiss, C., Takács, N., Kalup, C. E., et al. 2025, A&A, 694, 17
Knežević, Z., & Milani, A. 2003, A&A, 403, 1165
Kurlander, J. A., Bernardinelli, P. H., Schwamb, M. E., et al. 2025, The Astronomical Journal, 170, 99
Lang, D., Hogg, D. W., Mierle, K., Blanton, M., & Roweis, S. 2010, AJ, 139, 1782
Li, Z., Chowdhury, Y. A., Ivezić, Ž., et al. 2025, Icar, 438, 116609
Lu, X.-P., & Jewitt, D. 2019, AJ, 158, 220
Margot, J. L., Nolan, M. C., Benner, L. A. M., et al. 2002, Sci, 296, 144
Merritt, S. R., Fedorets, G., Schwamb, M. E., et al. 2025, arXiv:2506.02804
Michel, P., DeMeo, F. E., & Bottke, W. F. 2015, Asteroids IV (University of Arizona Press)
Monteiro, F., Silva, J. S., Tamayo, F., Rodrigues, T., & Lazzaro, D. 2020, MNRAS, 495, 3990
Mottola, S., Britt, D. T., Brown, M. E., et al. 2024, SSRv, 220, 17
Muinonen, K., & Lumme, K. 2015, A&A, 584, A23
Muinonen, K., Uvarova, E., Martikainen, J., et al. 2022, FrASS, 9, 1125
NASA JPL, 2025 Small-Body Database Query, https://ssd.jpl.nasa.gov/tools/sbdb_query.html
Nesvorný, D., Roig, F., Vokrouhlický, D., & Broš, M. 2024, ApJS, 274, 25
O'Mullane, W., Economou, F., Lim, K.-T., et al. 2022, arXiv:2211.13611
Paddack, S. J. 1969, JGR, 74, 4379
Parker, A., Ivezić, Ž., Jurić, M., et al. 2008, Icar, 198, 138
Penttilä, A., Shevchenko, V. G., Wilkman, O., & Muinonen, K. 2016, P&SS, 123, 117
Pravec, P., & Harris, A. W. 2007, Icar, 190, 250
Pravec, P., Scheirich, P., Kušniraák, P., et al. 2016, Icar, 267, 267
Roodman, A., Rasmussen, A., Bradshaw, A., et al. 2024, SPIE, 13096, 130961S
Rubin Observatory Science Pipelines Developers 2025, The LSST Science Pipelines Software: Optical Survey Pipeline Reduction and Analysis Environment, Project Science Technical Note PSTN-019, NSF-DOE,
Sánchez, P., & Scheeres, D. J. 2014, M&PS, 49, 788
SLAC National Accelerator Laboratory & NSF-DOEVera C. Rubin Observatory 2024, The LSST Commissioning Camera (LSSTComCam), SLAC National Accelerator Laboratory (SLAC)

SLAC National Accelerator Laboratory & NSF-DOEVera C. Rubin Observatory 2025, The LSST Camera (LSSTCam) (SLAC)
Spratt, C. E. 1990, JRASC, 84, 123
Stalder, B., Munoz, F., Aguilar, C., et al. 2024, SPIE, 13094, 1309409
Strauss, R., McNeill, A., Trilling, D. E., et al. 2024, AJ, 168, 184
Szabó, G. M., & Kiss, L. L. 2008, Icar, 196, 135
Szabó, G. M., Pál, A., Szigeti, L., et al. 2022, A&A, 661, 48
Takács, N., Kiss, C., Szakáts, R., et al. 2025, ApJ, 986, 33
Tanga, P., Pauwels, T., Mignard, F., et al. 2023, A&A, 674, A12
VanderPlas, J. T., & Ivezić, Ž. 2015, ApJ, 812, 18
Vavilov, D. E., & Carry, B. 2025, A&A, 693, A66
Vera C. Rubin Observatory 2025, The Vera C. Rubin Observatory Data Preview, 1
Warner, B. D., Harris, A. W., & Pravec, P. 2009, Icar, 202, 134
Warner, B. D., & Stephens, R. D. 2020, MPBu, 47, 23
York, D. G., Adelman, J., Anderson, J. E., Jr., et al. 2000, AJ, 120, 1579
Zappala, V., Cellino, A., Barucci, A. M., Fulchignoni, M., & Lupishko, D. F. 1990, A&A, 231, 548